Biomaterials 225 (2019) 119493

Contents lists available at ScienceDirect

Biomaterials

journal homepage: www.elsevier.com/locate/biomaterials

Review

Mechanical considerations for polymeric heart valve development: Biomechanics, materials, design and manufacturing

Richard L. Li[a,e], Jonathan Russ[b], Costas Paschalides[a], Giovanni Ferrari[c], Haim Waisman[b], Jeffrey W. Kysar[a,d,**,1], Kalfa David[e,1,*]

[a] Department of Mechanical Engineering, Fu Foundation School of Engineering and Applied Science, Columbia University, New York, NY, USA
[b] Department of Civil Engineering and Engineering Mechanics, Fu Foundation School of Engineering and Applied Science, Columbia University, New York, NY, USA
[c] Department of Surgery and Biomedical Engineering, Columbia University Medical Center, New York, NY, USA
[d] Department of Otolaryngology – Head and Neck Surgery, Columbia University Medical Center, New York, NY, USA
[e] Division of Cardiac, Thoracic and Vascular Surgery, Section of Pediatric and Congenital Cardiac Surgery, New-York Presbyterian - Morgan Stanley Children's Hospital, Columbia University Medical Center, New York, NY, USA

ARTICLE INFO

Keywords:
Native heart valves
Polymeric heart valves
Soft tissue mechanics
Mechanobiology
Mechanical testing

ABSTRACT

The native human heart valve leaflet contains a layered microstructure comprising a hierarchical arrangement of collagen, elastin, proteoglycans and various cell types. Here, we review the various experimental methods that have been employed to probe this intricate microstructure and which attempt to elucidate the mechanisms that govern the leaflet's mechanical properties. These methods include uniaxial, biaxial, and flexural tests, coupled with microstructural characterization techniques such as small angle X-ray scattering (SAXS), small angle light scattering (SALS), and polarized light microscopy. These experiments have revealed complex elastic and viscoelastic mechanisms that are highly directional and dependent upon loading conditions and biochemistry. Of all engineering materials, polymers and polymer-based composites are best able to mimic the tissue-level mechanical behavior of the native leaflet. This similarity to native tissue permits the fabrication of polymeric valves with physiological flow patterns, reducing the risk of thrombosis compared to mechanical valves and in some cases surpassing the *in vivo* durability of bioprosthetic valves. Earlier work on polymeric valves simply assumed the mechanical properties of the polymer material to be linear elastic, while more recent studies have considered the full hyperelastic stress-strain response. These material models have been incorporated into computational models for the optimization of valve geometry, with the goal of minimizing internal stresses and improving durability. The latter portion of this review recounts these developments in polymeric heart valves, with a focus on mechanical testing of polymers, valve geometry, and manufacturing methods.

1. Introduction

There have been many attempts to design and manufacture prosthetic heart valves that can function as effectively and reliably as native valves. Decades of research and development have shown that this is an extremely challenging task [1]. Heart valves operate in a demanding environment, and in response, nature has evolved a complex hierarchical architecture specially suited to maintain valve function for many decades. Additionally, recent studies of valvular cells have shown that heart valves are not purely passive devices and that valve homeostasis and remodeling is a complex and active mechanical and biological phenomenon [2]. Thus, the mechanical characteristics of native valves are extremely difficult to replicate, and current state-of-the-art mechanical and bioprosthetic valves continue to be plagued by the same types of complications (thrombosis, calcification, structural valve degeneration, pannus, material failure) that beset the first human-implanted caged-ball valves over 60 years ago [3]. As of 2015, there were an estimated 75,000 prosthetic valves implanted in the U.S. each year, and 170,000–250,000 worldwide [4]. The current standard of care offers patients a choice between mechanical and bioprosthetic

* Corresponding author. Pediatric Cardiac Surgery, New York-Presbyterian Morgan Stanley Children's Hospital, Columbia University Medical Center, 3959 Broadway, CHN-274, New York, NY, 10032, USA.
** Corresponding author. Department of Mechanical Engineering, Columbia University, 248 Mudd Building, Mail Code 4703, 500 W. 120th Street, New York, NY, 10027, USA.
E-mail addresses: jk2079@columbia.edu (J.W. Kysar), dk2757@cumc.columbia.edu (D. Kalfa).
[1] co-senior authors.

https://doi.org/10.1016/j.biomaterials.2019.119493
Received 23 April 2019; Received in revised form 21 August 2019; Accepted 11 September 2019
Available online 17 September 2019
0142-9612/

valves. In 2006, ~78% of aortic valve replacements were bioprosthetic and ~21% were mechanical [5]. More recently, there has been a trend towards increasing use of bioprosthetics, which has been accelerated by the success of transcatheter aortic valve replacements (TAVR) [5,6].

Mechanical valves are generally made in a tilting-disk configuration, with one or two rigid leaflets that rotate on hinges. The leaflets, also known as occluders, are constructed either entirely from pyrolytic carbon or from graphite coated with pyrolytic carbon. These types of valves are generally very durable, as pyrolytic carbon is strong and quite resistant to abrasion and fatigue [7–10]. Wear testing of St. Jude Medical mechanical valves has predicted that the pyrolytic carbon coating on the valves could last well over 200 years [11]. Clinically, bileaflet mechanical valves have demonstrated durability beyond 30 years, with low rates of valve-related mortality [12]. However, due to the brittle nature of the material, fracturing of the leaflets, struts, or housings of implanted mechanical valves has occurred on rare occasions [4]. A significant disadvantage of mechanical valves is the non-physiological hemodynamics created by the geometry of the valves coupled with the rigidity of the synthetic materials. Since blood flow must separate as it passes by the leaflets, this results in areas of stasis distal to the orifice and the leaflets [13] as well as regions of high shear stress [14], creating conditions that precipitate thrombosis and require the patient to undergo lifelong anticoagulation therapy [15]. Additionally, increased forces on the aortic wall due to abnormal flow patterns can induce the altered expression of extracellular matrix proteins, resulting in vascular remodeling, aortic dilatation, and possible aneurysm development [16,17].

Bioprosthetic valves (BHVs) are constructed from porcine valve or bovine pericardial tissue [4]. The geometry and mechanical properties of animal valves are similar to those of humans (Table 3). Consequently, they provide the advantages of physiological flow patterns and low thrombogenicity compared to mechanical valves. Durability in adults has reached up to ~20 years, but is largely limited by the onset of structural valve degeneration (SVD), which is characterized by thickening, calcification, tearing, or other disruptions to the leaflet tissue leading to stenosis or regurgitation [18–20]. Likely mechanisms for SVD include tissue processing conditions and imperfections in valve design, which cause collagen fiber disruption and create regions of high mechanical stress [4,18,21,22]. For example, the use of sutures to affix pericardial bioprostheses to stents has been shown to result in tearing of the leaflets at the free edge near the stent posts [23]. Also, the most common preservative for bioprosthetic tissues is glutaraldehyde, which has been shown to adversely affect the shear and flexural properties of the tissue [24–28]. This leads to increased internal stresses, which have been correlated with increased calcification and reduced fatigue life [29–31]. Moreover, glutaraldehyde fixation and storage lead to the formation of free aldehydes in the tissue that bind to calcium *in vivo* [32].

Thus, despite being considered the “gold standard” in heart valve replacements, neither mechanical nor bioprosthetic valves are ideal solutions.

The concept of tissue engineered heart valves (TEHV) offers the greatest potential for developing a durable valve replacement, since the theoretical result of the tissue engineering process is a completely biological valve, grown with the patient's own cells. In the initial paradigm of tissue engineering, a biodegradable valve-shaped scaffold is seeded with cells, matured *in vitro* in a bioreactor and then implanted in the patient so that leaflet tissue can grow naturally. Nevertheless, tissue-engineered valves still have major shortcomings, including insufficient structural stability of the leaflets and an uncontrolled balance between polymer biodegradation and extracellular matrix formation, which ultimately leads to failure of these constructs [33].

Flexible leaflet polymeric prosthetic heart valves are a promising and more affordable alternative to TEHV and bioprosthetic valves [1]. Raw polymer materials can be designed to more closely match the material properties of native tissue, and polymer films can easily be formed into geometries permitting physiological flow. Thus, polymeric valves have the potential to be more durable than bioprosthetic valves while avoiding the long-term anticoagulation treatment that is required for mechanical valves. Additionally, typical polymer valve fabrication techniques such as dip molding and compression molding are already well-studied and widely used in the plastics industry. A plethora of biocompatible and biostable polymers have shown promise in polymeric valve applications. These include both polymers that are commercially available, such as Estane® [35–38], Tecothane™ [39], ElastEon™ [36,38], and Gore-Tex® [40,41], and polymers that have been developed at the investigative level, including ADIAMat [42,43], xSIBS [44,45], and POSS-PCU [46,47]. However, challenges with durability remain. There have been few examples of human implantation, and commercial usage of polymeric valves has been limited to ventricular assist devices (VADs). The remaining mismatch with the complex mechanical properties of native valve tissue, in conjunction with imperfect valve geometry and surface morphology, appears to be a major underlying cause of structural degeneration of the polymer material, calcification, thrombosis, and overall limited durability during *in vivo* experiments [35]. The aim of this review is to inform the reader of important mechanical considerations when designing flexible leaflet polymeric devices. These include a comprehensive knowledge of the structure and mechanical properties of native heart valves, techniques for evaluating polymer mechanical properties, valve geometry, and manufacturing methods. We will focus on valves with the trileaflet configuration (aortic and pulmonary), but also discuss data related to the atrioventricular valves (mitral and tricuspid) when it is instructive.

2. Native valve properties

2.1. Structure and composition of semilunar native leaflet tissue

The largely passive nature of a heart valve leaflet belies a complex macro- and microstructure that is critical to maintaining good valve function through the billions of cycles in a person's lifetime. Briefly, pulmonary valve (PV) and aortic valve (AV) leaflets can be described as having four macroscopic regions: the hinge, belly, coapting surface, and the lannula which includes the nodulus of Morgagni (pulmonary valve) or of Arantius (aortic valve) [48]. A cross-section of leaflet tissue reveals three primary layers - the fibrosa, spongiosa, and ventricularis (Fig. 1a and b). The fibrosa functions as the main load bearing layer, and the ventricularis helps to reduce strain when the valve is fully opened. The spongiosa is traditionally thought to serve as a lubricating buffer layer between the fibrosa and ventricularis. The five main building blocks of these layers are collagen, elastin, glycosaminoglycans (GAGs), valvular interstitial cells (VICs), and valvular endothelial cells (VECs).

The fibrosa is located on the arterial side of the leaflet. As the main load bearing layer, it is the thickest of the three layers and extends over the entire leaflet surface [21,48,50]. Aptly named, it consists mainly of a dense network of type I collagen fibers arranged mostly in the circumferential direction, along with some collagen fibers arranged radially [21]. The circumferential collagen bundles transfer most of the load during diastole from the leaflets to the arterial wall, and they are embedded within a characteristic series of macroscopic folds of the fibrosal layer, which appear as corrugations that run parallel to the free edge [31,48]. Doehring et al. showed that collagen bundles within the leaflet comprise only part of a complex collagen mesostructure, which also includes membranes, pinnate fiber structures, and fractal-like branching patterns (Fig. 1c and d) [49]. Elastin in the fibrosa is arranged primarily in the form of tubes that surround the circumferential collagen bundles, along with some loosely arranged radial elastin fibers [51,52].

The ventricularis is located on the ventricle side and consists of collagen and sheets of fine elastin fibers, both aligned mostly in the radial direction with some in the circumferential direction as well

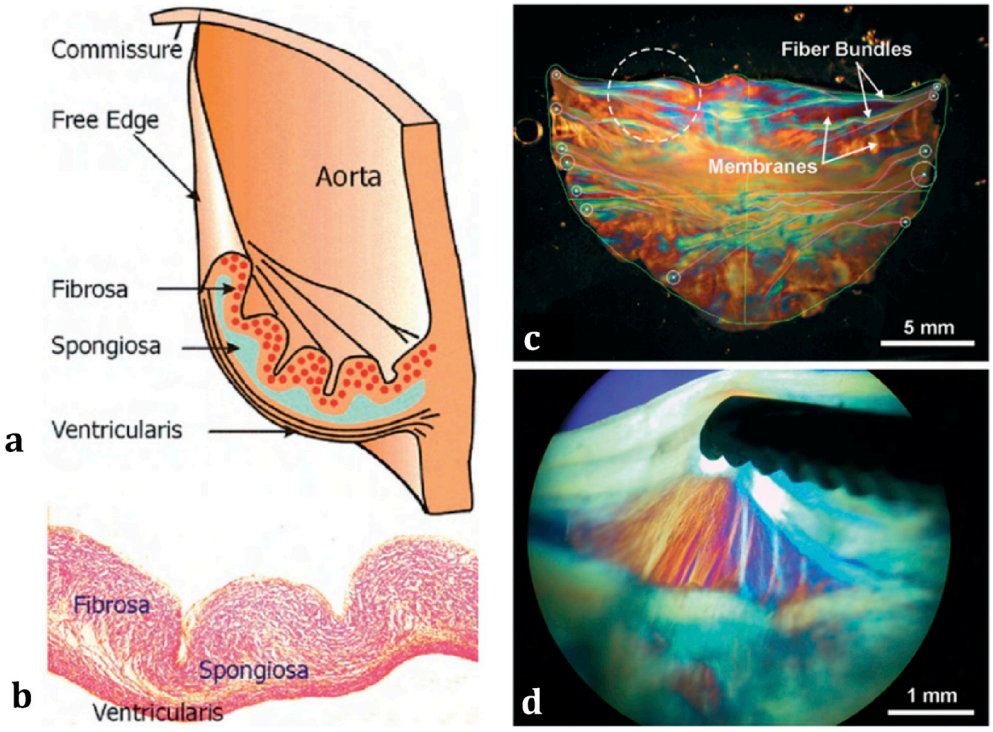

Fig. 1. (a) Cross section through the leaflet and aortic wall showing internal arrangement of fibrosa, spongiosa, and ventricularis. The fibrosa is shown in a folded configuration. It unfolds as the leaflet stretches radially. (b) Corresponding histological section. (c) Polarized light image of right coronary leaflet from the AV showing circumferentially-oriented collagen fiber bundles and interconnecting collagen membranes. (d) Magnified view of circular area in (c) showing alignment of collagen within individual fiber bundles and membranes [49]. Figures reprinted with permission from ICR Publishers.

[52–55]. The radial fiber arrangement in this layer acts to limit radial strains during leaflet opening and helps the leaflet return to the closed position [55]. The ventricularis also thickens near the free edge of the leaflet to form the lannula and noduli [56].

The spongiosa is made primarily of hydrophilic GAGs, which can combine with proteins to form proteoglycans (PGs) [57]. It also contains extensive collagen fiber and elastin interconnections which appear to bind the fibrosa and ventricularis [58,59]. The spongiosa is thought to act as a buffer layer to permit shearing and deformation between the outer layers [24–27,57,60]. GAGs have been shown to have a damping effect, so the spongiosa may also have a role in reducing leaflet flutter during forward flow [61]. However, some flexural testing data has shown a continuous transmural strain distribution from the fibrosa across to the ventricularis, suggesting that the spongiosa is not a separable layer with distinct mechanical properties but rather a transition region which functions only to resist delamination between the two outer layers [50,58].

Two main cell types, endothelial cells (VECs) and interstitial cells (VICs), help to maintain valve function through their chemical and mechanical responses to biomechanical stimuli [2]. VECs are oriented circumferentially over both the arterial and ventricular surfaces of the leaflet [48,62]. Their function is to regulate interactions between blood flow and VICs, including metabolic and inflammatory processes [63]. They have also been shown to have an active role in regulating the mechanical properties of leaflet tissue through interactions with VICs, impacting tissue stiffness by up to 30% [64,65]. Endothelial cells in vascular tissue are typically elongated in the direction of blood flow, but on valve leaflets their circumferential arrangement appears to be more closely related to leaflet stresses and tissue mechanics under diastolic loading, rather than hemodynamic forces [62].

VICs are located throughout the fibrosa, spongiosa and ventricularis. They encompass multiple phenotypes that are regulated through interactions with VECs. These phenotypes include smooth muscle cells, fibroblasts that secrete the collagen, elastin, and GAGs that comprise the valvular extracellular matrix (ECM), and myofibroblasts that exhibit characteristics of both muscle cells and fibroblasts [66–71]. The phenotype of the myofibroblasts is thought to be plastic and reversible, as fibroblasts have been shown to trans-differentiate into myofibroblasts in response to biophysical stimuli [66,67,69,72]. In addition to the synthesis of valvular extracellular matrix (ECM) molecules, VICs facilitate ECM remodeling and repair through the expression of matrix-degrading enzymes and their inhibitors [70,72,73]. VICs demonstrate contractile behavior in response to vasoactive agents with measurable effects on leaflet stiffness [64,70,74]. It has been speculated that VIC contraction may also facilitate cell-to-cell communication and serve a role in maintaining leaflet homeostasis [70,75–77].

Clark and Finke showed that the thickness of the human AV leaflet varies greatly across the surface, from 1760 μm at the noduli to 177 μm in the belly region, where it can be nearly transparent [53,54]. While PV and AV leaflets share the same basic structure, the primary difference is that AV leaflets are significantly thicker [56,78,79]. The intraluminal pressures in the aorta range between 120 mmHg in systole and 80 mmHg in diastole, while the corresponding values for the pulmonary artery are much lower at 25 mmHg and 8 mmHg [80]. Accordingly, Stradins et al. measured total leaflet thickness in human valves to be greater for AV leaflets (605 ± 196 μm) than PV leaflets (397 ± 114 μm) [81]. Joyce et al. showed that in porcine valves, most of this difference in thickness can be attributed to the fibrosa and ventricularis (Table 1). They also measured the decrease in leaflet thickness as transvalvular pressure was increased from 0 to 90 mmHg. The fibrosa and spongiosa contributed the most to the decrease in total thickness, while the decrease in thickness of the ventricularis was proportionally smaller due to its higher elastin content [78].

2.2. Mechanical properties of semilunar native leaflet tissue

2.2.1. Mechanical environment

In terms of mechanical loading, heart valve leaflets are subjected to a cycle of flexure (leaflet opening), shear (flow of blood through the valve), flexure (leaflet closing) and tension (leaflets suppressing backflow of blood). To determine the *in vivo* stresses due to these cycles of loading, Thubrikar et al. recorded the geometrical changes of the leaflet using radiopaque markers placed on the AV leaflets of dogs [82–84]. Among many other measurements, the authors found that the angle of rotation around the base of the leaflet in the radial direction was 75°, measured from mid-diastole to mid-systole. The angle of rotation

Table 1
Change in thickness of leaflets and individual layers with increase in transvalvular pressure [78]. Table reprinted with permission from Elsevier.

Transvalvular pressure	Total thickness (μm)	Fibrosa thickness (μm)	Spongiosa thickness (μm)	Ventricularis thickness (μm)	Fibrosa thickness/ total thickness (%)	Spongiosa thickness/total thickness (%)	Ventricularis thickness/total thickness (%)
Low pressures (PV)	265.7 ± 11.6	115.6 ± 4.7	88.3 ± 4.1	55.8 ± 3.9	43.8 ± 2.3	33.4 ± 2.0	20.7 ± 1.3
High pressures (PV)	188.8 ± 8.5	80.8 ± 5.1	58.7 ± 3.2	49.3 ± 1.9	42.6 ± 2.7	31.0 ± 1.6	26.4 ± 2.1
Low pressures (AV)	388.7 ± 21.7	262.2 ± 18.0	81.6 ± 1.0	89.9 ± 6.9	68.6 ± 10.6	21.8 ± 2.3	23.3 ± 2.6
High pressures (AV)	228.8 ± 9.3	142.7 ± 6.9	35.8 ± 3.7	60.9 ± 6.9	63.1 ± 6.0	15.0 ± 2.5	26.0 ± 4.0

around the commissures in the circumferential direction was 81°, while the circumferential curvature at the leaflet midsection changed from $0.11\,\mathrm{mm}^{-1}$ (diastole) to $-0.10\,\mathrm{mm}^{-1}$ (systole). These values were later corroborated by Sugimoto and Sacks for porcine AVs, with an 80° circumferential angle of rotation and circumferential curvatures of $0.186\,\mathrm{mm}^{-1}$ (diastole) and $-0.142\,\mathrm{mm}^{-1}$ (systole) [85].

From these recorded changes in curvature, Thubrikar et al. first calculated bending stress and then superimposed membrane stress to obtain the total stress. The baseline membrane stress σ_c along the circumferential direction was approximated as the hoop stress in the wall of a cylindrical pressure vessel

$$\sigma_c = \frac{PR}{t}, \tag{1}$$

where P is the transvalvular pressure, R is the radius of curvature of the leaflet, and t is the mean thickness of only the fibrosa, which is the main flexural layer since the ventricularis and spongiosa are assumed not to sustain bending stress. The radial membrane stress σ_r was approximated as the longitudinal stress in the wall of a cylindrical pressure vessel

$$\sigma_r = \frac{PR}{2t}. \tag{2}$$

Using $P = 80\,\mathrm{mmHg}$, $R = 9\,\mathrm{mm}$, $t = 0.11\,\mathrm{mm}$ circumferentially, and $t = 0.12\,\mathrm{mm}$ radially, the resulting values for membrane stress in diastole were 854 kPa circumferentially and 406 kPa radially. Then, superimposing bending stresses due to changes in leaflet curvature, it was shown that the total stress in diastole ranged from 760–950 kPa circumferentially and 370–440 kPa radially across the thickness of the fibrosa. The stresses in systole were assumed to be negligible due to the small pressure gradient and small radius of curvature of the leaflet.

Christie estimated the radial stress near the center of the AV leaflet in diastole using Eq. (2), with $P = 80\,\mathrm{mmHg}$, $R = 10\,\mathrm{mm}$, and $t = 0.5\,\mathrm{mm}$, yielding a stress of 106 kPa. However, it was assumed that only half of the leaflet thickness was load-bearing, so the final stress estimate was 200 kPa [86]. Parfeev et al. followed the same formula, but used pressures of 120 mmHg for the AV and 30 mmHg for the PV, a leaflet thickness of 0.25 mm, and radii of curvature of 10–20 mm, resulting in physiological radial stress estimates of 320–640 kPa for the AV and 80–160 kPa for the PV [87].

Cataloglu et al. used stereophotogrammetry to obtain a three-dimensional description of a human AV in the closed position, then performed finite element analysis using thin shell elements. The maximum principal stresses in diastole were found to be in the circumferential direction in the non-coronary leaflet and ranged between ~460 and ~550 kPa. Maximum principal stresses in the coronary leaflets ranged between ~320 and ~420 kPa [88,89]. It is important to note that these models assumed material homogeneity and isotropy, while the native leaflet is a complex structure and cannot truly be modeled with a single homogeneous material. However, these values are useful as estimates to inform the design of prostheses. To capture some of the heterogeneity of the AV leaflet, Rego and Sacks developed a functionally graded model (FGM), where the properties of the leaflet vary along the transmural direction z but are homogeneous at any z location. At end-diastole, the FGM predicted leaflet stresses to peak at ~200 kPa in the fibrosa in both the radial and circumferential directions and again at ~200 kPa in the ventricularis in the radial direction. Near the center of the thickness of the spongiosa, the stress in both directions dropped to a minimum of less than 50 kPa [90].

In addition to these internal stresses, hemodynamic forces also impose surface stresses on valvular leaflets. Weston et al. used laser Doppler velocimetry to calculate the maximum shear stress on the ventricular surface of a polyurethane valve leaflet to be $79\,\mathrm{dyne/cm}^2$ [91]. Yap et al. used a similar technique on a glutaraldehyde-fixed porcine valve, finding maximum shear stresses of $70\,\mathrm{dyne/cm}^2$ on the ventricular surface during systole and $23\,\mathrm{dyne/cm}^2$ on the fibrosal surface during diastole [92,93].

There is significant regional variation and directional dependency in strain across the leaflet [94–96]. Lo and Vesely subjected porcine AVs to a series of static pressure loadings, ranging from 0 to 130 mmHg [94]. At 80 mmHg, they found maximum radial strains of ~33% at the center of the leaflet nearer the noduli and maximum circumferential strains of ~15% near the commissures. Minimum radial strains of ~13% occurred near the commissures and minimum circumferential strains of ~6% occurred at the center of the leaflet nearer the base. Beyond 80 mmHg, the leaflet tissue appeared to lock up and did not stretch significantly further. Aggarwal et al. calculated the *in vivo* surface strains of human AV leaflets using 3D transesophageal echocardiography [95]. From the open to the closed configuration, a maximum radial strain of ~50% occurred at the leaflet base nearer the ventricle, and a maximum circumferential strain of ~50% occurred near the commissures. Minimum radial and circumferential strains of ~20% and ~10%, respectively, occurred along the middle of the free edge, away from the commissures. Across the whole leaflet, the strain in the radial direction was generally larger than in the circumferential direction, except at the commissures. These results are qualitatively consistent with porcine AV data obtained *in vitro* via stereophotogrammetry and under pulsatile flow by Weiler et al. [96]. The maximum radial strains were ~30% at the coaptation area and at the leaflet base nearer the ventricle, and the maximum circumferential strains were ~20% near the commissures, with all maximum strains occurring at peak diastole. It is unlikely that the differences in strain values between the studies are due to loading conditions (i.e. static pressure loading vs. pulsatile flow) since leaflet tissue is known to have little strain-rate dependency when loaded biaxially, as we will discuss later. Instead, these variations might be attributed to other experimental conditions such as species of sample (e.g. human in Aggarwal et al. vs. porcine in Weiler et al.) and imaging technique and analysis.

Due to the dynamic leaflet movements and high rates of deformation during normal valve function, accurate estimates of strain rates are integral to an understanding of leaflet tissue mechanics. Since local strains vary widely across the leaflet, local strain rates will necessarily vary as well. Missirlis estimated the maximum radial strain rate in the leaflets to be $2.5\,\mathrm{s}^{-1}$, based on a valve closure time of 0.04 s and a maximum radial strain during closure of 10%, as measured during static pressure loading on human AVs *in vitro* [97]. However, this radial strain measurement was based on a planar projection of the leaflets and does not agree with the maximum strain measurements discussed previously [94–96], which were based on three-dimensional data and likely to be more accurate. Additionally, a later study by Missirlis and Chong, using similar static pressure loading conditions but with

imaging by stereophotogrammetry, found radial strains to be much higher than 10% in many areas of the porcine AV non-coronary leaflet [98]. In contrast to the initial study by Missirlis, high-speed *in vivo* imaging of canine leaflets by Thubrikar et al. showed circumferential strains of 10.1% and radial strains of 30.8% during a valve closure time of 20–25 ms. This corresponds to circumferential and radial strain rates of $4.4 \pm 0.8\ s^{-1}$ and $12.4 \pm 1.6\ s^{-1}$, respectively [99,100]. Since the measurements of Thubrikar et al. were based on three-dimensional geometric analysis of video taken from four different angles, their estimates of physiological strain rates are likely to be more reliable than that of Missirlis.

2.2.2. Micromechanics

As previously mentioned, the primary building blocks of leaflet tissue include collagen, elastin, and GAGs. Collagen fibers have a hierarchical structure, with collagen fibrils bound together by proteoglycans to form fibers [101]. Circumferential bundles of collagen fibers in the fibrosa transfer the bulk of the load during diastole from the leaflets to the arterial wall [48]. Load on the leaflets is initially carried by the elastin while the continued stretching of the leaflet tissue causes the collagen fibers, which are initially crimped in a wavy configuration, to uncrimp. Once uncrimped, the load transfers to these much stiffer and less extensible collagen fibers, which resist further deformation. Upon unloading, the elastin tubes and fibers have the role of returning the collagen fibers to their crimped configuration [51,55,102,103]. The collagen and elastin in the ventricularis act together in a similar manner, although the primary fiber orientation is radial, rather than circumferential. As the ventricularis is stretched radially during systole, the crimped collagen fibers become fully extended, limiting the leaflet radial strains, while the elastin helps the leaflet contract back from the stretched position [55]. A schematic stress-strain curve describing this loading behavior (Fig. 2a) shows four main regions: (a) a low stress-low strain linear elastic regime where the load is carried by compliant elastin fibers while the collagen fibers are uncrimping, (b) a highly non-linear transition regime likely representing the transfer of load from elastin to collagen, (c) a more linear elastic regime of increased stiffness dominated by the relatively inextensible collagen fibers, and (d) yielding and failure of the elastin and collagen fibers [21,104,105].

Joyce et al. documented the changes in collagen fiber crimp, as well as fiber alignment, in porcine AV and PV leaflets as transvalvular pressure was increased from 0 to 90 mmHg [78]. Crimp was quantified using polarized light microscopy, which produced periodic light-distinguishing bands that correspond to the crimp period, defined as the distance between two adjacent crimp peaks. In the unloaded state (0 mmHg), both the AV and PV showed collagen crimp periods of ~12 μm. As pressure was increased from 0 mmHg, the AV showed a large increase in crimp period up to 4 mmHg, which is just enough pressure to induce coaptation for both types of valves, while the PV showed a large increase up to 20 mmHg. Beyond these pressures, there were minimal additional increases in crimp period for both the AV and PV. Additionally, at 0 mmHg, ~60% and ~40% of the areas of the belly regions of the AV and PV, respectively, contained visibly crimped structures. At 90 mmHg, this value had reduced to 6% for both the AV and PV.

The alignment of the collagen fibers was quantified using small angle light scattering (SALS). In this technique, a laser is passed through the tissue specimen, producing a scattered light pattern representing the distribution of fiber angles. An orientation index (OI) was defined as the angle that contains one half of the total area under the scattered light pattern distribution. These values were then converted to a normalized orientation index (NOI), such that the NOI ranged from a value of 0% for a randomly aligned fiber network to 100% for a perfectly aligned network. At 0 mmHg, the NOI, or degree of fiber alignment, was consistently ~35% for the AV and ~50% for the PV across several regions of the leaflets. As the pressure was increased from 0 to 4 mmHg, there was a significant increase in NOI in both types of valves. Similar to the behavior of the crimp period, fiber alignment did not increase significantly beyond 4 mmHg in the AV and 20 mmHg in the PV. At 90 mmHg, both valves had approximately the same NOI around 60%. These results for both crimp and fiber alignment are consistent with the observed stress-strain behavior of leaflet tissue. The large increases in crimp period and fiber alignment from zero to low pressures correspond to the elastin-dominated regime of the stress-strain curve (Fig. 2a), with high extensibility at low stresses, while the minimal increases in crimp period and fiber alignment at higher pressures correspond to the stiffer, collagen-dominated regime with low extensibility and rapidly increasing stress.

Collagen cross-links are also thought to have a significant role in leaflet mechanics, and they may even serve as a better indicator of leaflet behavior than a simple measurement of collagen content. While studying the relationships of collagen cross-links and collagen content with the mechanical behavior of human AV leaflets, Balguid et al. found a significant positive correlation between the leaflet modulus of elasticity, extracted from the linear portion of the stress-strain curve, and collagen cross-link concentration in the circumferential direction [103]. In contrast, there was no correlation between modulus and collagen content. There was also no correlation in the radial direction between

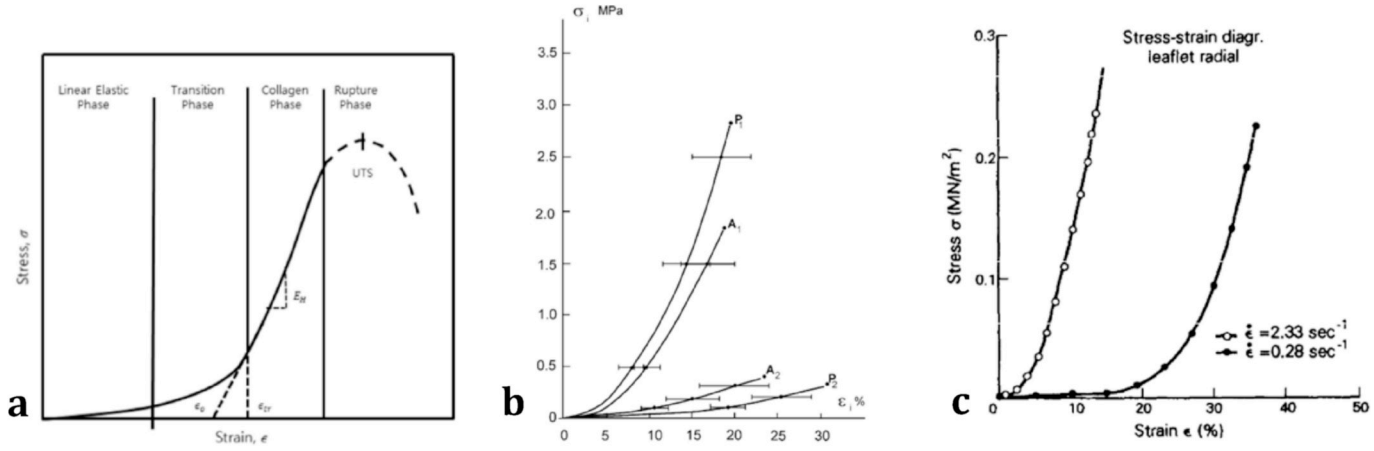

Fig. 2. (a) Typical stress-strain curve from uniaxial tensile loading of soft biological tissues, including heart valve leaflets [21,104]. (b) Uniaxial stress–strain curves for human PV and AV leaflets (P_1/P_2, PV leaflets in circumferential/radial direction; A_1/A_2, AV leaflets in circumferential/radial direction) [81]. (c) Uniaxial stress-strain curves for human AV leaflets showing the influence of differing strain rates [104]. Figures reprinted with permissions from Elsevier and Oxford University Press.

Table 2
Comparison of properties of individual layers isolated from porcine AV leaflets and tested under uniaxial tension. The elastic modulus was calculated at a stress of 300 kPa. The extensibility was defined as the point at which a tangent drawn to the stress-strain curve at 300 kPa crossed the x-axis. N.S. = not significant [31]. Table reprinted with permission from Elsevier.

	Young's modulus (kPa)		Extensibility (%)		Slope of stress relaxation curve	
	Circumferential	Radial	Circumferential	Radial	Circumferential	Radial
Fibrosa	13.02 ± 5.139	4.56 ± 2.337	19.40 ± 4.971	27.77 ± 13.532	−6.46 ± 0.916	−8.62 ± 2.018
Ventricularis	7.41 ± 1.694	3.68 ± 0.550	21.79 ± 6.581	62.66 ± 16.101	−8.15 ± 1.851	−9.07 ± 1.299
Significance	$p < 0.011$	N.S.	N.S.	$p < 0.0001$	$p < 0.023$	N.S.

modulus and cross-link concentration or between modulus and collagen content. Since collagen is a primary load-bearing element in the circumferential direction, but not radially, these findings suggest that the collagen cross-links must act in conjunction with the predominant collagen fiber orientation to have an effect. Thus, it was emphasized that the entire collagen architecture, including collagen content, cross-links, and fiber orientation, must be considered as a whole.

While most studies of leaflet properties utilize intact leaflets, Vesely and Noseworthy performed an interesting experiment with porcine AV leaflets where they separated the fibrosa and ventricularis and measured their properties independently (Table 2) [31]. Although total leaflet extensibility under uniaxial testing in the radial direction was 60%, the isolated fibrosal tissue had a radial extensibility of only ~20%. The authors explained that unfolding of the corrugations in the fibrosa accounted for the remaining ~40% extension. Vesely further isolated elastin structures from the fibrosa and ventricularis and compared their properties to the whole leaflet [55]. At max leaflet extension in the circumferential direction, the stiffness of aortic valve elastin was only 2.1 N/m vs. 3500 N/m for the whole leaflet. Also, the elastin stiffness increased from 0.31 N/m at low loads to 2.1 N/m at high loads, while the leaflet stiffness increased from 3.1 N/m to 3500 N/m, which is consistent with the observation that uncoiled collagen is the main load-bearing element during diastole. By comparing the stress-strain curves of isolated elastin vs. the individual layers, it was observed that only a small amount of tension in either direction in the fibrosa was carried by elastin, while the majority of tension was carried by collagen. In the ventricularis, circumferential loading was shared equally by elastin and collagen at strains up to 25%, while the radial response was dominated by elastin. Note that in these studies, the microdissection process for separating the fibrosa from the ventricularis required the severing of many fibrous connections. Thus, the properties of the whole intact leaflet are not necessarily the direct summation of measurements from the individual layers. Indeed, the authors found that once the layers are isolated, the fibrosa elongates and the ventricularis shrinks. This occurs primarily in the radial direction and suggests that, in the intact leaflet, the ventricularis is preloaded in tension [106]. A primary limitation of isolating elastin, as discussed by Vesely, is that this removes the collagen bundles that fill the voids within elastin structures. As a result, the elastin structures collapse more readily during stretching and can show increased extensibility and compliance.

At low physiological forces, the interaction of GAGs with collagen fibers in the still-crimped state is believed to contribute to the viscoelastic behavior of bulk tissue. To explore this hypothesis, Eckert et al. compared samples of intact porcine AV leaflet tissue with samples where the GAGs had been enzymatically removed [61]. The samples were tested both biaxially at high stress and under flexure to achieve low stresses. Hysteresis was used as a measure of viscoelasticity, and it was calculated as the difference in the areas below the loading and unloading curves and expressed as a percentage of the area below the loading curve. The high-stress biaxial tests showed that GAGs had a negligible effect both on hysteresis and on the general stress-strain behavior. However, the flexural tests at low stresses and strains showed a significant drop in hysteresis, from ~35% in the control samples to ~25% in tissues where GAGs were removed. Thus, at low physiological stress and strain levels, GAGs do contribute to some amount of viscous dissipation, or damping effects. However, at higher stresses and strains, these effects are overshadowed by the dominant behavior of collagen and elastin.

2.2.3. Tensile properties

2.2.3.1. Uniaxial testing. The tissue-level mechanical properties of valve leaflets, as determined by uniaxial and biaxial tensile tests, are highly anisotropic and reflect the directional arrangement of collagen and elastin fibers in the fibrosa and ventricularis. Specimens for uniaxial testing are typically prepared by cutting leaflet tissue into rectangular strips along either the circumferential or radial direction. They are then mounted in grips that stretch the specimens lengthwise at a predefined strain rate. Testing results from various studies showed that human and porcine valve leaflets follow a stress-strain curve typical of soft biological tissues (Fig. 2). Also, they are much stiffer and stronger in the circumferential direction than in the radial direction, while they have a higher extensibility in the radial direction (Table 3). These observations are all consistent with the predominantly circumferential orientation of collagen and elastin fibers. While these

Table 3
Mechanical properties of human and porcine valve leaflets under uniaxial tension. *Calculated at specimen stress level of 1.0 MPa **Calculated as the slope of the linear part of the stress-strain curve. ***Calculated as the slope a fitted line through the portion of the stress-strain curve between stress levels of 0.4–1.0 MPa for circumferential specimens and 0.05–0.1 MPa for radial specimens. Table partially reprinted with permission from Oxford University Press.

	Young's modulus (MPa)		Ultimate strength (MPa)		Ultimate strain (%)		Reference
	Circumferential	Radial	Circumferential	Radial	Circumferential	Radial	
Pulmonary	16.05 ± 2.02*	1.32 ± 0.93*	2.78 ± 1.05	0.29 ± 0.06	19.40 ± 3.91	29.67 ± 4.41	[81]
Aortic	15.34 ± 3.84*	1.98 ± 0.15*	1.74 ± 0.29	0.32 ± 0.04	18.35 ± 7.61	23.92 ± 3.94	[81]
	$P > 0.2$	$P = 0.002$	$P = 0.049$	$P > 0.2$	$P > 0.2$	$P = 0.043$	
Aortic	15.6 ± 6.4**	2.0 ± 1.5**	2.6 ± 1.2	0.42 ± 0.24	21.9 ± 10.6	29.8 ± 13.9	[103]
Aortic	14.55 ± 3.7***	1.57 ± 0.18***					[104]
Porcine aortic	7.78 ± 1.7***	1.28 ± 0.34***					[104]
Porcine aortic	42.30 ± 4.96*	5.33 ± 0.61*	1.58 ± 0.26	0.55 ± 0.11	7.26 ± 0.69	8.57 ± 0.80	[107]

trends are also consistent across different studies of leaflet mechanical properties, there is significant variability in the actual data. For example, the circumferential Young's modulus of the porcine AV leaflet was reported to be 7.78 ± 1.7 MPa by Mavrilas and Missirlis [104] and 42.30 ± 4.96 MPa by Kalejs et al. [107]. This variability can be attributed to a few major factors, including normal biological variability amongst the specimens, differences in data analysis (e.g. calculation of elastic modulus), and differences in experimental conditions (e.g. strain rate and specimen size) [104,108]. Another interesting observation is that the ultimate strengths in the circumferential direction are roughly an order of magnitude greater than the estimated maximum *in vivo* leaflet stresses from Section 2.2.1 Mechanical environment. Also, note the minimal difference between the mechanical properties of human AV and PV leaflets as recorded by Stradins et al. (Fig. 2b) [81].

As discussed in Section 2.2.2 Micromechanics, the leaflet stress-strain curve contains a highly non-linear transition region representing the transfer of load from elastin to collagen, followed by a more linear (but still slightly non-linear) elastic region dominated by the collagen fibers. Mavrilas and Missirlis therefore defined a transition strain ε_{tr} which corresponds to the end of the transition region and beginning of the post-transition region [104]. Calculated values for ε_{tr} were significantly different between fresh human and porcine AV leaflets in both the circumferential (6.80 ± 1.96% human vs. 16.80 ± 6.50% porcine) and radial (6.90 ± 1.69% human vs. 11.60 ± 3.10% porcine) directions. These results highlight the inherent mismatch in mechanical properties between human and porcine valves, which is a significant concern affecting the durability of porcine bioprostheses. The authors also tested two radial strips at different strain rates (2.33 s^{-1} and 0.28 s^{-1}) and showed that a higher strain rate corresponded to a lower ε_{tr} (Fig. 2c). This strain rate dependency is a viscoelastic phenomenon characteristic of soft biological materials. Leaflet viscoelasticity will be the subject of further discussion in Section 2.2.6 Viscoelasticity.

2.2.3.2. Biaxial testing. While uniaxial tests provide important qualitative information about leaflet properties, leaflets in diastole are known to be stressed multiaxially (see Section 2.2.1 Mechanical environment). Therefore, tension tests performed under biaxial loading conditions can provide much more accurate representations of leaflet micromechanics (e.g. fiber kinematics) and overall tissue-level behavior, and biaxial tests are frequently used to generate and validate constitutive models [58,86,94,100,102,109–113]. Billiar and Sacks tested porcine AV leaflets biaxially and used SALS to map the fiber architecture [109]. Square-shaped specimens were loaded at quasi-static strain rates (4–15%/s radially and 1–4%/s circumferentially) to pre-determined membrane stresses in the circumferential (T_{CC}) and radial (T_{RR}) directions according to seven different loading protocols: T_{CC}:T_{RR} = 10:60, 30:60, 45:60, 60:60, 60:45, 60:30, and 60:2.5 (N/m). Membrane stress (N/m) was used, rather than three-dimensional stress (N/m^2), since the layers within the leaflet are not homogeneous and do not bear load equally. The equibiaxial test case (60:60 N/m) showed extensibility to be much greater in the radial direction than the circumferential direction, a finding qualitatively consistent with the results of uniaxial tests. SALS analysis of the progression of loading protocols showed that as the ratio of radial to circumferential loading increases, the collagen fibers undergo large rotations which allows for high radial strains while tending towards contraction in the circumferential direction (Fig. 3). This action even results in negative strains in the circumferential direction in glutaraldehyde-treated specimens. The effect of this mechanical coupling on leaflet deformation can be lost during uniaxial tests due to the non-physiological loading conditions and because uniaxial testing specimens encompass a smaller percentage of the leaflet area with fewer intact fibers.

2.2.4. Flexural properties

Vesely and Boughner performed the first known experiments on heart valve leaflets in flexure [30]. They tested both fresh and glutaraldehyde-treated porcine AV leaflets, using a modified version of the three-point bending method. Circumferential strips were bent against their natural curvature (fibrosa on the outside of the bend) to reverse curvatures ranging from 0 to ~1.5 mm^{-1}. These curvatures were well beyond the physiological range but intended to simulate extreme bending patterns observed in functioning bioprosthetic valves. Bending moment vs. specimen curvature was plotted to create bending curves and bending stiffnesses were calculated from the slopes of these curves. The bending curves showed distinguishable regions similar to those of Fig. 2a: low bending stiffness at low curvatures, increasing bending stiffness at higher curvatures, then decreasing bending stiffness at the highest curvatures. One important consideration when assessing leaflet flexural properties is the location of the neutral axis. This is not trivial since the properties of the fibrosa, spongiosa, and ventricularis vary greatly, and the total thickness of the leaflet tissue is also highly variable. Here, the authors used polarized light microscopy to measure the strains within a bent sample, locating the neutral axis at a distance 40% into the thickness of the fibrosa. This location was largely independent of the local thickness of the spongiosa and ventricularis. It was estimated that overall, the neutral axis was located approximately 1/6th of the total thickness away from the surface of the fibrosa. Thus, the authors suggested that simple (Euler-Bernoulli) beam theory, which assumes a centrally located neutral axis, could not accurately describe leaflet behavior and that an analytical solution could not be obtained. Instead, bending stiffness vs. thickness was plotted (Fig. 4a), and the curve of best fit gave the equation for bending stiffness S as

$$S = 14.3 \cdot t^{1.14}, \tag{3}$$

where t is the leaflet thickness in mm and S has units of nN·m^2. In contrast, simple beam theory gives the bending stiffness of a beam with rectangular cross section as

$$S = EI = \frac{Ebt^3}{12}, \tag{4}$$

where E is the elastic modulus of a homogeneous isotropic material, I is the area moment of inertia of the rectangular cross section, and b is the width, which is assumed to be constant. Eq. (4) then takes the form

$$S = At^3, \tag{5}$$

where A is a constant. Comparing Eq. (3) with Eq. (5), the authors concluded that simple beam theory cannot adequately describe the flexural behavior of porcine leaflets.

However, later work from the Sacks group, described in the following paragraphs, relied heavily on simple beam theory to model leaflet flexural properties. In contrast to Vesely and Boughner, their strain analysis located the neutral axis very near the center of the leaflet thickness, at 40–45% of the total leaflet thickness from the fibrosal surface [50], which supports the use of simple beam theory. This discrepancy in neutral axis location could be explained by differences in experimental setup – Vesely and Boughner pre-loaded their specimens, bent them in reverse curvature only, and bent them to very high non-physiological curvatures. These actions may have mechanically activated the collagen in the fibrosa, resulting in a stiffer fibrosa compared to what was observed by Sacks et al. at lower, physiological curvatures.

In one study by the Sacks group, Merryman et al. investigated the effect of porcine AV interstitial cell (AVIC) contraction on leaflet flexural stiffness [70] using a three-point bending method developed by Engelmayr et al. [114]. The authors chose this approach over uniaxial testing since leaflet flexure would be more sensitive to the low strains and stresses generated by the cells – AVIC contraction in response to KCl creates forces of only 0.31–0.66 mN in the circumferential direction and 0.11–0.23 mN in the radial direction [74]. Additionally, flexure is a natural deformation mode, and it can be used to load different layers in

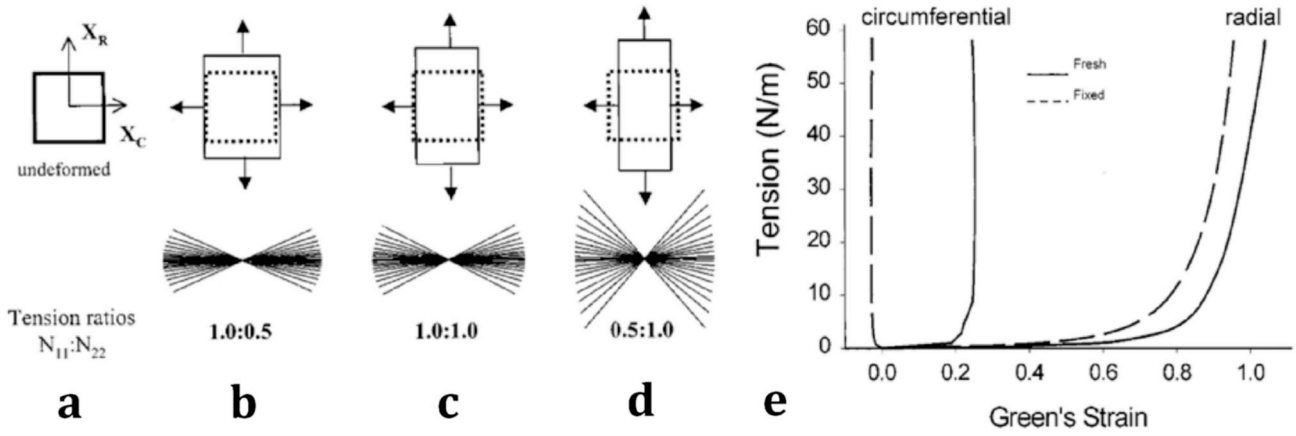

Fig. 3. (a) Schematic of biaxial test specimen. (b–d) Collagen fibers (represented schematically by the fanned lines) within the leaflet undergoing rotations as the radial load becomes larger with respect to the circumferential load. This permits very large radial strains while causing contraction circumferentially. (e) Stress-strain curves from biaxial testing of fresh and glutaraldehyde-fixed porcine AV leaflets, showing mechanical anisotropy. The fixed specimen contracts circumferentially due to strong in-plane coupling [109]. Figures reprinted with permission from the American Society of Mechanical Engineers.

tension or compression, allowing one to study the mechanical properties of individual layers while preserving leaflet integrity [27,115]. In the experiments, leaflet strips cut from the belly region in the circumferential direction were bent with (WC) and against (AC) their natural curvature (Fig. 4c), while KCl was used to induce cellular contraction. To account for large deflections, the applied moment M was expressed as a function of the cumulative change in curvature $\Delta\kappa$, from the reference configuration, using the generalized Euler-Bernoulli moment-curvature equation

$$M = E_{\text{eff}} I \Delta\kappa, \tag{6}$$

where E_{eff} is the instantaneous effective stiffness for any given $\Delta\kappa$ and I is the area moment of inertia of a rectangular cross section. Note that $\Delta\kappa$ is relevant here, rather than the actual curvature κ, because of the pre-existing natural curvature in the reference configuration. Also, E_{eff} describes the behavior of the leaflet as a whole and does not represent any intrinsic material properties. The $M - \Delta\kappa$ relationship had bi-directional linearity at curvatures between $\pm$ 0.3 mm^{-1}, in the physiological range, compared to the overall non-linearity across a larger range of curvatures shown by Vesely and Boughner [30]. Cell contraction due to KCl resulted in a 48% increase in E_{eff} for AC specimens (from 703.05 $\pm$ 132.58 kPa to 1040.66 $\pm$ 229.01 kPa), while the WC specimens saw only a 5% increase which was not statistically significant (from 491.69 $\pm$ 135.17 kPa to 516.50 $\pm$ 159.00 kPa). It is likely that this difference in behavior between AC and WC specimens is due to leaflet microstructure. Under WC loading, the ventricularis is in

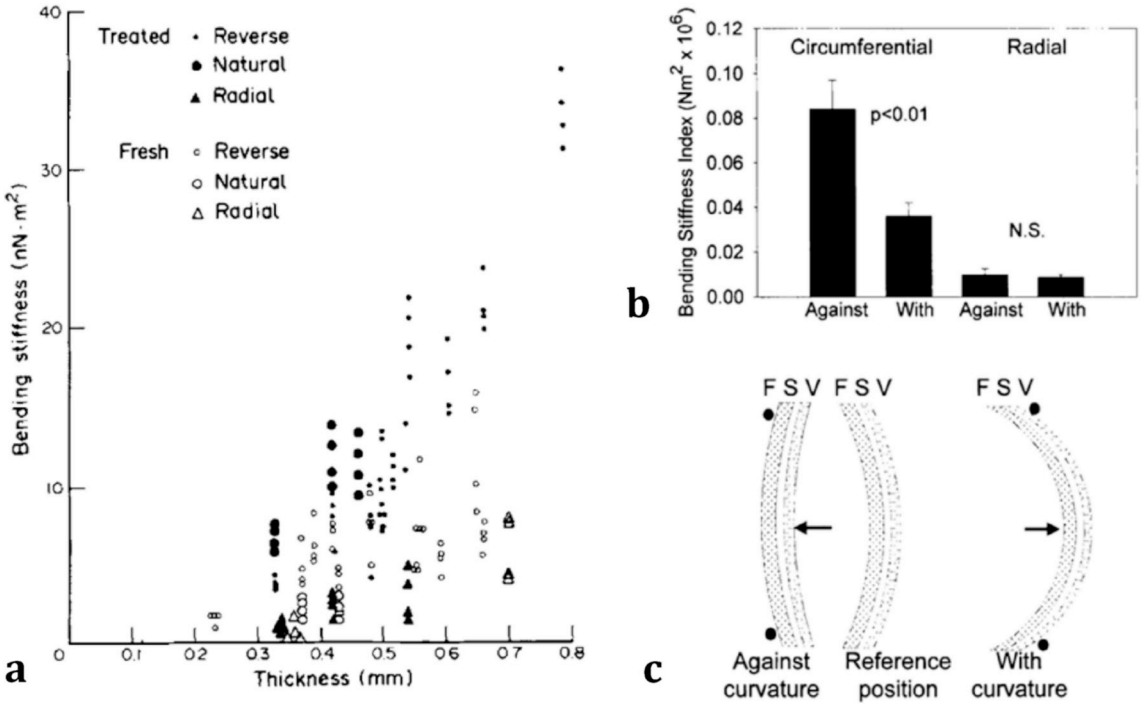

Fig. 4. (a) Bending stiffness of circumferential strips of porcine AV leaflet bent in the reverse and natural directions, plus radial strips bent in the reverse direction [30]. (b) Bending stiffness index of glutaraldehyde-treated porcine AV leaflets, showing that bending stiffness in circumferential strips is dependent on bending direction, while bending stiffness in radial strips is independent of bending direction [118]. (c) Schematic of flexural testing configuration showing orientations of the fibrosa (F), spongiosa (S) and ventricularis (V) with respect to the bending direction [118]. Figures reprinted with permissions from Elsevier and Wolters Kluwer Health.

tension, while in AC loading, the fibrosa is in tension. Disregarding microstructure, one might expect that cell contraction would have a pronounced effect in restricting extension of the layer in tension, while the effect of cell contraction would be negligible in the layer already under compression. The authors speculated that the reason the experiments show otherwise is that there is compliant elastin present in the ventricularis to accommodate the contraction. In contrast, the fibrosa is comprised mainly of collagen, so that in tension the cell contraction imposes significant stress on the collagen to resist flexure.

In a complementary study from the Sacks group, Mirnajafi et al. investigated the flexural properties of the commissural region in porcine AV leaflets using a cantilever beam method and a modified implementation of elastica [116]. The elastica theory describes large-scale deflections of an idealized one-dimensional object. It assumes a linear-elastic relationship between moment M and the finite curvature κ of the object such that

$$M = EI\kappa, \tag{7}$$

where EI is the bending stiffness [117]. The authors assumed the specimens to have zero curvature ($\kappa = 0$) in the reference configuration and showed that the elastica could accurately predict the deformed leaflet shape, demonstrating a shape error of ± 7.5% compared to experimental observations. The effective tissue modulus E_{eff} was then calculated by an inverse solution of the Euler-Bernoulli equations:

$$\frac{y''}{[1 + (y')^2]^{3/2}} = -\frac{M(x)}{E_{\text{eff}} I}, \tag{8}$$

where $M(x)$ is the moment resulting from the applied point load, I is the area moment of inertia of the cross-section, $y = y(x)$ is a parameterization of the predicted deformation of the leaflet, and x is the distance from the aortic root. The effective modulus was observed to be highly dependent on the direction of flexure. Flexing of the leaflets by an angle $\varphi = 30°$ in the direction along forward flow gave an effective modulus of 42.63 ± 4.44 kPa, while flexing the same amount in the non-physiological reverse direction gave an effective modulus of 75.01 ± 14.53 kPa. These values are significantly lower than the E_{eff} reported by Merryman et al. for the belly region [70]. It was suggested that having a stiffer belly region would avoid wrinkling of the opened leaflet and permit smoother valve function. Whereas E_{eff} in the belly region was constant across physiological curvatures, E_{eff} at the commissures decreased linearly with increasing φ due to tissue buckling at the commissure-aortic root junction. The authors speculated that this behavior presents a functional advantage since a lower E_{eff} at a higher angle of flexure would minimize the leaflet opening force.

One common finding among the flexural studies described this section, both from Vesely and Boughner and from the Sacks group, is that circumferentially-oriented fresh leaflet specimens are bent more easily with the direction of natural curvature (WC) rather than against it (AC) (Interestingly, Vesely and Boughner found that the reverse was true for glutaraldehyde-treated leaflets. This result, in turn, conflicts with the observations of Gloeckner et al. for such treated specimens (Fig. 4a) [30,70,116,118]). As mentioned previously, leaflet microstructure is responsible for this mechanical anisotropy. In the AC direction, the tension layer is the stiffer collagen-filled fibrosa, while in the WC direction it is the more compliant ventricularis [31]. Gloeckner et al. showed that the anisotropy occurs only along the circumferential direction, as bending stiffness along the radial direction showed no dependence on bending direction (Fig. 4b) [118]. This is due to the primarily circumferential arrangement of collagen in the fibrosa. When the fibrosa is extended radially, orthogonal to the predominant direction of its collagen fibers, its Young's modulus is closer to that of the ventricularis [31]. The smaller amount of radially-aligned collagen, compared to circumferentially-aligned collagen, in both the fibrosa and ventricularis also explains why leaflets are bent more easily along the radial direction than along the circumferential direction [30,118].

2.2.5. Fatigue

While there appear to be no documented experiments on fatigue in fresh leaflet tissue, fatigue of glutaraldehyde-treated tissues is better studied due to its implications for the durability of BHVs. We present here a just few examples which are informative of the mechanics of native tissues as well. Broom conducted some of the first fatigue tests of glutaraldehyde-treated leaflet tissue [28,119,120]. He subjected specimens from porcine aortic valves and from bovine and porcine mitral valves to stress-based accelerated fatigue tests in uniaxial tension. Histology of the mitral tissue showed a marked reduction in the degree of collagen fiber crimping after 18 million cycles at 2 MPa, the appearance of longitudinal cavities indicating the loss of matrix material after 75 million cycles at 4 MPa, and the gross disruption of fiber bundles after 175 million cycles at 2.3 MPa. Broom also observed that the stiffness of the treated tissue increased with increasing number of cycles. He attributed this effect to the observed reduction in collagen crimping, although an alternative explanation later offered by Sacks is that the stiffening could be caused by the progressive alignment of collagen fibers [121]. Cyclic compressive flexure of high-pressure-treated AV leaflets additionally resulted in kinking, or regions of localized flexural collapse of collagen bundles. Low-pressure-treated specimens, where collagen crimp was preserved, did not have this effect, suggesting that collagen fiber crimping has a role in accommodating deformation during compressive flexure in untreated tissues. Broom noted that in healthy living tissue, any breakdowns in the fibers and matrix would normally be repaired. However, in preserved tissues these fatigue effects are likely a major mechanism facilitating the development of SVD [4,18].

Sacks later reported on fatigue testing under biaxial stress conditions in which cyclic loading induced a gradual increase in structural stiffness in the radial direction of glutaraldehyde-treated porcine AV leaflet tissue [121]. In contrast to the uniaxial data from Broom, almost no change in the circumferential stiffness was observed with increasing number of cycles. The decrease in radial extensibility was attributed to stiffening of the collagen fiber network and a change in alignment of the fibers. These experimental studies were performed on tissue extracted from the center, belly region of the leaflets. However, as remarked by the author, roughly 50% of the leaflet area has a distinct structure from that of the belly and experiences very different loading histories over a cardiac cycle. Consequently, the fatigue properties of the various regions of the leaflet are likely to be quite different.

Gloeckner et al. performed flexural fatigue tests on glutaraldehyde-treated porcine AV leaflets, using a similar three-point bending setup as Merryman et al. and Mirnajafi et al. [70,116,118]. First, porcine bioprosthetic heart valves were subject to accelerated testing for 0, 50, 100 and 200 million cycles. Then leaflet strips were cut in the circumferential and radial directions and bent both with their natural curvature (WC) and against their curvature (AC) (Fig. 4c) to make four sample sets: circumferential WC, circumferential AC, radial WC, and radial AC. The formula from Euler-Bernoulli beam theory for the maximum displacement of a simply supported beam with a central point load was used to solve for bending stiffness EI

$$EI = \frac{PL^3}{48\gamma_{\max}}, \tag{9}$$

where $\gamma_{\max}$ is the maximum displacement, P is the applied force to cause bending, and L is the length of the specimen between its support posts. Since a leaflet is not homogeneous through its cross section and large displacements were applied, it would be inaccurate to accept EI as the true bending stiffness. Instead, EI was reported as a bending stiffness index (BSI) which was used only to compare relative bending stiffnesses between sample sets. Circumferential BSIs were significantly greater than BSIs in the radial direction. As mentioned previously, the circumferential samples also showed dependence on bending direction, with circumferential AC BSI greater than circumferential WC BSI. The

radial samples showed no dependence on bending direction. BSI decreased with number of cycles for all four sample sets. Rate of change in BSI was greatest for the circumferential AC samples – after 200 million cycles, their BSI decreased by about 80% of the uncycled BSI value, while other sample sets decreased by less than 40%. Since the fibrosa is the primary contributor to bending stiffness of the circumferential AC samples, these results indicate that the fibrosa experiences the greatest fatigue effects, perhaps due to its higher collagen content, while the ventricularis is affected to a lesser extent. It was suggested that this loss in flexural rigidity could be due to fiber debonding [121,122], but the exact mechanisms are still unclear and would be an interesting subject for further study. In any case, it is quite clear that there is a need for further fatigue experimentation of both fresh and treated tissues. These types of material characterizations are essential to understanding, and ultimately predicting, the long-term change in properties and function of the underlying tissue. A fatigue study incorporating fresh leaflet tissue could, in addition to providing valuable insight on native tissue mechanics, ultimately assist in better design and processing of BHVs.

2.2.6. Viscoelasticity

The micromechanics of valve leaflet tissue also dictate its complex time-dependent mechanical behavior. Soft biological materials are generally known to exhibit viscoelastic behaviors such as strain-rate sensitivity, hysteresis, creep, and stress relaxation [123,124]. Uniaxial testing of leaflet specimens can elicit these viscoelastic effects, even after preconditioning (Fig. 5a and b) [79,104,125–128]. However, in many studies using biaxial tests, which should more closely approximate physiological conditions, leaflet specimens exhibited only stress relaxation while strain rate sensitivity, hysteresis, and creep were minimal [50,100,129–131]. Yet, low-frequency (0.5–5 Hz) dynamic bulge testing of mitral valve leaflet tissue showed that the loss modulus increased steadily with increasing frequency [132], and Jett et al. found that biaxial loading did elicit some strain-rate dependence (decreasing extensibility with increasing loading rate) in porcine mitral valve leaflets if the subsequent analysis accounted for the effects of pre-conditioning stretches [113]. Recently, Anssari-Benam et al. performed equibiaxial tests showing significant strain rate dependency in porcine AV leaflets, although the samples were not pre-conditioned [133]. With such variations in results, likely stemming from the lack of a standard test protocol, this is certainly an area that requires further study.

Various mechanisms for leaflet viscoelasticity have been proposed, but the exact contributions and interactions occurring within the leaflet structure are not yet well-understood. While GAGs are known to impart viscoelastic properties, the removal of GAGs from native tissue has been shown to only reduce, but not eliminate, hysteresis and stress relaxation [61,131]. Thus, there must be other factors involved. Collagen structures have been shown to be viscoelastic – they can provide an immediate viscoelastic response to loading, but their contribution to longer-term behavior, such as creep and stress-relaxation, is believed to be negligible [134,135]. Sliding contact between collagen fibers has also been proposed as a source of energy loss [136]. Another potential mechanism for leaflet viscoelasticity and its dependence on loading conditions lies in the kinematics of collagen fibers and shear-thinning (decrease in viscosity with increase in shear rate) of the surrounding GAG matrix [130,137]. Uniaxial loading permits larger rotations and increased alignment of collagen, resulting in greater shearing of the

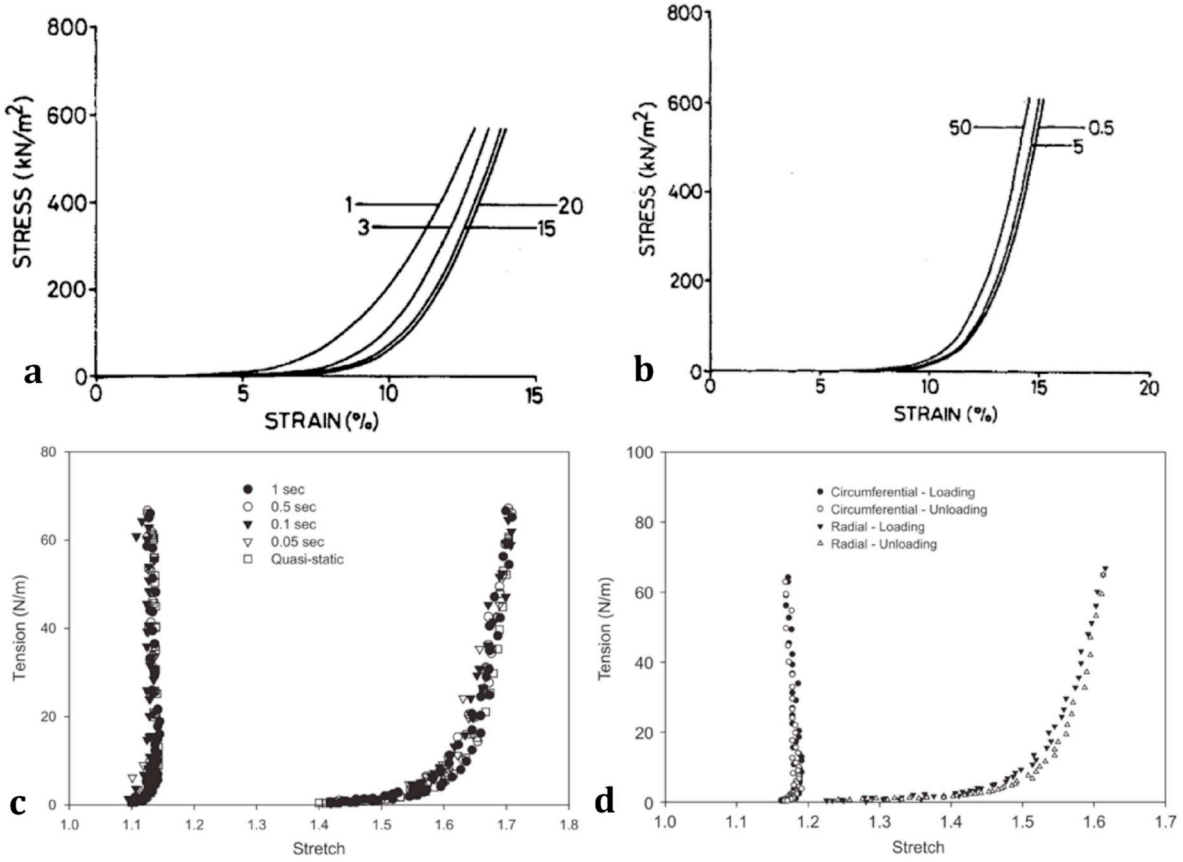

Fig. 5. (a) Representative uniaxial stress-strain curves for a circumferential strip during cycles 1, 3, 15, and 20 of preconditioning. The curves after cycle 20 overlay that of cycle 20, indicating that the mechanical response has stabilized due to the preconditioning. (b) Representative uniaxial stress-strain curve of a preconditioned circumferential strip at extension rates of 0.5, 5, and 50 mm/min, showing some strain rate dependence [125]. (c) Representative biaxial tension–stretch curves for the porcine AV leaflet in the circumferential (left) and radial (right) directions at loading-unloading half-cycle times of 1, 0.5, 0.1, 0.05, and 15 s (quasi-static), showing negligible strain rate dependence. (d) Representative loading-unloading curves for the AV leaflet, showing negligible hysteresis in the circumferential direction and a small amount in the radial direction [100]. Figures reprinted with permissions from Elsevier and John Wiley and Sons.

matrix gel, while in biaxial loading the rotation of the fibers appears to be constrained so that shearing occurs to a lesser degree [138].

One commonly used approach to viscoelastic constitutive modeling of heart valve leaflet tissue is the quasilinear viscoelastic (QLV) model [139–142]. This model was originally proposed by Fung and is commonly used to model soft tissue biomechanics [123,143]. The primary assumption in this theory is that the history of the stress response (relaxation function denoted by $K(\lambda, t)$) can be expressed as

$$K(\lambda, t) = G(t)T^{(e)}(\lambda), \qquad G(0) = 1, \tag{10}$$

which is a combination of a relaxation component (reduced relaxation function $G(t)$) and the elastic response $T^{(e)}(\lambda)$ to a step increase of stretch λ [123]. Then, by taking an infinitesimal change in stretch $\delta\lambda(\tau)$ and superposing it on a specimen in a state of stretch λ at time τ, the stress response at time t (for $t > \tau$) is the convolution integral

$$T(t) = \int_{-\infty}^{t} G(t-\tau)\dot{T}^{(e)}(\tau)d\tau, \tag{11}$$

where $T(t)$ is the tensile stress at time t and represents the sum of past responses to all the infinitesimal changes in stretch. After some manipulation, Eq. (11) can be rewritten as

$$T(t) = T^{(e)}[\lambda(t)] + \int_{0}^{t} T^{(e)}[\lambda(t-\tau)]\frac{\partial G(\tau)}{\partial \tau}d\tau, \tag{12}$$

which describes the tensile stress at time t as the sum of the instantaneous elastic response and a contribution from its history, which is usually negative. The functions $T^{(e)}(\lambda)$ and $G(t)$ are determined by fitting of experimental stress relaxation testing data.

2.2.6.1. Uniaxial testing. One disadvantage of QLV is that it assumes an instantaneous stretch via a step function, which is impossible to achieve in the physical world. The closest approximation for any testing apparatus is to ramp up to the desired displacement as quickly as possible. However, during the finite ramping time, the material has already begun to relax. Thus, information is lost, resulting in erroneous estimates of model parameters. Rather than idealize the physical ramp-up as a step function as in a traditional QLV model, Doehring et al. directly incorporated the ramp-up into their direct-fit QLV model by representing the elastic response with a power law function

$$T^{(e)}(\lambda) = A(\lambda - 1)^{B}, \tag{13}$$

where A and B are fitted parameters [142]. Data for the model was obtained from uniaxial testing of porcine AV leaflets. After fitting the data, both the traditional and the direct-fit approach showed that the C parameter, which indicates viscoelastic capacity of the tissue, increased with strain rate (a "shear-thickening" behavior that could be related to the molecular structure of collagen). However, the traditional method appeared to underestimate C. Comparing the two models to experimental data, the direct-fit model performed better, underestimating stress-relaxation by 14% vs. 48% in the traditional model and overestimating peak stress during cyclic loading by 3% vs. 8% in the traditional model.

Anssari-Benam et al. developed a viscoelastic constitutive model of the AV leaflet based on a Kelvin-Voigt model, using springs to represent the ventricularis and fibrosa and a dashpot to represent the spongiosa [127]. The final model expresses the stress-stretch response in the circumferential and radial directions as

$$T_{11} = \frac{E}{2}(\lambda_1^2 - \lambda_1^{-2}) + 4\eta\left(\frac{\dot{\lambda}_1}{\lambda_1}\right) - 4\eta\dot{\lambda}_1, \tag{14}$$

where T_{11} is the stress component along the direction of uniaxial loading, E is the sum of the stiffnesses of the ventricularis and fibrosa, λ_1 is the elongation in the loading direction, and η is the viscous dissipation coefficient. Due to the leaflet's anisotropy, different values for E and η were used to model the circumferential and radial directions. Experimental data was obtained from uniaxial testing of porcine AV leaflet strips cut in the circumferential and radial directions. The specimens were stretched to failure at strain rates of 6%/min, 60%/min, and 600%/min, and the resulting stress-strain curves showed clear strain rate dependency. The stiffness in the linear region of the stress-strain curves increased from 20.4 ± 0.86 MPa to 37.54 ± 1.45 MPa for circumferential specimens and from 0.71 ± 0.8 MPa to 3.36 ± 0.10 MPa for the radial specimens, indicating rate dependency in both directions. Interestingly, the stress-strain curves for the circumferential specimens all exhibited a transient decrease in stress at about half of the failure stress, which was believed to indicate failure of the ventricularis. Stress-elongation data was fitted to the model to obtain values for E and η in the circumferential and radial directions. There was a decrease in η for both circumferential (675.06 ± 82.15 MPa·s to 18.48 ± 0.99 MPa·s) and radial (49.12 ± 3.47 MPa·s to 4.59 ± 0.66 MPa·s) specimens as strain rate increased, indicating the occurrence of shear-thinning within the spongiosa. To characterize hysteresis and resiliency (i.e. recoverability), a series of successive single-cycle tests were performed on each sample while incrementally increasing the load from 5% to 80% of the observed load at failure. Strain rate was kept constant at 60%/min. Resilience was quantified by taking the ratio of the area below the unloading curve to the total area below the loading curve. This ratio was consistently smaller for circumferential specimens compared to radial specimens, indicating less resilience in the circumferential direction, and it corresponded with a greater amount of irreversible elongation (~2.5% circumferential vs. ~2.1% radial) at the end of the test.

The authors also characterized the creep and stress-relaxation responses of porcine AV leaflets, using a viscoelastic constitutive model based on Maxwell elements [128]. For the stress-relaxation experiments, samples were subject to incrementally increasing strain, using a constant strain rate of 60%/min and holding at each strain increment for 300 s. A similar protocol was used for the creep experiments, except that the samples were subject to incrementally increasing loads instead of strains. Fitting of data to a Maxwell model revealed that a double mode was needed to describe stress-relaxation at higher strain increments, and a secondary mode was needed for creep at higher load increments. The authors suggested that this behavior is consistent with leaflet micromechanics, where the mechanical response is dominated by GAGs and elastin at low loads and strains and by collagen at higher loads and strains.

2.2.6.2. Biaxial testing. In contrast to uniaxial viscoelastic results, Grashow et al. observed that the biaxial stress-strain behavior of porcine MV anterior leaflets (MVAL) up to physiological load levels exhibited no dependence on strain rate and a low hysteresis of 12% [130]. Creep and stress relaxation tests showed significant stress relaxation but negligible creep [129]. For the stress relaxation tests, samples were stretched until reaching an equibiaxial tension of 90 N/m and then held at constant strain for 3 h. The amount of stress relaxation was 32.09 ± 0.77% in the radial direction and 24.67 ± 0.93% in the circumferential direction. Stress relaxation under uniaxial loading was significantly different in the radial direction (28.5 ± 1.8%), but not in the circumferential direction (25.2 ± 2.2%). In the creep tests, samples were loaded to an equibiaxial tension of 90 N/m, then held at constant tension for 3 h. The observed lack of creep response is inconsistent with the viscoelastic behavior of other collagenous tissues such as pericardium and ligament. The authors thus described the overall mechanical behavior of the leaflets as *quasi-elastic*, since they observed significant stress relaxation, but no strain rate sensitivity, no creep, and minimal hysteresis.

To explore the mechanisms of this quasi-elastic behavior, the authors analyzed the influence of collagen fibril kinematics on the mechanical response of porcine MVAL tissue under biaxial creep and stress relaxation tests [101]. Small angle X-ray scattering (SAXS) was used to measure the change in collagen fibril angular distribution and the D-period (Fig. 6), which describes the visible 64–68 nm periodic banding

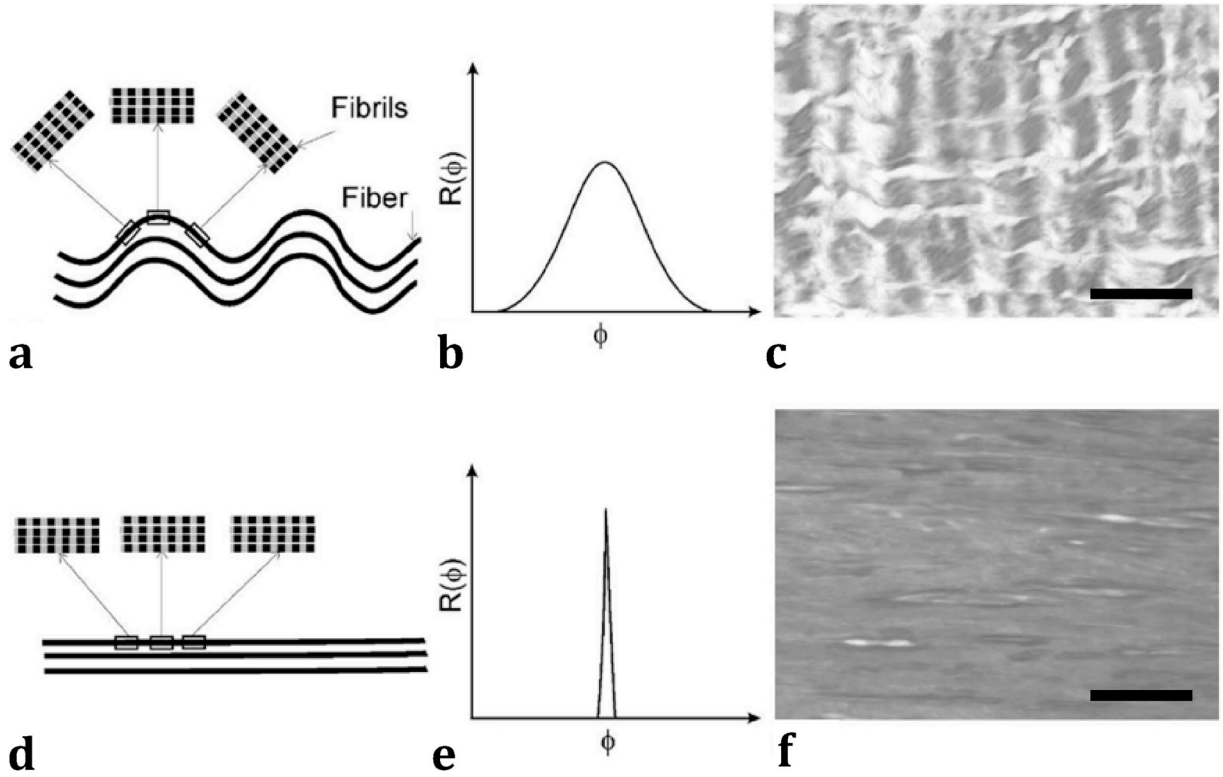

Fig. 6. Schematic demonstrating the change in collagen fibril angular distribution with uncrimping of collagen fibers: (a) crimped collagen fibers; (b) corresponding angular distribution of collagen fibrils in crimped configuration; (c) histological section showing crimped fibers under load-free condition; (d) straightened collagen fibers; (e) corresponding angular distribution of collagen fibrils in straightened configuration; (f) histological section showing straightened fibers under 90 N/m equibiaxial loading [101]. Scale bars in (c) and (f) are ~100 μm. Figures reprinted with permission from the American Society of Mechanical Engineers.

pattern on collagen fibrils that reflects the ordered staggering of collagen molecules within the fibril. The creep tests again showed no change in tissue-level strain, and SAXS revealed that D-period strain was also constant. SAXS also showed no change in fibril orientation or NOI during the creep tests, suggesting that the fibril network "locks up" under constant stress. Under constant strain (stress relaxation testing), the D-period decreased, and the fibril orientation remained the same. It was determined that MV collagen fibrils are not intrinsically viscoelastic, which suggests that there is a transfer of load away from the fibrils that allows them to recover.

AV tissue was also found to behave quasi-elastically, in a manner similar to MV tissue. Stella et al. performed strain rate, creep, and stress relaxation tests on porcine AV leaflets under biaxial loading. Strain rates were varied from quasi-static (0.038 s^{-1} radial and 0.012 s^{-1} circumferential) to physiological (381 s^{-1} radial and 1183.8 s^{-1} circumferential) [100]. Stress-strain behavior and hysteresis had no measurable dependency on strain rate in either the circumferential or radial directions (Fig. 5c and d). Stress relaxation and creep tests were performed in a similar manner as the MV tests described above, except that a maximum tension of 60 N/m was prescribed, instead of 90 N/m. The amount of stress relaxation was 33.28 ± 1.35% in the radial direction and 27.51 ± 1.07% in the circumferential direction. Creep was again negligible in both directions, and there was no discernible difference in response between different loading rates. The authors also obtained transmission electron microscopy (TEM) images showing collagen fibrils interacting with surrounding proteoglycans. It was suggested that these interactions could be responsible for the postulated load transfer away from the elastic collagen fibers, contributing to tissue-level viscoelastic behavior.

2.2.7. Continuum mechanics-based constitutive modelling of native tissues

Several constitutive models have been proposed to describe the continuum mechanical behavior of leaflet tissue, including phenomenological models and bottom-up, structural models [50,144,145]. The simplest phenomenological model is the hyperelastic model, which effectively captures non-linear elastic behavior and anisotropy but neglects viscous effects. In such a model, the stress-strain behavior is defined by a strain energy density function W. The second Piola-Kirchhoff stress $\mathbf{S}$ is then defined as the derivative of the strain energy density function W with respect to the Green-Lagrange strain tensor $\mathbf{E}$, according to principles of thermodynamics:

$$S_{ij} = \frac{\partial W}{\partial E_{ij}}, \quad \text{with } i, j = 1,2. \tag{15}$$

The most commonly used strain energy density function was proposed by Fung and takes the form

$$W = \frac{c}{2}(e^{Q} - 1) \tag{16}$$

$$Q = A_1 E_{11}^2 + A_2 E_{22}^2 + 2A_3 E_{11} E_{22} + A_4 E_{12}^2 + 2A_5 E_{11} E_{22} + 2A_6 E_{22} E_{12}, \tag{17}$$

where c and A_i are fitted material parameters [111,146]. This model has been shown to provide good agreement with the behavior of both human and porcine AV leaflets under biaxial loading [111]. Viscous effects may be excluded since preconditioning has been shown to reduce strain rate sensitivity in soft biological tissues, as mentioned in the previous section [123,130,147,148]. However, the presence of hysteresis suggests that the loading and unloading behavior of the leaflet tissue should be modeled separately [144]. Note that the Fung model is purely phenomenological and is typically used to capture the anisotropic, nonlinear elastic response of biomaterials. The use of the exponential in the strain energy density function is intended to capture the dramatic increase in stiffness of the material at a particular level of stretch that is usually observed experimentally and is associated with

load transfer from the elastin to the collagen fibers [149].

Further complexity can be introduced into a constitutive model by accounting for the leaflet's fibrous structure. Since there is a single preferred collagen fiber orientation in the circumferential direction, the leaflet can be modeled as a fiber-reinforced composite that is transversely isotropic with respect to the collagen fiber axis [150,151]. May-Newman and Yin developed a transversely isotropic model using a strain energy density function based on the strain invariants I_1 and α:

$$W = c_0(e^Q - 1) \tag{18}$$

$$Q = c_1(I_1 - 3)^2 + c_2(\alpha - 1)^4, \tag{19}$$

where c_0, c_1, and c_2 are fitted material parameters. The strain invariants are defined by $I_1 = tr(\mathbf{C}) = tr(\mathbf{B})$ and $\alpha^2 = \mathbf{N}\cdot\mathbf{C}\cdot\mathbf{N}$, where $\mathbf{C} = \mathbf{F}^T\cdot\mathbf{F}$ and $\mathbf{B} = \mathbf{F}\cdot\mathbf{F}^T$ are the right and left Cauchy-Green deformation tensors, respectively, $\mathbf{N}$ is a unit vector defining the preferred fiber direction in the undeformed configuration, and $\mathbf{F}$ is the deformation gradient tensor. The material was also assumed to be incompressible (i.e. $\det(\mathbf{F}) = 1$). This type of model was found to accurately predict stress-stretch behavior of porcine MV leaflets under equibiaxial, off-biaxial, and strip biaxial loading, with correlation coefficients between 0.90 and 0.99 [150]. The authors noted that this model only accounts for positive tensile strains and does not include compression and bending behavior. We remark again that models of this type are phenomenological and do not originate from physical, microstructural arguments.

While these phenomenological models can fit the experimental data accurately, they do not offer much insight into the underlying mechanisms of tissue behavior. Structural models, however, assume that tissue-level behavior can be broken down into individual contributions from its constituent components (i.e. fibers and matrix) [110,152]. Therefore, the development of a structurally-based constitutive model challenges one to consider each constituent carefully and can provide further insight into their properties. Billiar and Sacks used a structural approach, based on the work of Lanir [153,154], to develop the first constitutive model for the stress-strain behavior of AV leaflets [109,110]. Collagen fibers were assumed to carry all external loads, while the contributions of elastin and the ground matrix were deemed negligible. Thus, the structural model consisted of a single fiber material within a single layer of tissue, since modeling of the tri-layered structure (fibrosa, spongiosa and ventricularis) was considered too complex. Time-dependency was also ignored since the authors had experimentally observed negligible viscoelastic effects under the biaxial loading conditions they were attempting to model. An exponential stress-strain law was used to account for the fibers:

$$S_f = A[exp(BE_f) - 1], \tag{20}$$

where S_f is the second Piola–Kirchhoff fiber stress, $E_f = 0.5(\lambda_f^2 - 1)$ is the fiber Green's strain, and λ_f is the fiber stretch ratio. The final form of the constitutive model expresses the Lagrangian membrane stresses (T_{11} and T_{22}) along the biaxial test axes as:

$$T_{11} = \int_{-\pi/2}^{\pi/2} S_f^*(E_f)R(\theta)(\lambda_1 \cos^2\theta + \kappa_2 \sin\theta\cos\theta)d\theta$$

$$T_{22} = \int_{-\pi/2}^{\pi/2} S_f^*(E_f)R(\theta)(\lambda_2 \sin^2\theta + \kappa_1 \sin\theta\cos\theta)d\theta, \tag{21}$$

where $S_f^*(E_f)$ is the exponential stress-strain law modified to account for volume fraction of fibers, $R(\theta)$ is the angular fiber distribution as determined through small angle light scattering (SALS), κ_i are the in-plane shear strains along the biaxial test axes, and θ is the original fiber angle. The model fit well to experimental data from porcine AV leaflets, with average coefficients of determination at 0.95 and above, and it was also able to accurately match data that had not been used for parameter estimation.

The group later developed a fiber recruitment model, which accounts for the gradual recruitment (uncrimping and loading) of the collagen fibers [155]. Rather than following an exponential law, the fiber stress-strain relationship takes the form

$$S_{11}^f = K\int_0^\varepsilon D(x)\frac{\varepsilon - x}{1 + 2x}dx, \tag{22}$$

where K is the fiber elastic modulus incorporating the fiber volume fraction and $D(\varepsilon)$ is a Gamma distribution representing the gradual recruitment of fibers with increasing strain. The uniaxial fiber strain ε is defined by $\varepsilon = \mathbf{N}^T\cdot\mathbf{E}\cdot\mathbf{N}$, where $\mathbf{N}$ is the unit vector parallel to the fiber's longitudinal axis and $\mathbf{E}$ is the global tissue strain state. All components of $\mathbf{S^f}$, except S_{11}^f, are zero since it is assumed that each fiber can only support load along its longitudinal axis. Based on the assumption that the strain energy density of the tissue is the sum of the strain energy density of its constituents (i.e. fibers), the strain energy density function is

$$W = \int_{-\pi/2}^{\pi/2} R(\theta)w(\varepsilon)d\theta, \tag{23}$$

where $w(\varepsilon)$ is the fiber strain energy density. This can then be differentiated with respect to the Green-Lagrange strain tensor to arrive at the constitutive stress-strain law

$$\mathbf{S} = \int_{-\pi/2}^{\pi/2} R(\theta)S_{11}^f(\varepsilon)[\mathbf{N}\otimes\mathbf{N}]d\theta. \tag{24}$$

The authors applied both the exponential (two-parameter) model and the recruitment model to biaxial test data of bovine pericardium. While the two-parameter model provided a better fit ($r^2 = 0.99$), the fiber recruitment model also performed well ($r^2 = 0.92$) and provided some further insight that was not apparent with the two-parameter model. For example, integration of $D(\varepsilon)$ leads to a cumulative distribution function $F(\varepsilon)$ which represents the fraction of fibers of the total that are stretched at a given strain level. Thus, one could predict that at a Green-Lagrange strain of 0.16 in the bovine pericardium used in the study, only ~22% of the collagen fibers would be fully straightened.

While both phenomenological and structural hyperelastic models can fit experimental data quite well under certain loading conditions, it is important to note that the estimated *in vivo* deformation rates ranging from 2.5 to 12.4 s^{-1} are much higher than what typically can be achieved experimentally with commercially available testing equipment [97,99,100]. Additionally, biaxial testing devices are often not readily available. Therefore, to develop an accurate model of *in vivo* leaflet mechanics under uniaxial loading, one must account for rate-dependent effects. To predict the rate-dependent uniaxial response of behavior of porcine AV leaflet specimens, Anssari-Benam et al. developed a transversely isotropic viscoelastic model based on separate elastic (W_e) and viscous (W_v) strain energy density functions [133,156]. The elastic energy density function is broken down further into isotropic matrix (W_e^{iso}) and fiber contributions (W_e^{fibers}):

$$W_e = W_e^{iso}(I_1) + W_e^{fibers}(I_4) = \frac{1}{2}\alpha(exp[\beta(I_1 - 3)] - 1) + \frac{k_1}{2k_2}(exp[k_2(I_4 - 1)^2] - 1), \tag{25}$$

where the first invariant I_1 is the trace of the right Cauchy-Green deformation tensor, the fourth invariant I_4 incorporates the preferred fiber direction, α and k_1 are stress-like material parameters and β and k_2 are dimensionless parameters. The viscous energy density function also comprises matrix and fiber contributions and is expressed as

$$W_v = W_v^{matrix}(I_1, J_2) + W_v^{fibers}(I_1, J_5) = \frac{\eta_1}{4}J_2(I_1 - 3) + \frac{\eta_2}{4}J_5(I_1 - 3) = \frac{1}{4}(I_1 - 3)(\eta_1 J_2 + \eta_2 J_5), \tag{26}$$

where J_2 and J_5 are invariants of the time derivative of the right Cauchy-Green deformation tensor. The terms η_1 and η_2 are viscous material parameters, where η_1 governs the dissipative effects of the GAG matrix and η_2 governs the dissipative effects of fiber-matrix and fiber-fiber interactions. The consitutive model under uniaxial loading conditions takes the final form

$$\begin{aligned}\sigma_{11} = \sigma_{circumferential} &= \alpha\beta(\lambda_1^2 - \lambda_1^{-1})(exp[\beta(\lambda_1^2 + 2\lambda_1^{-1} - 3)]) \\ &+ 2k_1\lambda_1^2(\lambda_1^2 - 1)exp[k_2(\lambda_1^2 - 1)^2] \\ &+ \dot{\lambda}_1(\lambda_1^2 + 2\lambda_1^{-1} - 3)(\eta_1[2\lambda_1^3 + \lambda_1^{-3}] + 2\eta_2\lambda_1^3) \\ \sigma_{22} = \sigma_{radial} &= \alpha\beta(\lambda_2^2 - \lambda_2^{-1})(exp[\beta(\lambda_2^2 + 2\lambda_2^{-1} - 3)]) \\ &+ \eta_1\dot{\lambda}_2(2\lambda_2^3 + \lambda_2^{-3})(\lambda_2^2 + 2\lambda_2^{-1} - 3),\end{aligned} \quad (27)$$

where σ is the Cauchy stress tensor and λ_i are the principal stretches. Experimental stress-stretch data for model fitting was obtained by uniaxial testing of porcine AV leaflets at stretch rates of 0.001, 0.01, 0.1, and 0.5 s^{-1}. The model produced a good fit with $r^2 > 0.97$, and it was also able to predict the uniaxial stress-stretch curve at a stretch rate 0.2 s^{-1} with $r^2 > 0.99$. Analysis of fitted parameters showed that the viscous damping parameters η_1 and η_2 decrease as the deformation rate $\dot{\lambda}$ increases. The decrease of η_1 is characteristic of shear-thinning behavior of the GAGs, while the decrease in η_2 could be due to a decrease in the time afforded for dissipative fiber interactions to occur. The authors also used the model to predict stress-stretch behavior of the AV leaflet at a strain rate of 2.5 s^{-1}, which is the first known prediction of physiological behavior using a continuum-based model where the deformation rate is explicitly included in the constitutive relationship. The predicted stress-stretch curves showed that for a diastolic circumferential stretch of λ= 1.13, the corresponding stress in a circumferentially-oriented leaflet sample under uniaxial loading is ~2.6 MPa. This value is about an order of magnitude higher than previous leaflet stress estimates that did not account for strain rate dependency (see Section 2.2.1 Mechanical environment), and it is also higher than the measured circumferential tensile strength of porcine AV leaflets (Table 3). This constitutive model was later extended to phenomenologically account for fiber dispersion under biaxial deformation [133]. The new model also appeared to overestimate overall physiological stresses, but the authors suggested this discrepancy could be due to regional variations in physiological leaflet deformation that were not captured in the model since it was based only on the belly region. It would be interesting to see if a more comprehensive study could yield more accurate results.

The complex mechanical response of AV leaflet tissue due to the underlying material structure provides a uniquely challenging problem for constitutive model development. Here, we have highlighted a few instances of purely phenomenological models employing the theory of hyperelasticity to capture the strongly anisotropic response of AV leaflet tissue. In contrast to these phenomenological models, the discussed structural models developed by Billiar and Sacks provide additional physical insight which aids in understanding the underlying response of the material. Although suitable structural models are considerably difficult to devise, their development may be crucial to improving our understanding of the material and consequently, our ability to provide a sufficiently predictive constitutive theory. Finally, we note that rate dependency is essential to incorporate when attempting to predict the response of leaflet specimens under uniaxial loading, but there still appears to be general disagreement over the importance of rate dependent effects under biaxial conditions.

3. Materials for prosthetic valves

The polymer class of materials spans a huge range of mechanical properties. In order to simulate the mechanics of the native heart valve, polymers selected for heart valve applications are typically elastomeric, with low stiffness, high elasticity, and low glass transition temperatures so that the materials are soft and rubbery at body temperature. Polyurethanes (PU) have found the most success with several PU-based devices reaching several hundred million cycles during *in vitro* durability testing. Of the myriad of polymeric valves found in the literature, many have been fabricated from commercially available materials, while others have incorporated advanced materials still being developed at the investigative level (Table 5) [1,157,158].

The leaflets in a prosthetic valve must survive a demanding *in vivo* environment, with highly dynamic loading, high strain rates, and anisotropic stretching. Therefore, the mechanical properties of the leaflet material are of fundamental importance in ensuring not only valve competence, but also long-term durability. Both the native valve tissue and the elastomeric polymers typically used to replace it exhibit nonlinear stress-strain behavior that can be characterized as hyperelastic and viscoelastic. To select the optimal materials, due diligence is needed in considering the overall constitutive model as well as the effects of dynamic loading and fatigue. In this section, we will review the mechanical properties of polymers which have been utilized in past and present applications for flexible leaflet heart valves, along with some new materials which show promise for the future.

3.1. Mechanical properties

3.1.1. Elastic modulus and leaflet thickness

A primary mode of deformation in the leaflets is bending. According to Euler-Bernoulli beam theory, the bending stiffness of a section of material is given by *EI*, where *E* is the elastic modulus of the material and *I* is the area moment of inertia. For a rectangular cross-section of the leaflet,

$$I = \frac{bh^3}{12}, \quad (28)$$

where *b* is the width of the cross section and *h* is the thickness of the leaflet. Therefore, the resistance of the leaflets to bending scales increases linearly with *E* and cubically with leaflet thickness *h* [159].

Native leaflet tissue exhibits non-linear stress-strain behavior, and the elastic moduli of polymers are similarly strain dependent. However, the elastic moduli of polyurethanes can be an order of magnitude higher than that of native leaflet tissue in the radial direction [104,160–162]. This results in greater resistance to deformation and suboptimal leaflet dynamics during opening and closing in polymer leaflets [161]. Additionally, the greater force required to open the polymeric leaflets results in higher pressure gradients and energy loss across the valve, which are indicative of poor valve function [36,163].

Thornton et al. investigated the interplay of leaflet modulus and thickness using a finite element model of a polymeric bileaflet valve for the aortic position [164]. They modeled the leaflets using the isotropic linear elastic mechanical properties of polypropylene, varying the Young's modulus *E* between 3 and 8 MPa and also varying the thickness while holding *E* constant at 7 MPa. The results showed that leaflet stresses generally decreased with decreasing modulus and increasing thickness, although having too much flexibility ($E \leq 3$ MPa or thickness ≤ 0.1 mm) resulted in prolapse of the valve (for comparison, recall $E_{circ} \sim 15$ MPa and $E_{rad} \sim 2$ MPa, with thickness ranging from ~0.2 mm to ~2 mm in a normal human trileaflet aortic valve). However, increasing the stiffness would require a greater transvalvular pressure differential to achieve coaptation and reduce the efficiency of the valve – at $E = 7$ coaptation required pressure differentials of 7.7 kPa and 11 kPa for leaflets of thickness 0.3 mm and 0.9 mm, respectively. Since there are large regional variations in the stresses within the leaflet, the authors suggested that one approach to obtaining lower and more uniform stresses is to introduce local variations in leaflet thickness. This concept was indeed later implemented in polymeric valves developed by Daebritz et al.[42,43,197,213] and by Claiborne et al. [44,165].

Bernacca et al. performed an *in vitro* study comparing the effects of

varying the elastic modulus vs. the leaflet thickness on the hydrodynamic performance of a polyurethane trileaflet valve [36]. They tested valves with leaflet elastic moduli ranging from 5 to 63.6 MPa and leaflet thicknesses from 48 to 238 μm. The results showed that, except for the highest modulus value (63.6 MPa), the choice of modulus over the range of 5–32.5 MPa did not significantly affect the hydrodynamics of the valve in terms of regurgitation, leakage, energy loss, and mean pressure differential across the open valve. In accordance with beam theory, the leaflet thickness was a much greater determinant of hydrodynamic performance. The authors noted that low modulus materials are subjected to higher strains than high modulus materials at the same stress level and are therefore more susceptible to creep and ultimately failure. Since this work showed that relatively high modulus materials, up to ~32.5 MPa, did not adversely affect hydrodynamic function, they suggested that such materials might reasonably be used to improve the fatigue life of the leaflets.

3.1.2. Fatigue

The ISO 5840 standard for flexible leaflet prosthetic heart valves sets a minimum durability requirement of 200 million cycles during *in vitro* accelerated wear testing (AWT), which is equivalent to approximately 5 years of use. At an accelerated testing frequency of 10 Hz, reaching 200 million cycles takes nearly 8 months in real time. Before committing to such a lengthy evaluation, along with the time and money required to develop a valve prototype, one may first wish to know if potential valve materials possess acceptable fatigue properties. Additionally, these quantitative measurements, taken independently of valve design, can provide valuable insight into the mechanisms behind a valve's success or failure during AWT. In contrast to tensile properties, manufacturer data on the fatigue performance of commercial biomedical polymers is much less readily available. However, there are several interesting fatigue experiments documented in the academic literature.

McMillin developed a series of *in vitro* fatigue tests to help predict long-term *in vivo* performance of biomedical polymers intended for heart and ventricular assist devices [166]. Four sets of tests were used to rank five different materials. Three of the tests were uniaxial fatigue tests: a cut-growth fatigue test in an air at 37 °C where a 1 mm cut was introduced into the side of the specimen prior to testing, an uncut fatigue test in air at 37 °C, and an uncut fatigue test in blood at 37 °C. The fatigue tests were accelerated by gradually increasing the cyclic strains throughout the durations of the tests, which ranged from 20 days to 2 months. The fourth test was a tear strength test in air at 37 °C. The five materials tested were butyl rubber, Hexsyn, Pellethane®, Avcothane-51, and Biomer. Interestingly, a different polymer prevailed in each set of tests. In the cut-growth tests Hexsyn performed the best with an 18% strain at 50% probability of failure. In the uncut tests, Pellethane® had the best performance in air with 175% strain at 50% probability of failure, but Biomer was the best in blood with 260% strain at 50% probability of failure. All samples performed better in blood than in air. Avcothane had the highest tear strength by far at 37 kN/m. The author also conducted biaxial fatigue testing and found that the performance of the polymers ranked in the same order as in the uniaxial fatigue tests.

The overall variation in polymer performance encountered by McMillin indicates the importance of selecting the appropriate tests for different applications. For example, the choice of a stress-based vs. strain-based fatigue test can have a very significant effect on the results - a material with low elastic modulus will stretch easily and survive cycling to a fixed strain, but as mentioned previously, it may elongate further and fail under a cyclic stress. In the assist devices described by McMillin, the polymer would be used in a diaphragm that is displaced a prescribed distance, thus explaining the choice of strain-based fatigue tests for this study. However, in the context of flexible leaflet polymeric heart valves for implantation, it is our opinion that stress-based fatigue testing should be performed. As discussed earlier in Section 2.2.1 Mechanical environment, the maximum physiological stresses and strains in the native valve tissue occur at peak diastole, which is a load-driven condition governed by the transvalvular pressure differential. Thus, stress-based testing is more physiologically relevant as it can simulate the cyclic pressure loading sustained by the valve material. Since strain is not prescribed, it would also allow one to observe the deleterious effects of creep, as described in the following studies and in the next section on viscoelasticity.

Parfeev et al. performed a series of stress-based fatigue tests on several polymers to establish their wear limits, defined as the maximum stress above which the cyclic deformations would be unacceptable [87]. The tests were conducted in both uniaxial and biaxial tension for 10^7 cycles at a frequency between 22 and 25 Hz. In uniaxial fatigue testing, 52–336/4 (SKTV silicon rubber) performed the best with a wear limit of 1.80 MPa. In biaxial fatigue testing, a version of 52–336/4 reinforced with Lavsan (the Russian trade name for PET fibers, also known as Dacron in the U.S.) gauze reached 2.10 MPa, although FSM-2 (fluorosilicone rubber) was the best-performing neat polymer at 0.80 MPa. The wear limits were then compared to estimated *in vivo* stresses for the cusp in biaxial tension of 0.32–0.64 MPa for the aortic valve and 0.08–0.16 MPa for the pulmonary valve. Since the aortic valve stresses are very close to the wear limits of the polymers, the authors suggested that for aortic valve applications the polymers should be additionally reinforced. On the other hand, any of the silicone or fluorosilicone rubbers could be used for the pulmonary valve. The authors also conducted long-term fatigue testing at 26 Hz for 75 days to assess behavior at low stresses in the physiological range. In these tests, FSM-2 accumulated the most residual strain at 18%, while 52–336/4 and IR-68 had the least at 9% and 10% respectively.

Gallocher et al. used tensile tests, tension fatigue tests, and a bending fatigue test to compare the performance of poly(styrene-b-isobutylene-b-styrene) (SIBS) with and without polypropylene (PP) fiber reinforcement and to evaluate its potential for use in heart valves [167]. Note that the cross-linked version of SIBS, xSIBS, has since shown promising *in vitro* results for TAVR applications [45,168]. The tensile fatigue tests were performed according to the ASTM standard D 3479M − 96 for tension-tension fatigue testing of polymer matrix composite materials, cycling at 100 Hz between ± 10% of a selected mean load. The isotropic SIBS failed after 130 million cycles at a mean stress lower than 0.33 MPa, while adding three PP fibers as reinforcement only slightly increased the stress at failure. However, adding 12 PP fibers drastically improved the fatigue performance, and it did not fail after 350 million cycles at a mean stress of 2.5 MPa, higher than the 1.5 MPa achieved by polyurethane. The bending fatigue test was conducted by cycling the samples in buckling mode. Image analysis showed that the samples were bent to a curvature of 0.296 mm^{-1}, which is consistent with values reported for bioprosthetic heart valve leaflets during *in vitro* testing. After cycling, the specimens were subjected to tensile testing to determine if mechanical properties had been degraded due to fatigue. The results showed that isotropic SIBS stiffened due to the fatigue test, with Young's modulus increasing from 3.61 to 4.11 MPa. There was no statistically significant difference for SIBS reinforced with 12 PP fibers before and after the fatigue test, indicating that the reinforcement fibers had improved the bending fatigue properties compared to the neat polymer.

However, during an *in vivo* evaluation of a trileaflet valve constructed from PET-reinforced SIBS leaflets, Wang et al. observed that cracking of the leaflets had exposed the underlying reinforcing fibers, leading to tissue ingrowth with calcification and subsequent valve failure [169]. Tracing back through the literature, it was found that the cracking could be explained by the high susceptibility of SIBS to creep. El Fray et al. had previously evaluated the dynamic fatigue properties of SIBS using the hysteresis method, which is based on measuring the variation of hysteresis loops as a material fatigues [170,171]. In this method, the dynamic modulus is obtained from the slope of the mid-stress curve, which represents the average of the loading stress and unloading stress for each value of strain. The authors cyclically loaded

the specimens at 1–4 Hz while incrementally increasing the applied stress from 5% to 50% of the material's measured ultimate tensile strength (~10,000 cycles total) and monitoring the change in dynamic modulus. Results showed that the dynamic modulus of SIBS decreased exponentially between each increment of stress, with a steady overall decline from ~21 MPa to ~5 MPa at the point of material failure. Dynamic creep was obtained in a separate test, where dimensional changes were monitored while cycling at a single stress at 1 Hz. The appropriate stress level for dynamic creep testing was identified as the stress at which the drop in dynamic modulus exceeded 5%, which was calculated to be 1.25 MPa. When loaded, the SIBS showed an instantaneous elastic deformation of 20% strain and creeped to 30% after 100,000 cycles, at which point the test was terminated. This poor creep behavior was attributed to its amorphous structure. In contrast, materials with more favorable creep properties commonly have semi-crystalline hard segments or hydrogen bonding, while the improved creep resistance of xSIBS is due to the presence of crosslinks containing strong carbon-carbon bonds [172].

The Glasgow group performed a series of cyclic tests to identify any change in mechanical properties that might occur in polymers during implantation [173]. Two experimental variants of the commercial polyurethane Elast-Eon^{TM}, EV3.34 and EV3.35, were first formed into valves, then implanted in the mitral position of sheep, explanted after 9 months, and finally compared to unimplanted control material using the cyclic tests. Since stress cycling is more representative of *in vivo* conditions for a working valve, specimens were subjected to cyclic stress-based testing, cycling between zero extension and a maximum stress of 7 MPa for 500 cycles at a displacement rate of 50 mm/min. The energy loss per cycle, or hysteresis, was calculated as the area between the loading and unloading curves. Dynamic creep was quantified as residual strain, the additional strain remaining after each loading cycle. The EV3.34 variant showed similar inelastic energy loss behavior and residual strain in the explanted material compared to the control material. However, for EV3.35, after 500 cycles the explanted material showed both 30% less energy loss and 30% less residual strain than the control material. The authors suggested that changes in properties of explanted material could be due to plasticization effects from interactions with chemical species in the blood. Note that most of the studies described above were comparative in nature, with the intent of evaluating several polymers for potential heart valve use and then selecting the best one. The Glasgow fatigue experiment, however, is unique in that it was conducted on material that was not only implanted *in vivo*, but also subjected to the stresses and strains of a functioning valve. Thus, cost and time aside, this type of testing scheme would ultimately be more valuable since it provides a more accurate representation of a material's long-term clinical environment.

3.1.3. Viscoelasticity

As seen in the literature we have just reviewed, dynamic creep and hysteresis are important indicators of the fatigue life of polymers. Although creep tests are generally performed by applying a constant stress while measuring the deformation over time, the state of stress in a heart valve leaflet is certainly neither constant nor continuous as it cycles through systole and diastole. Yet, the rapid cycling of stresses in leaflets persists for many decades, and it has been shown that at physiological stress levels, these cycles can have a cumulative effect, resulting in elongation of the leaflets, or residual strain. This elongation perhaps stems from the hysteretic, viscoelastic behavior of the polymer. Under physiological conditions, the loading-unloading cycles are so rapid that a polymer leaflet may not recover fully before the next cycle, so that residual strain becomes cumulative and the leaflet essentially creeps. This elongation of the leaflet material is necessarily accompanied by localized thinning, which then leads to increased stresses and reduced fatigue life [174]. Additionally, a portion of the energy loss represented by hysteresis is associated with material damage and could also lead to increased strains. However, it is not clear in the literature if the observed residual strains are viscoelastic in nature and therefore recoverable, or the result of material damage and therefore plastic and irreversible, or a combination of both. Further study is warranted on this front to help predict the durability of prosthetic valve materials.

While there have been many studies on stress relaxation of native leaflet tissue, the stress relaxation response of polymers for prosthetic valves has seldom been considered. In one instance, however, Millon and Wan compared the stress relaxation response of polyvinyl alcohol-bacterial cellulose (PVA-BC) nanocomposites with porcine AV leaflets. Samples were held at constant strain for 100 s, and the relaxation data was fitted to a model for composite tissue:

$$\frac{\sigma(t)}{\sigma_o} = \frac{\sigma_R}{\sigma_o} + Ae^{-Bt} + Ce^{-Dt}, \tag{29}$$

where $\sigma(t)$ is the stress at time t, σ_o is the initial stress, σ_R is the final stress at $t = 100$ s, and A, B, C, and D are fitted parameters. The authors tested various concentrations of PVA and BC, as well as different processing conditions (number of freeze-thaw cycles). The relaxation responses of samples with 15% PVA and 0.5% BC after 4 cycles and after 1 cycle matched most closely with the leaflet response in the circumferential and radial directions, respectively [175].

3.1.4. Continuum mechanics-based constitutive modelling of polymers

The mechanical behavior of elastomeric polymers is typically described by a hyperelastic material model, which defines the constitutive behavior of non-linearly elastic materials using a strain energy density function, rather than using the overly simplified constitutive representation of a model based purely on linear elasticity. Mohammadi et al. used Mooney-Rivlin hyperelastic models to describe their anisotropic PVA-BC nanocomposite material (Table 4), while Claiborne et al. used the same type of model for SIBS and xSIBS [165,176]. The Mooney-Rivlin model for an incompressible material is defined by a strain energy density function in the form:

$$W = \sum_{i,j=0}^{\infty} a_{ij}(I_1 - 3)^i(I_2 - 3)^j, \quad \text{with } a_{00} = 0, \tag{30}$$

where W is the strain energy density, I_1 and I_2 are the first and second invariants of the right Cauchy-Green tensor respectively, and a_{ij}

Table 4
Parameters for hyperelastic Mooney-Rivlin models of anisotropic PVA-BC nanocomposite, showing the accuracy of various models using different numbers of coefficients [176]. Table reprinted with permission from SAGE Publications.

	a_{10}	a_{01}	a_{20}	a_{11}	a_{02}	Absolute error (%)
Longitudinal direction						
Two parameters	−0.144	−0.13	0	0	0	4.16
Three parameters	−0.446	0.499	0.0330	0	0	1.47
Five parameters	−3.906	4.095	27.240	−72.51	50.882	0.15
Circumferential direction						
Two parameters	1.365	−1.374	0	0	0	3.38
Three parameters	2.790	3.053	2.396	0	0	0.98
Five parameters	−26.778	28.001	184.86	−492.57	346.379	0.07

Table 5
Available data on mechanical properties of polymers for use in implantable prosthetic heart valves.

Year	Authors(s)	Material	Mechanical properties	References
1958	Roe et al., San Francisco	Silastic No. 50	Tensile strength = 5 MPa Elongation at break = 250% Hardness (Shore A) = 75	[200,202]
1966	Roe et al., San Francisco	General Electric No. SE-555	Tensile strength = 11 MPa Elongation at break = 850% Hardness (Shore A) = 45 Tear strength = 44 kN/m	[200,202]
1977	Reul & Ghista, HIA	Avcothane-51	E = 2.4 MPa (100% elongation at 37 °C) E = 4.4 MPa (300% elongation at 37 °C) Tear strength (Trouser) = 37 kN/m	[163,166]
1977	Imamura & Kaye, Mayo Clinic	ePTFE	Tensile strength = 413 MPa	[216]
1982	Wisman et al., Penn State	SPU	Tensile strength = 46 MPa Elongation at break = 750% Stress at 100% elongation = 5.9 MPa Hardness (Shore A) = 75	[204,232]
1987	Hilbert et al., NIH and FDA	Biomer	E = 2.5 MPa (100% elongation at 37 °C) E = 4.0 MPa (300% elongation at 37 °C) Tear strength (Trouser at 37 °C) = 9.6 kN/m Initial modulus E = 7.8 MPa Tensile strength = 44 MPa Tear strength = 70 kN/m	[166,233] [159]
1987	Herold et al., HIA	Cardiomat 610	Tensile strength = 28.0 MPa Elongation at break = 500% Hardness (Shore A) = 80	[214]
		Mitrathane M2007	Tensile strength = 39.2 MPa Elongation at break = 775% Hardness (Shore A) = 65	
		Pampul-3 Ameo	Tensile strength = 49.0 MPa Elongation at break = 605% Hardness (Shore A) = 75	
		PUR 1025/1	Tensile strength = 50.6 MPa Elongation at break = 649% Hardness (Shore A) = 87	
1995	Leat & Fisher, Leeds	Eurothane 2003	E = 6 MPa	[160,161,211]
		IT C34	E = 7–10 MPa	
1995	Wheatley et al., Glasgow	Estane® 58201	no data given	[35,37]
		Estane® 58315	E = 16.2 MPa	[36,38]
		Elast-Eon™ & variants	E = 5.0–63.6 MPa	
2001	Fisher et al., Leeds	Tecothane™ 80 A	E = 10 MPa	[39]
2009	Seifalian et al., UCL	POSS-PCU	At 37 °C Young's modulus = 15.9–26.2 MPa Tensile strength = 31.0–55.9 MPa Elongation at break = 762.7–852.4% Tear strength (Die C) = 50.9–63.4 N/mm	[46,47,185,188]
2009	Mohammadi et al., Ontario	PVA-BC	2, 3, and 5-parameter isotropic Mooney-Rivlin hyperelastic models based on tensile test data for anisotropic PVA-BC, one set of models for longitudinal direction and another set for circumferential direction	[175,176,189,191]
2010	Bluestein et al., Innovia & Stony Brook	SIBS-Dacron, xSIBS	2-parameter isotropic Mooney-Rivlin hyperelastic model based on tensile test data xSIBS tensile strength = 5 MPa	[44,165,167,169,215,228,234]
2014	Prawel et al., Colorado State	HA/LLDPE IPN	E = 76.49–99.71 MPa Yield strength = 8.23–9.74 MPa Elongation at break = 476–787% Bending stiffness = 12.93–21.72 nN·m^2	[235]
2015	Zhu et al., Singapore	ePTFE	E = 34.17 ± 0.54 MPa	[223]
2019	Guo et al., Shenyang	PEGDA/PET	Storage modulus: Parallel to fibers ~23.30 MPa Perp. to fibers ~9.68 MPa	[236]

represents the model coefficients. To define the model for a specific material, the authors obtained stress-strain data from uniaxial tensile tests and calibrated their material models using this data and commercial finite element analysis software. This software generally estimates model parameters by performing a curve fit, using non-linear regression analysis to minimize the error between the predicted response and the experimental data. The stress-strain ($\sigma - \varepsilon$) behavior is obtained, in general terms, by taking the derivative of the strain energy density function W with respect to an appropriate strain measure, ε:

$$\sigma = \frac{\partial W}{\partial \varepsilon}. \tag{31}$$

The resulting material model can then be used to perform a finite element analysis of the leaflets to predict mechanical stresses and valve

dynamics. Mohammadi et al. attempted curve fits in two principal directions using two, three, and five parameters and showed that the five-parameter Mooney-Rivlin model resulted in the least error compared to the experimental data (Table 4).

While Mohammadi et al. relied on two separate models to describe the two principal directions of anisotropic PVA-BC, Serrani et al. developed a single hyperelastic anisotropic constitutive model to describe the mechanical behavior of block co-polymers with oriented cylinders [177]. The strain energy density ψ was divided into isotropic and anisotropic contributions:

$$\psi(\mathbf{C}) = \psi_{iso}(\mathbf{C}) + \psi_{aniso}(\mathbf{C}), \tag{32}$$

where $\mathbf{C}$ is the right Cauchy-Green tensor. A Mooney-Rivlin model was used for the isotropic portion, while the anisotropic portion was given by

$$\psi_{aniso}(I_4) = k_4 \log^2 \sqrt{I_4}, \tag{33}$$

where k_4 is an experimentally-determined material parameter. The pseudo-invariant I_4 accounts for the cylinder orientation using unit vector $\mathbf{a}$:

$$I_4 = \mathbf{a}_0 \cdot \mathbf{C}\mathbf{a}_0 = \mathbf{a}^T \cdot \mathbf{a}, \tag{34}$$

where $\mathbf{a}_0$ defines the cylinders' direction in the undeformed configuration, and $\mathbf{a}$ defines the cylinders' direction in the deformed configuration. The authors used this model to perform a microstructural optimization based on simulated quasi-static loading of valve leaflets during diastole. Interestingly, the resulting optimum arrangement of cylinders closely matched the collagen fiber architecture of native leaflets, with a predominantly circumferential orientation. Although a proposed manufacturing technique based on injection molding technique (see Section 5.2 Injection/compression/cavity molding) could not fully achieve the optimum microstructural arrangement, this framework should nevertheless serve as a powerful tool once the appropriate manufacturing technology becomes available.

Overall, it would be helpful to see additional work performed examining the inclusion of rate-dependency of some polymers in the computational analyses and the resulting impact on quantities of interest related to valve function (e.g. EOA, mechanical energy losses due to hysteresis, etc.). Additionally, some investigation of the effects of creep would be highly informative since the geometry of the valve may change drastically over time, having a potentially large impact on valve performance. In the longer term, the mechanics of damage due to high cycle fatigue need to be studied further. These insights could be highly beneficial in incorporating new models of the stress-softening failure physics into temporal multi-scale simulations in order to predict the likely locations of failure in the valve structure. Simulations of this type could potentially help guide the design of valves with dramatically increased durability.

3.2. Composite biomaterials for heart valve prostheses

3.2.1. Macroscale composites

Considering the anisotropic, hierarchical, and fibrous nature of native heart valve tissue, the ideal material for a prosthetic valve might be a polymer-based composite that could replicate those properties. Many early attempts to fabricate such a composite material have focused on reinforcing the polymer leaflets with synthetic, macroscale fibers. This reinforcement is presumed to extend the life of the valve by redistributing the load in the leaflet and reducing the maximum stress experienced by the polymer, while also arresting the growth of any tears [178–180]. The McGoon and Roe-Moore prostheses both used PTFE fibers to reinforce elastomeric leaflets, and a human-implanted Roe-Moore valve reportedly functioned for 13 years [181]. Gerring et al. designed cusps made from Silastic silicone rubber with Terylene (the U.K. trade name for the PET fiber, also known as Dacron in the U.S.) polyester fabric reinforcement [182]. *In vivo* testing showed promising results, with some animals having survived for 30 months and counting at the time of reporting. Cacciola et al. showed that a winding machine could be used to arrange PE fibers within EPDM rubber leaflets, and that the fibers could be placed in regions of high stress or oriented in different directions to mimic collagen or elastin [178,180]. Finite element simulations of these reinforced valves suggested that the fibers carried up to 60% of the peak stresses and could also produce a more homogenous stress distribution [179]. As mentioned previously, Wang et al. developed a valve made from SIBS reinforced with a Dacron (PET) mesh, but dynamic creep during *in vivo* tests caused cracking of the SIBS and exposure of the underlying mesh [169]. Although a crosslinked version of SIBS – xSIBS – exhibited reduced creep, its strength was also significantly improved, and the use of reinforcement in xSIBS was deemed unnecessary [44,165,172]. Recently, Guo et al. developed a transcatheter aortic valve with leaflets comprised of poly(ethylene glycol) diacrylate (PEGDA) hydrogels reinforced with anisotropic polyethylene terephthalate/polyamide6 (PET-PA6) fabric. The PET-PA6 fabric contained highly directional fibers which were aligned with the circumferential direction of the prosthetic valve leaflets, and the resulting device showed good hemodynamic performance with a low systolic pressure gradient (8.67 mmHg), large orifice area (1.75 cm^2), and low regurgitation (3.41%).

3.2.2. Nanocomposites

While the long history of macroscale composites thus far has not produced any commercially-viable devices, the emerging class of nanocomposite biomaterials – materials reinforced with nanoscale filler – has shown the potential for more promising results. One distinct advantage of using nanofillers is the ability to improve not only the polymer's mechanical properties, but also its chemical properties, such as calcification potential and hemocompatibility [183]. Another advantage is that the valve manufacturing process is simplified – macroscale reinforcement needs to be carefully aligned and fixed during impregnation with the polymer matrix, while in a nanocomposite the nanoscale filler is already homogenously mixed into the polymer so that it can be cast monolithically. This greatly improves the reproducibility and scalability of the device. The small size of the filler also enables thinner leaflets, which is beneficial for TAVR applications where valves must be crimped to small diameters for percutaneous delivery.

The most promising nanocomposite is POSS-PCU, which was developed at University College London [46] and has since shown strong *in vivo* and *in vitro* results in TAVR applications [47,185]. It is a polyurethane consisting of a polycarbonate soft segment (PCU) and polyhedral oligomeric silsesquioxanes (POSS) covalently bonded to a hard segment containing aromatic compounds. In addition to increasing resistance to thrombosis and protecting the soft segment (responsible for the polymer's flexibility and elasticity) from degradation, the POSS also improved the polymer's elastic and viscoelastic properties [186,187]. For 100 μm thick samples, the tensile strength of POSS-PCU was shown to be much higher than PCU at both 25 °C (53.6 ± 3.4 vs. 33.8 ± 2.1 MPa) and 37 °C (55.9 ± 3.9 vs. 24.8 ± 3.4 MPa). Young's modulus was also greatly improved in POSS-PCU (25.9 ± 1.9 vs. 9.1 ± 0.9 MPa at 25 °C and 26.2 ± 2.0 vs. 8.4 ± 0.5 MPa at 37 °C). However, there was no significant increase in elongation at break and tear strength. Regarding viscoelastic behavior, the initial creep rate of POSS-PCU was higher compared to PCU, but the final extension of POSS-PCU at the end of the creep test was much lower. The nanocomposite was later incorporated into a prototype transcatheter valve where it contributed to markedly improved hydrodynamics compared to a commercial bioprosthetic valve, showing a larger effective orifice area, lower transvalvular pressure differential, and lower energy loss, although the design of the valve itself was likely also a factor [47,185,188].

Two other nanocomposites, one using bacterial cellulose (BC) as filler and the other using carbon nanotubes, are still in the early stages

of development but could yield very interesting results. With a focus on mechanical properties, Millon and Wan incorporated bacterial cellulose (BC) fibers into a polyvinyl alcohol (PVA) hydrogel [175,189,190]. They were able to achieve anisotropic tensile properties approximating native tissue by pouring PVA-BC into a mold, then thermally cycling the mold while it was held at 75% strain (Table 4) [190]. Work is currently underway to develop a prototype aortic valve from this material [176,191]. Recently, Rozeik et al. investigated the use of carbon nanotubes to reinforce ultra-thin (50 μm) leaflets, potentially for TAVR applications where valves must be crimped to small diameters [192]. The secant modulus of the neat polymer, Carbothane®, was increased by adding 0.5% w/w of nanotubes, but there was no significant additional increase in the secant modulus at a 1.0% concentration. It was also observed that increasing the concentration of carbon nanotubes led to decreased fatigue life, possibly due to increased brittleness. The authors noted that there were still many parameters to be studied, including functionalization of the nanotubes. They generated several surgical valve prototypes with nanotube-reinforced leaflets but did not publish any *in vitro* testing data.

4. Valve geometry

The geometry of the leaflets directly affects performance and durability. It has been shown that using a geometry with more physiological flow leads to improved hemodynamics and lesser risk of thrombosis [193], while as mentioned previously, abnormal flow patterns can result in increased forces on the arterial wall, leading to dilatation and possible aneurysm development [16,17]. Leaflet geometry also affects internal stresses, which appear to be related to calcification [35,44]. Therefore, it is generally accepted that it is desirable to match the geometry of a polymeric valve to the natural valve geometry as closely as possible.

This is no easy task. The natural heart valve is a complex structure, and its organic shape defies simple characterization. Many attempts have been made to describe heart valve leaflets geometrically as semilunar, sigmoid, parabolic, or using cylinders, cones, ellipses, and other mathematical descriptions [99,194,195]. Similar constructs have been used to define the geometries of leaflets for prosthetic devices (Table 6). Although none can match the complexity of the natural valve, they serve as a suitable starting point for developing prostheses and for understanding heart valve dynamics.

4.1. Bileaflet valves

Though the focus of this review is on trileaflet valves, it is worth including some information on polymeric bileaflet valves to provide additional context. The first polymeric device to be successfully implanted in a human was a bileaflet mitral valve developed by Braunwald in 1959 [196]. The valve shape was obtained from casts of animal and human valves. The leaflets were fabricated from Dacron fabric infused with PU in a mold, and the chordae were woven from Teflon.

The ADIAM polycarbonate urethane (PCU) bileaflet valve is one of the most successful flexible leaflet valves, having reached 1 billion (10^9) cycles during *in vitro* testing. The valve design includes a large anterior leaflet and smaller posterior leaflet which mimics the native mitral valve and encourages physiological flow patterns [197]. *In vivo* testing showed trivial regurgitation, no thrombus formation, and no signs of structural damage or calcification. Despite these successes, the valve never reached the clinical phase of study [181], highlighting the difficulty in obtaining regulatory approval for such high-risk devices.

4.2. Trileaflet valves

Trileaflet configurations are desirable as they are geometrically similar to the natural aortic and pulmonary valves, permitting central flow which helps to minimize blood trauma and risk of thrombosis [182,193,198]. *In vivo* studies comparing the trileaflet and bileaflet valves show lower pressure gradients (6 mmHg for trileaflet and 12 mmHg for bileaflet) and less regurgitation of trileaflet valves compared to bileaflet valves [198]. The reduction in blood trauma with the combination of superior stress distribution along the leaflets compared to bileaflet and quarto-leaflet valves should in theory increase durability [1].

Initial development of trileaflet valve geometry dates to 1958 when Roe and Moore proposed a design with cone-shaped leaflets, which were thought to be less resistant to opening during forward flow than dome-shaped cusps [200–202]. Later, Ghista and Reul studied the leaflet geometry analytically, based on the principal radii of curvature and subtending angles defined by Chong [203], to determine the optimal shapes for achieving smooth washout, minimum leaflet stress, and good coaptation [163]. The optimized design enabled tangential flow and mutual support of the leaflets along the whole closure rim, resulting in durability of more than 350 million cycles *in vitro*.

Wisman et al. designed a segmented polyurethane (SPU) trileaflet valve using 3 hemicylindrical leaflets and a flexible support framework. *In vitro* testing showed good hydraulic function and efficiency. *In vivo* performance varied between growing calf and adult animals, with dystrophic calcification and thrombosis when implanted in growing calves, but longer survival and less calcification when implanted in mature animals [204].

In developing a valve for a ventricular assist device (VAD), Fisher et al. at the University of Leeds analyzed previous leaflet geometries and showed that an increased radius of curvature at the base of the leaflets would improve opening characteristics. The new leaflet geometry was described in terms of a variable curvature. A weighting term was used to vary the leaflet resistance to opening by controlling the rate of increase in curvature from the leaflet free edge to the base towards the base of the valve, reducing the opening pressures by over 40%. Leaflet thickness was also varied, with a value of 180 μm leading to a pressure differential of less than 1 mmHg [161].

The Glasgow group described their leaflet geometry using conic sections - elliptical radially and hyperbolic circumferentially (Fig. 7a) [37]. The geometry was meant to approximate the leaflet shape of a bovine pericardial bioprosthetic valve. Hyperbolic parameters were adjusted to enable efficient coaptation with minimal stretching of the leaflets. The authors also discussed the effects of valve frame design and leaflet attachment location. During accelerated fatigue testing, the valve performed for the equivalent of 10 years without failure and showed good hydrodynamic performance. A later design from the same group used a conical geometry for the leaflet area adjacent to the frame to permit buckling and facilitate opening and closing, while the upper leaflet area was spherical to provide a stable closed position and ensure good coaptation [39]. *In vitro* durability testing reached 360 million cycles and showed greater effective orifice area (EOA) and reduced regurgitation and energy loss compared with mechanical and porcine bioprosthetic valves.

Based on the hyperbolic geometries from Leeds and Glasgow, Jiang et al. defined leaflet shapes using a hyperboloid of revolution. Parameters were calculated to meet certain criteria such as coaptation at the commissures, a small central opening, and only moderate curvature of the free edge when in the closed position. This was compared to a second design defined by an arc subtending two straight lines, which gave better control of the central opening and leaflet curvature [205]. However, it was later noted that these designs suffered from gaps between adjacent leaflets and a large central orifice in the closed position. Additionally, the designs did not account for the properties of the valve material [176].

The aforementioned valve designs have relied in large part on experimental methods to evaluate their performance. Additionally, the designs are typically based on relatively simple mathematical equations that assist in describing the geometry. As previously mentioned, both

Table 6
Polymeric heart valve geometries – descriptions and testing results.

Year	Author(s)	Geometry/description	Results	References
Bileaflet valves				
1959	Braunwald & Morrow, Boston	Shape based on plaster casts of human and animal mitral valves	*In vivo* – Human implant (mitral), 60 h and 4 months (1st human PU valve implant)	[196,237]
2003	Iwasaki et al., Waseda	Valves for pulsatile pumps Type A – Circular flexible disc attached to a frame along the diameter, producing two flaps. Type B – 12-spoke structure cast from polyurethane with a 150 μm disc on top	*In vitro* – Type A: 8.8×10^5 cycles Type B – 3.7×10^6 cycles	[238]
2006	Daebritz et al., Munich	Kidney shaped stent with two asymmetrical struts supporting a large anterior and smaller posterior leaflet	*In vitro* – 1 billion (10^9) cycles	[42,197,213]
Trileaflet valves				
1958, 1966	Roe et al., San Francisco	Conical cusps, shown to be less resistant to opening than dome-shaped cusps	*In vitro* - 786 million cycles *In vivo* – 18 clinical human implants, 4 post-operative survivors from 79 to 100 months	[200–202,239]
1977	Reul & Ghista, HIA	Analytical determination of shapes for smooth washout, minimum leaflet stress and fatigue lifetime of 20 years	*In vitro* – 350 + million cycles	[163,193]
1982	Wisman et al., Penn State	3 hemicylindrical leaflets of 10 mm diameter each angled with respect to the flow axis, with flexible support framework	*In vitro* – good hydraulic function and efficiency *In vivo* – calcification and thrombosis in growing calf, longer survival and less calcification in mature animals	[204]
1994	Fisher et al., Leeds	Variable radius of curvature where the radius of curvature of leaflet increases away from the center of the valve towards the base of the leaflet	*In vitro* – 180 μm leaflets produced a pressure drop of less than 1 mmHg	[161]
1996	Wheatley et al., Glasgow	Leaflet geometry is elliptical radially and continuous hyperbolae circumferentially	*In vitro* – 800 million cycles *In vivo* – 6-month survival in sheep	[37,38,240]
2004	Jiang et al., Ontario	Hyperboloids of revolution: control of central opening and leaflet curvature by varying parameters such as coaptation at commissures and curvature of free edge	*In vitro* – successful demonstration of opening/closing of valve using a cyclic flow tester	[205]
2009	Mohammadi et al., Ontario	Bezier curves/surfaces	FEA showed acceptable opening/closing characteristics and good stress distribution	[176]
2009	Bluestein et al., Stony Brook	Hemispherical geometry, originating from Thubrikar's characterization, leaflet thickness varying along the radial direction	FEA and fluid dynamic simulations showed superior stress distribution and improved hemodynamics	[44,165]
2010	Burriesci et al., UCL	Ruled surface between intersection of the stent cylinder with a plane and an arc joining the commissures, lying on a plane normal to the valve axis.	*In vitro* – 10 cycles testing – less energy loss, blood trauma and clot formation	[47,185,188,199]
2015	Gharaie & Morsi, Victoria	Sweeping a circumferential curve along a radial curve	FSI model showed improved characteristics compared to other polymeric valves, with EOA of 3.22 cm^2 and pressure drop of 3.52 mmHg	[209]

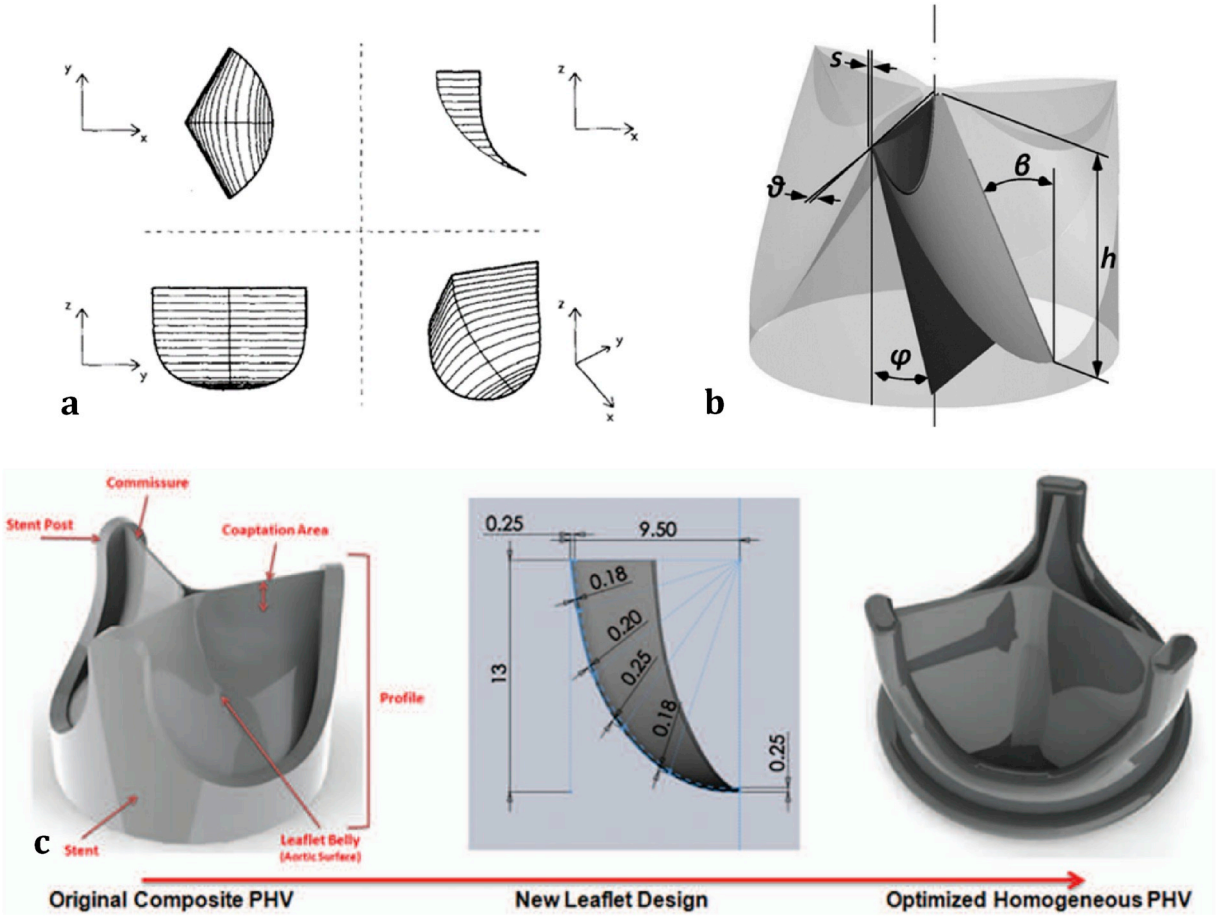

Fig. 7. (a) Ellipto-hyperbolic leaflet geometry from the Glasgow group. In the closed position, the geometry is elliptical in the radial direction (x-z plane) and hyperbolic in the circumferential direction (x–y) plane [37]. (b) Design schematic from the UCL group showing the various geometric parameters to be optimized using structural FEA: leaflet height h, leaflet angle β, commissural distance s, reflection angle to valve axis φ, and reflection angle to valve radius ϑ [199]. (c) Schematic of design process by Claiborne et al. showing original prosthetic heart valve (PHV) made with SIBS-Dacron composite leaflets, computational optimization of leaflet thickness distribution, and final optimized valve design for homogeneous xSIBS leaflets [44]. Figures reprinted with permissions from Elsevier, Taylor & Francis, and Wolters Kluwer Health.

the tasks of designing and subsequent evaluation/analysis are considerably complex. In recent years great strides have been taken in improving the quality of computational methods for predicting the performance of particular valve designs. Numerical simulations including structural finite element analysis (FEA), computational fluid dynamics (CFD), and, more recently, incorporation of the fluid-structure interaction (FSI) physics have proven to be important tools for optimizing valve designs, resulting in the improvement of a variety of valve performance metrics. Fluid-structure interaction models incorporate the solid structural physics, the physics of fluid flow, and the highly nonlinear interaction between the two. This is in contrast to both computational fluid dynamics simulations, in which the solid structure is usually assumed to be fixed, and typical structural finite element simulations where the fluid effect is typically reduced to an assumed pressure distribution. In the remainder of the section we will mention first a few studies utilizing FEA and CFD tools independently to improve the valve design, followed by a selection of work incorporating the FSI capability.

In order to improve on the designs of Jiang et al., Mohammadi et al. utilized Bezier surfaces, which could be easily altered by manipulating control points in computer-aided design (CAD) software [176]. Combined with structural FEA, this enabled the authors to quickly analyze various geometries using the relevant material properties and select an optimum design that addressed the deficiencies of the previous hyperboloid designs. Although fluid flow was not incorporated, the structural simulations showed acceptable opening and closing dynamics and stress distributions within the physiologic range for native aortic valves.

In a similar optimization study, Burriesci et al. designed a low-profile semi-stented aortic valve. The geometry was defined as a ruled surface between the intersection of the stent cylinder with a plane and an arc joining the commissures, lying on a plane normal to the valve axis [199]. Structural FEA software was used to optimize certain geometric features of the valve (Fig. 7b) in order to maximize the geometric orifice area (GOA) and decrease stress amplitudes in the leaflets. Since no fluid flow was simulated, the typical effective orifice area (EOA) metric was replaced with the largest geometric orifice opening area during a cardiac cycle (termed the GOA). Subsequent *in vitro* testing confirmed a larger EOA compared to a reference valve using the ellipto-hyperbolic geometry from the Glasgow group [37], along with reductions in regurgitation and the transvalvular pressure differential. Echoing studies that we have previously discussed, it was determined that the leaflet thickness significantly affected the hydrodynamic function. Valves with the thinnest leaflets exhibited the largest EOA and the lowest pressure differential, regurgitation, and energy loss [188]. This design was later incorporated into the investigational TRISKELE transcatheter aortic valve [47,185].

Another interesting work based on structural FEA, without incorporation of fluid flow physics, is a parametric study by Li and Sun in which 500 different geometric realizations were analyzed in the closed

position in order to determine the effect of certain geometric parameters on the peak leaflet stress [206]. Subsequent numerical optimization of these geometric parameters showed a potential 5% reduction in the peak stress with respect to the original leaflet design. A design study by Claiborne et al. found that stress distribution within the leaflets could be optimized by varying the thickness across the leaflet (Fig. 7c) [44]. The leaflet shape was hemispherical, and coaptation was maximized using a flat leaflet profile. The final optimized design had a leaflet with varying thickness from 180 to 250 μm, producing an EOA of 1.44 cm^2. Structural FEA simulating static loading in the closed position demonstrated superior stress distribution compared to other polymeric valves. Separate CFD simulations of blood flow through both a fixed open and closed geometry of the valve showed improved hemodynamics and reduced thrombogenicity.

Trileaflet heart valve designs based on simulations incorporating the highly nonlinear fluid structure interaction physics are becoming increasingly prevalent. Compared with results from FEA simulations excluding the fluid flow physics, both Piatti et al. [207] and Hsu et al. [208] remark on the importance of performing the FSI analyses in order to obtain accurate predictions of the valve opening response. Gharaie and Morsi used a FSI model to optimize and test the performance of their design, showing improved hemodynamic characteristics and structural integrity (increased EOA, reduced regurgitation, reduced transvalvular pressure differential, lower leaflet stresses) compared to the ellipto-hyperbolic geometry from the Glasgow group [37,209]. The leaflet surface was obtained by sweeping a circumferential curve along a radial curve. The circumferential curve was optimized to obtain a parallel free edge for good coaptation and to create a small central orifice area to minimize regurgitation. In selecting the curvature in the radial direction, care was taken to avoid a curvature that would be too high and thus interfere with the flow vortex in the sinuses of Valsalva, while still permitting sufficient leaflet displacement.

Additionally, both Hsu et al. [208] and Xu et al. [210] constructed parameterized leaflet geometries using NURBS surfaces and splines, which provide a very useful framework for design optimization based on movement of the associated control points. Xu et al. provide a very interesting and advanced framework for providing optimized replacement valves on a patient-specific basis. Each design's performance is evaluated using a fully coupled FSI simulation using models derived from the patient's medical imaging. Though highly computationally demanding (it can take 1–2 days to simulate one cardiac cycle with FSI), it is a reasonable expectation that these predictive methods, when coupled with techniques from numerical optimization, will yield very efficient and durable valve designs. As remarked by Xu et al., combining these computational methods with the emerging field of 3D bioprinting could provide a viable path for optimal patient-specific valve replacements.

5. Valve manufacturing methods

Polymer valve manufacturing methods can be grouped into three general categories: dip molding, film fabrication, and injection/compression/cavity molding (Table 7). While each method has distinct advantages and disadvantages, the choice of method is often dictated by the chemical properties of the selected valve material. Polymers that are readily soluble in organic solvents, such as polyurethanes, are amenable to dip molding or film fabrication via solvent casting. Materials that are more chemically stable, such as silicone, must be heated to a melt and then shaped into leaflets via compression molding or cavity molding. The fabrication process can have a significant impact on valve performance and durability, affecting critical areas such as the leaflet-frame interface.

5.1. Dip molding

Dip molding, also referred to as dip coating or dip casting, generally produces valves with good durability. Several valve prototypes produced by dip-molding have reached several hundred million cycles *in vitro* and shown promising *in vivo* results. The dip molding process is simple in concept. First, a mold or mandrel with the desired leaflet geometry (Fig. 8a) is dipped into a polymer-solvent solution, which is typically heated to a temperature between 60 and 80 °C. Upon removal, a layer of solution is adhered to the mold. The mold is then heated to remove the solvent by evaporation (drying), leaving a thin film of the polymer. These steps can be repeated until the desired polymer thickness is achieved. The valve frame or stent can be dipped together with the mold in the first step or in subsequent dipping steps. This enables a smooth transition and durable bond between the leaflets and the frame, even if the frame is constructed from a dissimilar material such as nitinol [47,185] or PEEK [211]. In practice, achieving repeatability with dip molding requires precise control of many factors, including polymer concentration and solution viscosity, mold shape and surface roughness, mold orientation during dipping and drying, dipping speed, and atmospheric conditions. Due to the fluid state of the polymer, manipulation of any of these variables easily affects leaflet thickness and uniformity and could potentially introduce defects such as bubbles. Mackay et al. and Rahmani et al. showed that even in a well-controlled process, thickness can vary in the range of ~50% within the same leaflet [37,188]. Some research groups have introduced robotic mechanisms to improve control of the dipping step and also to tumble the mold during drying to improve uniformity of polymer distribution [47,212]. However, Daebritz et al. intentionally varied the leaflet thickness distribution to reduce stress at the commissures. Rather than dipping a mold into polymer solution, a dropping technique was used to deposit PCU onto the mold in a controlled manner, enabling variation of thickness across the leaflet from 80 to 200 μm [42,43,197,213]. The PCU droplets coated the whole valve, including the stent which was made from a harder PCU, thus providing a strong bond between the stent and the leaflets.

5.2. Injection/compression/cavity molding

Compared to dip molding, a significant advantage of injection, compression, and cavity molding techniques is that the leaflet thickness can be defined entirely by the mold, greatly improving reproducibility. Injection molding involves the melting of a polymer and then the application of pressure to force the polymer melt through an inlet and into a mold. The flow of the polymer melt normally imparts some directionality to the polymer chains [217]. Stasiak et al. used this behavior to achieve anisotropy in leaflets made from poly(styrene-block-isoprene-block-styrene) containing 30 wt% styrene (SIS30), a block copolymer with cylindrical morphology [218]. The polymer was heated to 160 °C and injected at a pressure of 8.51 MPa through a 1 mm diameter inlet pipe into the top of a valve-shaped mold. SAXS revealed a bi-directional orientation of the copolymer that was governed by a balance between shear and extensional flow during the injection molding process. Shearing occurred in the radial direction at the interfaces between the polymer and the mold, resulting in radially oriented cylinders at the leaflet surfaces, while elongation forces due to extensional flow produced circumferentially oriented cylinders at the center of the leaflet thickness. The ratio of radial to circumferential orientation could be controlled by varying the flow rate and sample thickness. As discussed earlier (see Section 3.1.4 Continuum mechanics-based constitutive modelling), this technique was limited in that it could not fully reproduce a computationally optimized arrangement, where the cylinders were predominantly oriented in the circumferential direction. It would be interesting to see if further improvements can be made in order to realize this optimum microstructure. Injection molding has also been proposed as a technique to make valves for VADs [219–221]. However, one major disadvantage of this technique is that polymer flow and inhomogeneous cooling typically lead to residual stresses that can impact valve dynamics and reduce valve durability [217].

Table 7
Manufacturing processes for flexible leaflet polymeric heart valves.

Year	Author(s)	Material and process	Results	References
Dip molding, dip coating, dip casting				
1959	Kolff et al., Cleveland	PU dissolved in tetrahydrofuran (THF) and poured into an open mold	*In vivo* – dog implant (mitral, aortic and tricuspid), high mortality due to clotting on surface	[241]
1959	Braunwald & Morrow, Boston	Dacron fabric placed between two-piece male/female mold and filled with liquid PU	*In vivo* – human implant (mitral), 60 h and 4 months	[196,237]
1977	Reul & Ghista, HIA	Leaflet molds dipped into Avcothane-51 PU solution	*In vitro* – 350 + million cycles *in vitro* (aortic)	[163]
1980	Russell et al., Boston	Valved conduit – conduit formed first by dipping in Avcothane-51 solution, then leaflet mold inserted into conduit and filled with solution	*In vitro* – 58 + million cycles *In vivo* – calf implant 135 days (aortic)	[231]
1982	Wisman et al., Penn State	PU dissolved in N–N-dimethyl acetamide (DMAc), leaflet mold dipped in solution	*In vivo* – calf, sheep and goat implant (mitral and tricuspid), survival up to 960 days	[204]
1987	Herold et al., HIA	PU dissolved in THF or DMAc, leaflet molds made by electro-erosion and dipped in PU solution	*In vitro* – 93 million cycles *In vivo* – calf implant up to 267 days (trileaflet prosthetic in mitral position)	[214]
1991	Jansen et al., HIA	Leaflet molds and valve stent dipped together into PU solution, after dipping the mold is tumbled in space for even thickness distribution	*In vitro* – 648 million cycles *In vivo* – 5 of 7 calves > 150 days, outperformed bioprosthetic (trileaflet prosthetic in mitral position)	[212,242]
1994	Leat & Fisher, Leeds	PU dissolved in dimethyl formamide (DMF), leaflet mold dipped in solution	*In vitro* – 160 + million cycles	[211]
1995	Wheatley et al., Glasgow	Leaflet molds made by electrical discharge machining (EDM) and dipped in Elast-Eon™ PU-silicone copolymer solution	*In vitro* – 800 million cycles *In vivo* – 6-month survival in sheep (trileaflet prosthetic in mitral position)	[35–38,173,240,243,244]
2001	Fisher et al., Leeds	Leaflet mold dipped in Tecothane™ 80 A PU solution	*In vitro* – 362 million cycles (trileaflet)	[39,245]
2003	Daebritz et al., Munich	Droplets of dissolved ADIAMat PCU deposited onto leaflet mold, thickness intentionally varied to reduce stress at commissures	*In vitro* – 600/1000 million cycles (aortic/mitral) *In vivo* – good survival to 5 months in calves, outperformed bioprosthetic	[42,43,197,213]
2005	Yoganathan et al., Georgia Tech	Leaflet mold dipped in Elast-Eon™ solution	*In vitro* – low flow regions corresponding with thrombus formation *in vivo*. Thicker leaflets correspond to greater leakage.	[246,247]
2006	Metzner et al., Kiel & Aachen	Dip-coating in PU to form valved stent for percutaneous, catheter-based delivery	*In vivo* – good survival in sheep (8 of 9, pulmonary) to 4 weeks	[248,249]
2009	Seifalian et al., UCL	POSS-PCU dissolved in DMAc, leaflet molds dipped in solution, design later adapted for percutaneous delivery, dipping process automated to improve reproducibility	*In vitro* – lower leakage vs. commercial TAVI bioprosthetics	[46,47,185,188]
2016	Zilla et al., SAT	Dip molding or spray molding of dissolved SAT polymer onto leaflet mold	*In vitro* – 600 million cycles *In vivo* – 8 weeks in sheep	[250,251]
Injection/compression/cavity molding				
1958, 1966	Roe et al., San Francisco	Silastic silicone, heated to 177 °C in a compression molding die for 1 h, removed from die and heat cured at 204 °C for 4 h In a later iteration, SE-555 silicone heated to 132 °F in the molding die at 100 MPa	*In vitro* - 786 million cycles *In vivo* – 18 clinical human implants, 4 post-operative survivors from 79 to 100 months (aortic)	[200–202,239]
1965	Braunwald & Morrow, Boston	Plain PTFE fabric and PTFE fabric coated with PTFE dispersion	*In vivo* – 23 clinical human implants, 15 died or required reoperation due to severe regurgitation (aortic)	[252]
1973	Mohri, U. of Washington	Silastic silicone injected into a compression molding die, pressurized to 41 MPa for 5 min, air and overflow evacuated, then pressure increased to 62 MPa for 1 min, vulcanization in oven at 148.9 °C for 50 min, then valve removed from die and cured at 148.9 °C for 2.5 h	*In vitro* – durability equivalent to 18–25.5 years	[253]
1980	Chetta & Lloyd, Notre Dame	Two-piece male/female mold filled with RTV-615, a room temperature vulcanizing silicone rubber	*In vitro* – functioned for 280 million cycles until work hardening of silicone rubber prevented leaflet opening	[222]
1989	Kolff & Yu, Utah	Silastic silicone, stent and leaflet molded at same time on a cylindrical mold	N/A	[254]
2004	Jiang et al., Ontario	Polyvinyl alcohol cryogel (PVA-C), cavity mold injected with hot PVA-water solution, then sealed, clamped and immersed in water bath with controlled freeze/thaw cycles.	N/A	[205]
2009	Mohammadi et al., Ontario	Polyvinyl alcohol-bacterial cellulose (PVA-BC) composite, cavity molding process similar to Jiang et al.	N/A	[176,190,191]
2013	Bluestein et al., Stony Brook	Raw xSIBS compressed under vacuum in a mold at 260 °C with 1 ton of force for 30 min. Mold fabricated by EDM.	*In vitro* – 400 + million cycles, hydrodynamics comparable to bioprostheses	[45,165,215]
2014	Stasiak et al., Cambridge, UK	Injection molding of SIS30 block copolymer to introduce bidirectional, anisotropic cylinder orientation	*In vitro* – 3 + million cycles	[218]
2015	De Gaetano et al., Cambridge, UK	Compression molding of styrene block copolymers to introduce anisotropy and microstructural orientation	*In vitro* – EOA and regurgitation comparable to mechanical and bioprosthetic valves	[255,256]
Film fabrication				
1960	McGoon, Mayo Clinic	PTFE cloth impregnated with PU	*In vivo* – 98 implantations	[181]

(*continued on next page*)

Table 7 (*continued*)

Year	Author(s)	Material and process	Results	References
1974	Gerring et al., Oxford	Terylene (PET) fabric coated with Silastic by press curing, then cut and bonded to sewing ring Also, films of Biomer (PU) cast from solution onto glass plate, then cut and bonded to sewing ring	*In vivo* – survival up to 30+/21 + months for Silastic/Biomer implants in calves (pulmonary)	[182]
1977	Imamura et al., Mayo Clinic	Gore-Tex® (ePTFE) assembled in multilayer laminate to reduce porosity and improve strength, sutured to support frame with additional ePTFE layers for reinforcement	*In vivo* – survivability 12/28 dogs up to 15 months (tricuspid)	[216,257]
1989	Kolff & Yu, Utah	Pellethane® polyurethane, vacuum formed or solution cast	*In vivo* – 5/5 sheep up to 15 months	[254]
1990	Nistal et al., Spain	Gore-Tex® ePTFE (no report of fabrication process)	*In vivo* – survival up to 42 weeks in sheep (tricuspid)	[224]
1995	Leat & Fisher, Leeds	Solvent casting of flat PU films, cut and bonded to valve frame, then thermally formed into alpharabola geometry on a mold	*In vitro* – 100 million cycles	[161,211]
2005	Koh et al., Osaka	Gore-Tex® (ePTFE) membrane cut and sutured to either bovine pericardium or Gore-Tex® vascular grafts. Radiopaque markers sutured to center of leaflet free edges to imitate the nodulus of Arantius	*In vivo* – 47 human implants (pulmonary), no significant obstruction after 1 month–7 years	[225]
2009	Ando & Takahashi, Tokyo	Gore-Tex® (ePTFE) membrane manually cut, folded, and sutured to create three pockets that comprise the valve, then sutured within a Dacron conduit to make a valved conduit	*In vivo* – 139 human implants (pulmonary), good survivability and competence at 10 years	[40]
2010	Wang et al., Innovia	SIBS dissolved in toluene and cast around a Dacron mesh to produce a flat sheet with uniform thickness, leaflet cut and sewn onto a molded SIBS stent using polyester sutures	*In vivo* – poor survivability (1/4) of sheep aortic implant, valve failure due to material damage and calcification	[165,169,258]
2014	Prawel et al., Colorado State	Leaflets formed with a cylindrical sheet of hyaluronan-linear low-density polyethylene interpenetrating networks (HA/LLDPE IPN)	*In vitro* - EOA higher than bioprostheses, comparable regurgitation	[235]
2014	Zhang et al., Shanghai	Films of Gore-Tex® (ePTFE) dip-coated in phosphorylcholine, then trimmed and sutured to stent	*In vivo* – good survivability in sheep (9 of 9) to 4 weeks (pulmonary)	[41]
2017	Basir et al., Netherlands	Valve made from textile of woven ultra-high-molecular-weight polyethylene (UHMWPE) fibers and affixed to stent	*In vivo* – 17/18 sheep survived to 6 months (pulmonary)	[259]
2019	Guo et al., Shenyang	Anisotropic PET fabric impregnated with PEGDA hydrogel, trimmed and sutured to nitinol stent	*In vitro* – Large EOA and low regurgitation	[236]

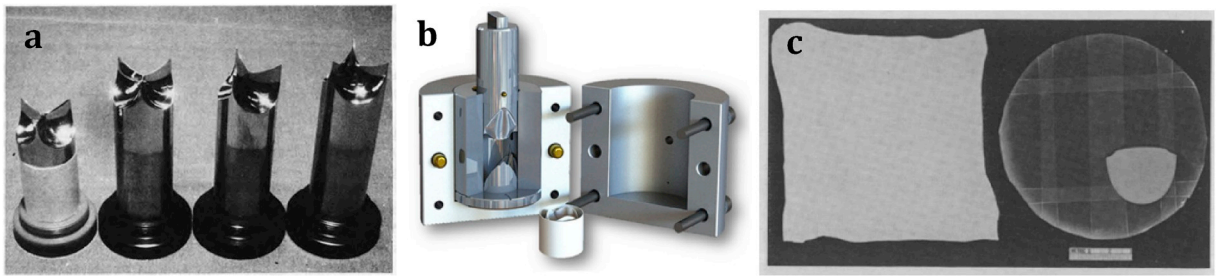

Fig. 8. (a) Polished stainless steel molds for dip-molding [214]. (b) Illustration of compression mold used for manufacture of xSIBS valve [215]. (c) ePTFE films used for fabrication of prosthetic valve leaflets. (Left) Single layer of ePTFE film. (Right) Laminated 8-layer ePTFE film with 15-layer regions for reinforcement. A single layer is porous and white in appearance, while multilayer laminates are nonporous and transparent. Leaflet shapes were cut according to the scallop-shaped template [216]. Figures reprinted with permissions from Elsevier and Springer Nature.

Compression molding involves preheating of the polymer and then placing it in an open mold. The mold is then closed, and a pressure is applied to force the material into all the parts of the molding box. Heat and pressure are maintained in the molding box until the material has cured. Claiborne et al. used to this method to fabricate valves from xSIBS, heating the mold up to 260 °C and compressing with 1 ton of force (Fig. 8b) [165,215]. This process can be simplified by using materials that do not require high heat, but instead can cure at room temperature [222].

Jiang et al. used a similar process, termed cavity molding as it does not require pressure, to fabricate a valve from PVA-C hydrogel [205]. After filling the mold with hot PVA solution, it was sealed, placed in a water bath, and then subjected to cycles of alternating freezing at −20 °C and thawing at +20 °C to form the device. It was noted that dipping and film fabrication methods were not suitable because solidification and mechanical properties of PVA-C are determined by the freeze/thaw cycles. The leaflets, stent, and sewing ring were formed from the same material in a single step, ensuring these components were well-integrated.

5.3. Film fabrication

Film fabrication is the technique of manually manipulating flat polymer films into the desired valve geometry. Rather than fabricating the film in the leaflet shape directly, a flat film is first obtained by any of a variety of techniques such as solution casting, compression molding, or extrusion. The film is then trimmed to leaflet dimensions and attached to the valve frame by solvent bonding or suturing. The leaflets can be set into a specific geometry by thermal forming [211]. Expanded polytetrafluoroethylene (ePTFE) is an example of a material that cannot be easily processed by solvents or conventional molding since it retains the chemical inertness of PTFE and has a microporous structure that can be easily degraded by heat treatment [223]. Therefore, attempts to incorporate ePTFE into heart valves typically require the acquisition of pre-processed films from commercial sources. The films are then manipulated into valve configurations by trimming and suturing (Fig. 8c) [40,41,216,224,225].

One disadvantage of this method is the resulting weakness of the critical leaflet-frame interface. Sutures, for example, introduce stress

concentrations that can severely limit valve durability. It was mentioned previously that in dipping techniques, the leaflets are formed and bonded to the frame in a single step, providing a seamless transition. Leat and Fisher performed an interesting comparison of film fabrication and dip molding [211]. They showed that PU valves manufactured by film fabrication and solvent bonded to a PEEK frame tended to suffer subsequent debonding, resulting in low durability and failure prior to 100 million cycles. However, valves manufactured by dip molding had no such problems and had reached 160 million cycles by the time of publication.

In general, dip molding and injection, compression, and cavity molding appear to be the most promising techniques for the fabrication of polymeric valves. Injection, compression, and cavity molding offer the most reproducibility for achieving certain leaflet thicknesses, while dip molding has thus far produced the most durable valves. Film fabrication techniques are conceptually the simplest, but they typically result in a weak leaflet-frame interface, limiting durability. In terms of resources, injection, compression, and cavity molding require the most specialized equipment, as the raw polymer must be brought to high temperatures and/or pressures. A basic dip molding setup requires little more than a valve-shaped mold and a hot plate to heat and dissolve the polymer, but any attempt to improve the reproducibility of leaflet thicknesses would require specialized robotic equipment. Film fabrication requires the least investment in equipment, but it can also be the most labor intensive if one is to perform manual suturing. Thus, both film fabrication and dip molding are appropriate for prototyping, while dip molding and injection, compression, and cavity molding could be considered for scalable production.

6. Summary and future directions

The native heart valve is an intricate mechanism specially suited to operate for billions of cycles in a dynamic loading environment in the most critical organ of the body. A thorough understanding of native heart valve leaflet tissue properties can inform materials design and selection for prosthetic valves. To facilitate the translation from native valve properties to prosthetics design, this review has discussed the functional microstructure and complex mechanical behavior of native leaflets as revealed through uniaxial, biaxial, flexural, fatigue and viscoelastic testing. Polymers also exhibit complex mechanical behavior characterized by hyperelasticity, viscoelasticity and plasticity. Yet, early development of prosthetic valves took a very simplistic view of polymer mechanical properties, relying on linear elastic models of the material. Since the microstructural behavior of the native valve is so crucial to its success, so too must we account for the same level of complexity in synthetic valve materials. Recent development of anisotropic nanocomposites and block copolymers, anisotropic hyperelastic material models, and computational tools for microstructure optimization show a growing recognition for the need to bridge this gap. It is expected that continued advancements in materials design, along with increasingly accurate mathematical models describing and predicting the underlying physics, will contribute to significant improvements in valve performance.

The effect of polymer mechanical properties on valve performance and durability is inextricably linked to the geometry of the valve leaflets. While the geometry of a native valve can be easily cast and replicated, this may not necessarily result in optimal performance for a polymeric valve. As an extreme example, stiff pyrolytic carbon is well-suited for valves with tilting disk geometries, but the use of pyrolytic carbon leaflets in a configuration without hinges would result in a non-functioning valve that cannot open or close. Leaflet design has long been guided largely by intuition, but in theory one could optimize the geometry for any given material. While some studies have attempted relatively simple problems, such as optimizing leaflet thickness distribution under static diastolic loading, recent advances in computer power have enabled the development of complex FSI models where it is possible to consider all components of the valve under dynamic physiological conditions. The improved accuracy of these simulations, coupled with techniques in numerical design optimization, could lead to further, unexpected insights regarding valve design.

The fabrication process for polymeric valves is largely governed by the choice of valve material, but it has also been shown that certain manufacturing techniques can be used to tune the microstructure of the material, itself such as in the case of oriented block copolymers. Furthermore, the choice of manufacturing technique can impose constraints on leaflet geometry (e.g. thickness) while also directly affecting valve durability. Here, one can hardly make a comparison to the growth of native valves. Nature's ability to synthesize, repair, and remodel biological tissue from the nanoscale to macroscale clearly surpasses any existing man-made technology. However, recent developments in self-healing polymers and 3D printing of soft materials highlight potential pathways for the manufacture of artificial organs [226,227].

The clinical success of polymeric valves still faces some extraordinary challenges. Significant advancements in materials science and in valve design and manufacturing are needed before polymeric heart valves become preferred with respect to standard mechanical and bioprosthetic valves. However, transcatheter aortic valve replacements (TAVR) are an emerging class of prosthetic valves where polymers show excellent potential, and this review has highlighted a few examples of polymeric valves currently being developed for TAVR applications [45,47,185,188,192,215,228]. TAVR may very well soon replace surgical aortic valve replacements (SAVR) as the gold standard in valve replacements, as the recent PARTNER 3 clinical studies showed that bioprosthetic TAVR produced outcomes that were superior to or at least as good as bioprosthetic SAVR [229]. Polymeric TAVR, however, has an advantage over bioprosthetic TAVR in that polymeric leaflets can be crimped with little or no impact on leaflet mechanics [45], while crimping of the biological tissue in bioprosthetic TAVR is known to produce irreversible damage to collagen fibers [228,230]. Polymeric valves can also be fully integrated into polymeric valved conduits [40,231] that can be easily crimped to a low diameter, allowing for easy transcatheter deployment even in patients with small native femoral vessels (e.g. children, adolescents and young adults) and obstructed vessels (e.g. atherosclerosis in adults). Finally, the inherent compliance of the polymer material would permit such a tubed device to adapt and conform to a wide range of anatomies and could even permit multiple valve-in-valve procedures, whereas bioprosthetics are currently limited to one or two. The promise of transcatheter deployment technology, coupled with the latest developments in polymeric valve materials, modelling, and fabrication, suggest that we are steadily converging to an ideal valve replacement solution. Clearly, there is much work to be done overall, but one hopes that we are on the cusp of a breakthrough.

Funding

This work was supported in part by the National Institutes of Health [R01-HL-143008] (GF); the Kibel Fund for Aortic Valve Research (GF); the Congenital Heart Defect Coalition (DK); and the Babies Heart Fund for Research in Congenital Heart Disease (DK).

Data availability

Not applicable.

Conflicts of interest

No conflict of interest.

References

[1] D. Bezuidenhout, D.F. Williams, P. Zilla, Polymeric heart valves for surgical implantation, catheter-based technologies and heart assist devices, Biomaterials 36

(2015) 6–25.
[2] S. Arjunon, S. Rathan, H. Jo, A.P. Yoganathan, Aortic valve: mechanical environment and mechanobiology, Ann. Biomed. Eng. 41 (7) (2013) 1331–1346.
[3] J. Butany, M.S. Ahluwalia, C. Fayet, C. Munroe, P. Blit, C. Ahn, Hufnagel valve: the first prosthetic mechanical valve, Cardiovasc. Pathol. 11 (6) (2002) 351–353.
[4] F.J. Schoen, J. Butany, Cardiac Valve Replacement and Related Interventions, Cardiovascular Pathology, 4th ed., Academic Press, 2016, pp. 529–576.
[5] J.M. Brown, S.M. O'Brien, C. Wu, J.A.H. Sikora, B.P. Griffith, J.S. Gammie, Isolated aortic valve replacement in North America comprising 108,687 patients in 10 years: changes in risks, valve types, and outcomes in the Society of Thoracic Surgeons National Database, J. Thorac. Cardiovasc. Surg. 137 (1) (2009) 82–90.
[6] S.D. Culler, et al., Trends in aortic valve replacement procedures between 2009 and 2015: Has transcatheter aortic valve replacement made a difference? Ann. Thorac. Surg. 105 (4) (2018) 1137–1143.
[7] J.L. Kaae, Structure and mechanical properties of isotropic pyrolytic carbons deposited below 1600 °C, J. Nucl. Mater. 38 (1971) 42–50.
[8] H.S. Shim, The behavior of isotropic pyrolytic carbons under cyclic loading, Biomater. Med. Devices Artif. Organs 2 (1) (1974) 55–64.
[9] H.S. Shim, F.J. Schoen, The wear resistance of pure and silicon-alloyed isotropic carbons, Biomater. Med. Devices Artif. Organs 2 (2) (1974) 103–118.
[10] F.J. Schoen, J.L. Titus, G.M. Lawrie, Durability of pyrolytic carbon-containing heart valve prostheses, J. Biomed. Mater. Res. 16 (5) (1982) 559–570.
[11] D.R. Elizondo, E.D. Boland, J.R. Ambrus, J.L. Kurk, Mechanical cardiac valve prostheses: wear characteristics and magnitudes in three bileaflet valves, J. Heart Valve Dis. 5 (Suppl. I) (1996) S115–S123.
[12] S. Saito, et al., Bileaflet mechanical valve replacement: an assessment of outcomes with 30 years of follow-up, Interact. Cardiovasc. Thorac. Surg. 23 (4) (2016) 599–607.
[13] A.P. Yoganathan, W.H. Corcoran, E.C. Harrison, J.R. Carl, The Bjork-Shiley aortic prosthesis: flow characteristics, thrombus formation and tissue overgrowth, Circulation 58 (1) (1978) 70–76.
[14] L.P. Dasi, H.A. Simon, P. Sucosky, A.P. Yoganathan, Fluid mechanics of artificial heart valves, Clin. Exp. Pharmacol. Physiol. 36 (2) (2009) 225–237.
[15] B. Iung, J. Rodes-Cabau, The optimal management of anti-thrombotic therapy after valve replacement: certainties and uncertainties, Eur. Heart J. 35 (42) (2014) 2942–2949a.
[16] E. Girdauskas, M.A. Borger, M.A. Secknus, G. Girdauskas, T. Kuntze, Is aortopathy in bicuspid aortic valve disease a congenital defect or a result of abnormal hemodynamics? A critical reappraisal of a one-sided argument, Eur. J. Cardio-thoracic Surg. 39 (6) (2011) 809–814.
[17] P.M. Den Reijer, et al., Hemodynamic predictors of aortic dilatation in bicuspid aortic valve by velocity-encoded cardiovascular magnetic resonance, J. Cardiovasc. Magn. Reson. 12 (1) (2010) 1–13.
[18] D. Dvir, et al., Standardized definition of structural valve degeneration for surgical and transcatheter bioprosthetic aortic valves, Circulation 137 (4) (2018) 388–399.
[19] T.E. David, S. Armstrong, M. Maganti, Hancock II bioprosthesis for aortic valve replacement: the gold standard of bioprosthetic valves durability? Ann. Thorac. Surg. 90 (3) (2010) 775–781.
[20] T. Bourguignon, et al., Very long-term outcomes of the Carpentier-Edwards Perimount valve in aortic position, Ann. Thorac. Surg. 99 (3) (2015) 831–837.
[21] A. Hasan, et al., Biomechanical properties of native and tissue engineered heart valve constructs, J. Biomech. 47 (9) (2014) 1949–1963.
[22] F.J. Schoen, R.J. Levy, Tissue heart valves: current challenges and future research perspectives, J. Biomed. Mater. Res. 47 (4) (1999) 439–465.
[23] F.J. Schoen, J. Fernandez, L. Gonzalez-Lavin, A. Cernaianu, Causes of failure and pathologic findings in surgically removed Ionescu-Shiley standard bovine pericardial heart valve bioprostheses: emphasis on progressive structural deterioration, Circulation 76 (3) (1987) 618–627.
[24] E.A. Talman, D.R. Boughner, Glutaraldehyde fixation alters the internal shear properties of porcine aortic heart valve tissue, Ann. Thorac. Surg. 60 (2) (1995) S369–S373.
[25] E.A. Talman, D.R. Boughner, Effect of altered hydration on the internal shear properties of porcine aortic valve cusps, Ann. Thorac. Surg. 71 (5) (2001) S375–S378.
[26] D.T. Simionescu, J.J. Lovekamp, N.R. Vyavahare, Degeneration of bioprosthetic heart valve cusp and wall tissues is initiated during tissue preparation: an ultrastructural study, J. Heart Valve Dis. 12 (2) (2003) 226–234.
[27] J.J. Lovekamp, D.T. Simionescu, J.J. Mercuri, B. Zubiate, M.S. Sacks, N.R. Vyavahare, Stability and function of glycosaminoglycans in porcine bioprosthetic heart valves, Biomaterials 27 (8) (2006) 1507–1518.
[28] N.D. Broom, An 'in vitro' study of mechanical fatigue in glutaraldehyde-treated porcine aortic valve tissue, Biomaterials 1 (1) (1980) 3–8.
[29] M.J. Thubrikar, J. Aouad, S.P. Nolan, Patterns of calcific deposits in operatively excised stenotic or purely regurgitant aortic valves and their relation to mechanical stress, Am. J. Cardiol. 58 (3) (1986) 304–308.
[30] I. Vesely, D. Boughner, Analysis of the bending behaviour of porcine xenograft leaflets and of natural aortic valve material: bending stiffness, neutral axis and shear measurements, J. Biomech. 22 (6/7) (1989) 655–671.
[31] I. Vesely, R. Noseworthy, Micromechanics of the fibrosa and the ventricularis in aortic valve leaflets, J. Biomech. 25 (1) (1992) 101–113.
[32] T. Rodriguez-Gabella, R. Puri, P. Voisine, J. Rodés-Cabau, P. Pibarot, Aortic bioprosthetic valve durability, J. Am. Coll. Cardiol. 70 (8) (2017) 1013–1028.
[33] A. Hasan, et al., Electrospun scaffolds for tissue engineering of vascular grafts, Acta Biomater. 10 (1) (2014) 11–25.
[35] G.M. Bernacca, T.G. Mackay, R. Wilkinson, D.J. Wheatley, Calcification and fatigue failure in polyurethane heart valve, Biomaterials 16 (4) (1995) 279–285.
[36] G.M. Bernacca, B. O'Connor, D.F. Williams, D.J. Wheatley, Hydrodynamic function of polyurethane prosthetic heart valves: influences of Young's modulus and leaflet thickness, Biomaterials 23 (1) (2002) 45–50.
[37] T.G. Mackay, D.J. Wheatley, G.M. Bernacca, A.C. Fisher, C.S. Hindle, New polyurethane heart valve prosthesis: design, manufacturing and evaluation, Biomaterials 17 (19) (1996) 1857–1863.
[38] D.J. Wheatley, L. Raco, G.M. Bernacca, I. Sim, P.R. Belcher, J.S. Boyd, Polyurethane: material for the next generation of heart valve prostheses? Eur. J. Cardio-thoracic Surg. 17 (4) (2000) 440–448.
[39] M. Butterfield, D.J. Wheatley, D.F. Williams, J. Fisher, A new design for polyurethane heart valves, J. Heart Valve Dis. 10 (1) (2001) 105–110.
[40] M. Ando, Y. Takahashi, Ten-year experience with handmade trileaflet polytetrafluoroethylene valved conduit used for pulmonary reconstruction, J. Thorac. Cardiovasc. Surg. 137 (1) (2009) 124–131.
[41] B. Zhang, et al., Transcatheter pulmonary valve replacement by hybrid approach using a novel polymeric prosthetic heart Valve : proof of concept in sheep, PLoS One 9 (6) (2014) e100065.
[42] S.H. Daebritz, J.S. Sachweh, et al., Introduction of a flexible polymeric heart valve prosthesis with special design for mitral position, Circulation 108 (10) (2003) 134–139.
[43] S.H. Daebritz, et al., Introduction of a flexible polymeric heart valve prosthesis with special design for aortic position, Eur. J. Cardio-thoracic Surg. 25 (6) (2004) 946–952.
[44] T.E. Claiborne, et al., Toward optimization of a novel trileaflet polymeric prosthetic heart valve via device thrombogenicity emulation, Am. Soc. Artif. Intern. Organs J. 59 (3) (2013) 275–283.
[45] O.M. Rotman, B. Kovarovic, M. Bianchi, M.J. Slepian, D. Bluestein, *In vitro* durability and stability testing of a novel polymeric transcatheter aortic valve replacement valve, Am. Soc. Artif. Intern. Organs J. (2019).
[46] A.G. Kidane, G. Burriesci, M. Edirisinghe, H. Ghanbari, A novel nanocomposite polymer for development of synthetic heart valve leaflets, Acta Biomater. 5 (7) (2009) 2409–2417.
[47] B. Rahmani, et al., A new transcatheter heart valve concept (the TRISKELE): feasibility in an acute preclinical model, EuroInterv. 12 (7) (2016) 901–908.
[48] M. Misfeld, H.H. Sievers, Heart valve macro- and microstructure, Philos. Trans. R. Soc. Biol. Sci. 362 (1484) (2007) 1421–1436.
[49] T.C. Doehring, M. Kahelin, I. Vesely, Mesostructures of the aortic valve, J. Heart Valve Dis. 14 (5) (2005) 679–686.
[50] M.S. Sacks, W. David Merryman, D.E. Schmidt, On the biomechanics of heart valve function, J. Biomech. 42 (12) (2009) 1804–1824.
[51] M. Scott, I. Vesely, Aortic valve cusp microstructure: the role of elastin, Ann. Thorac. Surg. 60 (1995) S391–S394.
[52] M.J. Scott, I. Vesely, Morphology of porcine aortic valve cusp elastin, J. Heart Valve Dis. 5 (5) (1996) 464–471.
[53] R.E. Clark, E.H. Finke, Scanning and light microscopy of human aortic leaflets in stressed and relaxed states, J. Thorac. Cardiovasc. Surg. 67 (5) (1974) 792–804.
[54] R.E. Clark, E.H. Finke, The morphology of stressed and relaxed human aortic leaflets, Trans. Am. Soc. Artif. Intern. Organs 20 (1) (1974) 437–448.
[55] I. Vesely, The role of elastin in aortic valve mechanics, J. Biomech. 31 (2) (1998) 115–123.
[56] L. Gross, M.A. Kugel, Topographic anatomy and histology of the valves in the human heart, Am. J. Pathol. 7 (5) (1931) 445–474.
[57] K.J. Grande-Allen, A. Clabro, V. Gupta, T.N. Wight, V.C. Hascall, I. Vesely, Glycosaminoglycans and proteoglycans in normal mitral valve leaflets and chordae: association with regions of tensile and compressive loading, Glycobiology 14 (7) (2004) 621–633.
[58] J.A. Stella, M.S. Sacks, On the biaxial mechanical properties of the layers of the aortic valve leaflet, J. Biomech. Eng. 129 (5) (2007) 757–766.
[59] H. Tseng, K.J. Grande-Allen, Elastic fibers in the aortic valve spongiosa: a fresh perspective on its structure and role in overall tissue function, Acta Biomater. 7 (5) (2011) 2101–2108.
[60] E.A. Talman, Internal shear properties of fresh porcine aortic valve cusps: implications for normal valve function, J. Heart Valve Dis. 5 (2) (1996) 152–159.
[61] C.E. Eckert, et al., On the biomechanical role of glycosaminoglycans in the aortic heart valve leaflet, Acta Biomater. 9 (1) (2013) 4653–4660.
[62] J.D. Deck, Endothelial cell orientation on aortic valve leaflets, Cardiovasc. Res. 20 (10) (1986) 760–767.
[63] R.L. Leask, N. Jain, J. Butany, Endothelium and valvular diseases of the heart, Microsc. Res. Tech. 60 (2) (2003) 129–137.
[64] I. El-Hamamsy, K. Balachandran, M.H. Yacoub, A.P. Yoganathan, A.H. Chester, Endothelium-dependent regulation of the mechanical properties of aortic valve cusps, J. Am. Coll. Cardiol. 53 (16) (2009) 1448–1455.
[65] C.A. Simmons, Aortic valve mechanics: an emerging role for the endothelium, J. Am. Coll. Cardiol. 53 (16) (2009) 1456–1458.
[66] G. Gabbiani, G.B. Ryan, G. Majno, Presence of modified fibroblasts in granulation tissue and their possible role in wound contraction, Experientia 27 (5) (1971) 549–550.
[67] G. Gabbiani, G. Majno, G.B. Ryan, The fibroblast as a contractile cell: the myofibroblast, Biol. Fibroblast (1973) 139–154.
[68] A. Bairati, S. DeBiasi, Presence of a smooth muscle system in aortic valve leaflets, Anat. Embryol. 161 (3) (1981) 329–340.
[69] N.J. Brand, A. Roy, G. Hoare, A. Chester, M.H. Yacoub, Cultured interstitial cells from human heart valves express both specific skeletal muscle and non-muscle markers, Int. J. Biochem. Cell Biol. 38 (1) (2006) 30–42.
[70] W.D. Merryman, H.Y.S. Huang, F.J. Schoen, M.S. Sacks, The effects of cellular contraction on aortic valve leaflet flexural stiffness, J. Biomech. 39 (1) (2006)

88–96.
[71] J.T. Butcher, R.M. Nerem, Valvular endothelial cells regulate the phenotype of interstitial cells in Co-culture: effects of steady shear stress, Tissue Eng. 12 (4) (2006) 905–915.
[72] E. Rabkin-Aikawa, et al., Clinical pulmonary autograft valves: pathologic evidence of adaptive remodeling in the aortic site, J. Thorac. Cardiovasc. Surg. 128 (4) (2004) 552–561.
[73] E. Rabkin-Aikawa, M. Farber, M. Aikawa, F.J. Schoen, Dynamic and reversible changes of interstitial cell phenotype during remodeling of cardiac valves, J. Heart Valve Dis. 13 (5) (2004) 841–847.
[74] J.D.B. Kershaw, M. Misfeld, H.-H. Sievers, M.H. Yacoub, A.H. Chester, Specific regional and directional contractile responses of aortic cusp tissue, J. Heart Valve Dis. 13 (5) (2004) 798–803.
[75] D.A. Filip, A. Radu, M. Simionescu, Interstitial cells of the heart valves possess characteristics similar to smooth muscle cells, Circ. Res. 59 (3) (1986) 310–320.
[76] R.H. Messier, et al., Dual structural and functional phenotypes of the porcine aortic valve interstitial population: characteristics of the leaflet myofibroblast, J. Surg. Res. 57 (1) (1994) 1–21.
[77] D.L. Mulholland, A.I. Gotlieb, Cell biology of valvular interstitial cells, Can. J. Cardiol. 12 (3) (1996) 231–236.
[78] E.M. Joyce, J. Liao, F.J. Schoen, J.E. Mayer, M.S. Sacks, Functional collagen fiber architecture of the pulmonary heart valve cusp, Ann. Thorac. Surg. 87 (4) (2009) 1240–1249.
[79] J. Leeson-Dietrich, D. Boughner, I. Vesely, Porcine pulmonary and aortic valves: a comparison of their tensile viscoelastic properties at physiological strain rates, J. Heart Valve Dis. 4 (1) (1995) 88–94.
[80] J.E. Hall, Guyton and Hall Textbook of Medical Physiology, 13th ed., Elsevier, Philadelphia, 2016.
[81] P. Stradins, et al., Comparison of biomechanical and structural properties between human aortic and pulmonary valve, Eur. J. Cardio-thoracic Surg. 26 (3) (2004) 634–639.
[82] M. Thubrikar, W.C. Piepgrass, L.P. Bosher, S.P. Nolan, The elastic modulus of canine aortic valve leaflets *in vivo* and *in vitro*, Circ. Res. 47 (5) (1980) 792–800.
[83] M.J. Thubrikar, W.C. Piepgrass, J.D. Deck, S.P. Nolan, Stresses of natural versus prosthetic aortic valve leaflets *in vivo*, Ann. Thorac. Surg. 30 (3) (1980) 230–239.
[84] J.D. Deck, M.J. Thubrikar, P.J. Schneider, S.P. Nolan, Structure, stress, and tissue repair in aortic valve leaflets, Cardiovasc. Res. 22 (1) (1988) 7–16.
[85] H. Sugimoto, M.S. Sacks, Effects of leaflet stiffness on *in vitro* dynamic bioprosthetic heart valve leaflet shape, Cardiovasc. Eng. Technol. 4 (1) (2013) 2–15.
[86] G.W. Christie, Anatomy of aortic heart valve leaflets: the influence of glutaraldehyde fixation on function, Eur. J. Cardio-thoracic Surg. 6 (1992) S25–S33.
[87] V.M. Parfeev, I.V. Grushetskii, E.V. Smurova, Mechanical properties of elastomers for artificial leaflet heart valves, Mech. Compos. Mater. 19 (1) (1983) 92–99.
[88] R.E. Clark, H.M. Karara, A. Cataloglu, P.L. Gould, Close-range stereophotogrammetry and coupled stress analysis as tools in the development of prosthetic devices, Trans. Am. Soc. Artif. Intern. Organs 21 (1) (1975) 71–78.
[89] A. Cataloglu, R.E. Clark, P.L. Gould, Stress analysis of aortic valve leaflets with smoothed geometrical data, J. Biomech. 10 (3) (1977) 153–158.
[90] B.V. Rego, M.S. Sacks, A functionally graded material model for the transmural stress distribution of the aortic valve leaflet, J. Biomech. 54 (2017) 88–95.
[91] M.W. Weston, D.V. LaBorde, A.P. Yoganathan, Estimation of the shear stress on the surface of an aortic valve leaflet, Ann. Biomed. Eng. 27 (4) (1999) 572–579.
[92] C.H. Yap, N. Saikrishnan, G. Tamilselvan, A.P. Yoganathan, Experimental measurement of dynamic fluid shear stress on the aortic surface of the aortic valve leaflet, Biomechanics Model. Mechanobiol. 11 (2012) 171–182.
[93] C.H. Yap, N. Saikrishnan, A.P. Yoganathan, Experimental measurement of dynamic fluid shear stress on the ventricular surface of the aortic valve leaflet, Biomechanics Model. Mechanobiol. 11 (2012) 231–244.
[94] D. Lo, I. Vesely, Biaxial strain analysis of the porcine aortic valve, Ann. Thorac. Surg. 60 (2) (1995) S374–S378.
[95] A. Aggarwal, et al., *In-vivo* heterogeneous functional and residual strains in human aortic valve leaflets, J. Biomech. 49 (12) (2016) 2481–2490.
[96] M. Weiler, C. Hwai Yap, K. Balachandran, M. Padala, A.P. Yoganathan, Regional analysis of dynamic deformation characteristics of native aortic valve leaflets, J. Biomech. 44 (8) (2011) 1459–1465.
[97] Y.F. Missirlis, *In-Vitro* Studies of Human Aortic Valve Mechanics, Rice University, 1974.
[98] Y.F. Missirlis, M. Chong, Aortic valve mechanics-part I: material properties of natural porcine aortic valves, J. Bioeng. 2 (1978) 287–300.
[99] M.J. Thubrikar, The Aortic Valve, CRC Press, Boca Raton, 1990.
[100] J.A. Stella, J. Liao, M.S. Sacks, Time-dependent biaxial mechanical behavior of the aortic heart valve leaflet, J. Biomech. 40 (14) (2007) 3169–3177.
[101] J. Liao, L. Yang, J. Grashow, M.S. Sacks, The relation between collagen fibril kinematics and mechanical properties in the mitral valve anterior leaflet, J. Biomech. Eng. 129 (1) (2007) 78–87.
[102] M.M. Adamczyk, T.C. Lee, I. Vesely, Biaxial strain properties of elastase-digested porcine aortic valves, J. Heart Valve Dis. (2000) 445–453.
[103] A. Balguid, et al., The role of collagen cross-links in biomechanical behavior of human aortic heart valve leaflets - relevance for tissue engineering, Tissue Eng. 13 (7) (2007) 1501–1511.
[104] D. Mavrilas, Y. Missirlis, An approach to the optimization of preparation of bioprosthetic heart valves, J. Biomech. 24 (5) (1991) 331–339.
[105] R.E. Clark, Stress-strain characteristics of fresh and frozen human aortic and mitral leaflets and chordae tendinae, J. Thorac. Cardiovasc. Surg. 66 (2) (1973) 202–208.
[106] I. Vesely, A. Lozon, Natural preload of aortic valve leaflet components during glutaraldehyde fixation: effects on tissue mechanics, J. Biomech. 26 (2) (1993) 121–131.
[107] M. Kalejs, P. Stradins, R. Lacis, I. Ozolanta, J. Pavars, V. Kasyanov, St Jude Epic heart valve bioprostheses versus native human and porcine aortic valves - comparison of mechanical properties, Interact. Cardiovasc. Thorac. Surg. 8 (5) (2009) 553–556.
[108] E.O. Carew, J. Patel, A. Garg, P. Houghtaling, E. Blackstone, I. Vesely, Effect of specimen size and aspect ratio on the tensile properties of porcine aortic valve tissues, Ann. Biomed. Eng. 31 (5) (2003) 526–535.
[109] K.L. Billiar, M.S. Sacks, Biaxial mechanical properties of the natural and glutaraldehyde treated aortic valve cusp—part I: experimental results, J. Biomech. Eng. 122 (2000) 23–30.
[110] K.L. Billiar, M.S. Sacks, Biaxial mechanical properties of the native and glutaraldehyde-treated aortic valve cusp: part II—a structural constitutive model, J. Biomech. Eng. 122 (2000) 327–335.
[111] C. Martin, W. Sun, Biomechanical characterization of aortic valve tissue in humans and common animal models, J. Biomed. Mater. Res. A 100A (2012) 1591–1599.
[112] T. Pham, F. Sulejmani, E. Shin, D. Wang, W. Sun, Quantification and comparison of the mechanical properties of four human cardiac valves, Acta Biomater. 54 (2017) 345–355.
[113] S. Jett, D. Laurence, R. Kunkel, A.R. Babu, K. Kramer, An investigation of the anisotropic mechanical properties and anatomical structure of porcine atrioventricular heart valves, J. Mech. Behav. Biomed. Mater. 87 (2018) 155–171.
[114] G.C. Engelmayr, D.K. Hildebrand, F.W.H. Sutherland, J.E. Mayer, M.S. Sacks, A novel bioreactor for the dynamic flexural stimulation of tissue engineered heart valve biomaterials, Biomaterials 24 (14) (2003) 2523–2532.
[115] J. Liao, E.M. Joyce, M.S. Sacks, Effects of decellularization on the mechanical and structural properties of the porcine aortic valve leaflet, Biomaterials 29 (8) (2008) 1065–1074.
[116] A. Mirnajafi, J.M. Raymer, L.R. McClure, M.S. Sacks, The flexural rigidity of the aortic valve leaflet in the commissural region, J. Biomech. 39 (16) (2006) 2966–2973.
[117] R.V. Southwell, An Introduction to the Theory of Elasticity for Engineers and Physicists, 2nd ed., Oxford University Press, London, 1941.
[118] D.C. Gloeckner, K.L. Billiar, M.S. Sacks, Effects of mechanical fatigue on the bending properties of the porcine bioprosthetic heart valve, Am. Soc. Artif. Intern. Organs J. (1999) 59–63.
[119] N.D. Broom, The stress/strain and fatigue behaviour of glutaraldehyde preserved heart-valve tissue, J. Biomech. 10 (11–12) (1977) 707–724.
[120] N.D. Broom, Fatigue-induced damage in glutaraldehyde-preserved heart valve tissue, J. Thorac. Cardiovasc. Surg. 76 (2) (1978) 202–211.
[121] M.S. Sacks, The biomechanical effects of fatigue on the porcine bioprosthetic heart valve, J. Long Term Eff. Med. Implant. 11 (2001) 231–247.
[122] N. Vyavahare, R.J. Levy, M. Ogle, F.J. Schoen, R. Zand, M. Sacks, Mechanisms of bioprosthetic heart valve failure: fatigue causes collagen denaturation and glycosaminoglycan loss, J. Biomed. Mater. Res. 46 (1) (1999) 44–50.
[123] Y.C. Fung, Biomechanics: Mechanical Properties of Living Tissues, Springer, New York, 1981.
[124] M.S. Sacks, Biaxial mechanical evaluation of planar biological materials, J. Elast. 61 (2000) 199–246.
[125] J.M. Lee, D.W. Courtman, D.R. Boughner, The glutaraldehyde-stabilized porcine aortic valve xenograft. I. Tensile viscoelastic properties of the fresh leaflet material, J. Biomed. Mater. Res. 18 (Jul. 1984) 61–77.
[126] E.O. Carew, A. Garg, J.E. Barber, I. Vesely, Stress relaxation preconditioning of porcine aortic valves, Ann. Biomed. Eng. 32 (4) (2004) 563–572.
[127] A. Anssari-Benam, D.L. Bader, H.R.C. Screen, A combined experimental and modelling approach to aortic valve viscoelasticity in tensile deformation, J. Mater. Sci. Mater. Med. 22 (2) (2011) 253–262.
[128] A. Anssari-Benam, D.L. Bader, H.R.C. Screen, Anisotropic time-dependant behaviour of the aortic valve, J. Mech. Behav. Biomed. Mater. 4 (8) (2011) 1603–1610.
[129] J.S. Grashow, M.S. Sacks, J. Liao, A.P. Yoganathan, Planar biaxial creep and stress relaxation of the mitral valve anterior leaflet, Ann. Biomed. Eng. 34 (10) (2006) 1509–1518.
[130] J.S. Grashow, A.P. Yoganathan, M.S. Sacks, Biaxial stress–stretch behavior of the mitral valve anterior leaflet at physiologic strain rates, Ann. Biomed. Eng. 34 (2) (2006) 315–325.
[131] A. Borghi, S.E.P. New, A.H. Chester, P.M. Taylor, M.H. Yacoub, Time-dependent mechanical properties of aortic valve cusps: effect of glycosaminoglycan depletion, Acta Biomater. 9 (2013) 4645–4652.
[132] K.O. Lim, D.R. Boughner, Low frequency dynamic viscoelastic properties of human mitral valve tissue, Cardiovasc. Res. 10 (1976) 459–465.
[133] A. Anssari-Benam, Y. Tseng, A. Bucchi, A transverse isotropic constitutive model for the aortic valve tissue incorporating rate-dependency and fibre dispersion : application to biaxial deformation, J. Mech. Behav. Biomed. Mater. 85 (2018) 80–93.
[134] Z.L. Shen, H. Kahn, R. Ballarini, S.J. Eppell, Viscoelastic properties of isolated collagen fibrils, Biophys. J. 100 (12) (2011) 3008–3015.
[135] C.A. Rock, T.C. Doehring, Biomechanical properties of fiber bundle and membrane mesostructures of the porcine aortic valve, J. Heart Valve Dis. 25 (1) (2016) 82–89.
[136] S.M. Mijailovich, D. Stamenović, J.J. Fredberg, Toward a kinetic theory of connective tissue micromechanics, J. Appl. Physiol. 74 (2) (1993) 665–681.
[137] W.A. Naimark, J.M. Lee, H. Limeback, D.T. Cheung, Correlation of structure and viscoelastic properties in the pericardia of four mammalian species, Am. J. Physiol. 263 (1992) H1095–H1106.
[138] T.W. Gilbert, M.S. Sacks, J.S. Grashow, S.L.-Y. Woo, S.F. Badylak, M.B. Chancellor, Fiber kinematics of small intestinal submucosa under biaxial and uniaxial stretch,

J. Biomech. Eng. 128 (6) (2006) 890.
[139] A.A.H.J. Sauren, M.C. van Hout, A.A. van Steenhoven, F.E. Veldpaus, J.D. Janssen, The mechanical properties of porcine aortic valve tissues, J. Biomech. 16 (5) (1983) 327–337.
[140] E.P.M. Rousseau, A.A.H.J. Sauren, M.C. van Hout, A.A. van Steenhoven, Elastic and viscoelastic material behaviour of fresh and glutaraldehyde- treated porcine aortic valve tissue, J. Biomech. 16 (5) (1983) 339–348.
[141] E.O. Carew, E.A. Talman, D.R. Boughner, I. Vesely, Quasi-linear viscoelastic theory applied to internal shearing of porcine aortic valve leaflets, J. Biomech. Eng. 121 (1999) 386–392.
[142] T.C. Doehring, E.O. Carew, I. Vesely, The effect of strain rate on the viscoelastic response of aortic valve tissue: a direct-fit approach, Ann. Biomed. Eng. 32 (2) (2004) 223–232.
[143] F. Xu, T. Lu, Introduction to Skin Biothermomechanics and Thermal Pain, Springer, Heidelberg, 2011.
[144] E.J. Weinberg, M.R. Kaazempur-Mofrad, On the constitutive models for heart valve leaflet mechanics, Cardiovasc. Eng. 5 (1) (2005) 37–43.
[145] J.D. Humphrey, F.C. Yin, On constitutive relations and finite deformations of passive cardiac tissue. Part I. A pseudo-strain energy function, J. Biomech. Eng. 109 (1987) 298–304.
[146] C. Martin, T. Pham, W. Sun, Significant differences in the material properties between aged human and porcine aortic tissues, Eur. J. Cardio-thoracic Surg. 40 (1) (2011) 28–34.
[147] Y.C.B. Fung, Elasticity of soft tissues in simple elongation, Am. J. Physiol. 213 (6) (1967) 1532–1544.
[148] F.C. Yin, K. May-Newman, Biaxial mechanical behavior of excised porcine mitral valve leaflets, Am. J. Physiol. Heart Circ. Physiol. 269 (4) (1995) H1319–H1327.
[149] G.A. Holzapfel, R.W. Ogden, Constitutive modelling of arteries, Proc. R. Soc. A Math. Phys. Eng. Sci. 466 (2118) (2010) 1551–1597.
[150] K. May-Newman, F.C. Yin, A constitutive law for mitral valve tissue, J. Biomech. Eng. 120 (1) (1998) 38.
[151] J. Li, X.Y. Luo, Z.B. Kuang, A nonlinear anisotropic model for porcine aortic heart valves, J. Biomech. 34 (10) (2001) 1279–1289.
[152] E.J. Weinberg, M.R.K. Mofrad, Transient, three-dimensional, multiscale simulations of the human aortic valve, Cardiovasc. Eng. 7 (4) (2007) 140–155.
[153] Y. Lanir, A structural theory for the homogeneous biaxial stress-strain relationships in flat collagenous tissues, J. Biomech. 12 (6) (1979) 423–436.
[154] Y. Lanir, Constitutive equations for fibrous connective tissues, J. Biomech. 16 (1) (1983) 1–12.
[155] M.S. Sacks, Incorporation of experimentally-derived fiber orientation into a structural constitutive model for planar collagenous tissues, J. Biomech. Eng. 125 (2) (2003) 280–287.
[156] A. Anssari-Benam, A. Bucchi, H.R.C. Screen, S.L. Evans, A transverse isotropic viscoelastic constitutive model for aortic valve tissue, R. Soc. Open Sci. 4 (2017) 160585.
[157] H. Ghanbari, H. Viatge, A.G. Kidane, G. Burriesci, M. Tavakoli, A.M. Seifalian, Polymer heart valves: new materials, emerging hopes, Trends Biotechnol. 27 (6) (2009) 359–367.
[158] M. Boffito, S. Sartori, C. Mattu, G. Ciardelli, Polyurethanes for Cardiac Applications, Advances in Polyurethane Biomaterials, Elsevier Ltd, 2016, pp. 387–416.
[159] W.S. Haworth, Testing of materials for artificial heart valves, Br. Polym. J. 10 (1978) 297–301.
[160] M.E. Leat, J. Fisher, D.K. Gilding, I.P. Middleton, The mechanical properties of Eurothane low elastic modulus polyurethanes, Adv. Biomater. 10 (1992) 133–139.
[161] M.E. Leat, J. Fisher, A synthetic leaflet heart valve with improved opening characteristics, Med. Eng. Phys. 16 (6) (1994) 470–476.
[162] P. Zioupos, J.C. Barbenel, J. Fisher, Mechanical and optical anisotropy of bovine pericardium, Med. Biol. Eng. Comput. 30 (1) (1992) 76–82.
[163] D.N. Ghista, H. Reul, Optimal prosthetic aortic leaflet valve: design parametric and longevity analyses: development of the Avcothane-51 leaflet valve based on the optimum design analysis, J. Biomech. 10 (5) (1977) 313–324.
[164] M.A. Thornton, I.C. Howard, E.A. Patterson, Three-dimensional stress analysis of polypropylene leaflets for prosthetic heart valves, Med. Eng. Phys. 19 (6) (1997) 588–597.
[165] T.E. Claiborne, J. Sheriff, M. Kuetting, U. Steinseifer, M.J. Slepian, D. Bluestein, *In vitro* evaluation of a novel hemodynamically optimized trileaflet polymeric prosthetic heart valve, J. Biomech. Eng. 135 (2) (2013) 21021–21028.
[166] C.R. McMillin, Physical testing of elastomers for cardiovascular applications, Artif. Organs 7 (1) (1983) 78–91.
[167] S.L. Gallocher, A.F. Aguirre, V. Kasyanov, L. Pinchuk, R.T. Schoephoerster, A novel polymer for potential use in a trileaflet heart valve, J. Biomed. Mater. Res. B Appl. Biomater. 79B (2) (2006) 325–334.
[168] O.M. Rotman, et al., Novel polymeric valve for transcatheter aortic valve replacement applications: *in vitro* hemodynamic study, Ann. Biomed. Eng. 47 (1) (2019) 113–125.
[169] Q. Wang, A.J. McGoron, R. Bianco, Y. Kato, L. Pinchuk, R.T. Schoephoerster, *In-vivo* assessment of a novel polymer (SIBS) trileaflet heart valve, J. Heart Valve Dis. 19 (4) (2010) 499–505.
[170] R. Renz, V. Altstadt, G.W. Ehrenstein, Hysteresis measurements for characterizing the dynamic fatigue of R-SMC, J. Reinf. Plast. Compos. 7 (1988) 413–434.
[171] M. El Fray, P. Prowans, J.E. Puskas, V. Altstadt, Biocompatibility and fatigue properties of polystyrene-polyisobutylene-polystyrene, an emerging thermoplastic elastomeric biomaterial, Biomacromolecules 7 (2006) 844–850.
[172] Y. Zhou, L. Pinchuk, Crosslinked Polyolefins for Biomedical Applications and Method of Making Same, United States Patent 9,382,357 B2, Jul. 5, 2016.
[173] G.M. Bernacca, I. Straub, D.J. Wheatley, Mechanical and morphological study of biostable polyurethane heart valve leaflets explanted from sheep, J. Biomed. Mater. Res. 61 (1) (2002) 138–145.
[174] G.M. Bernacca, T.G. Mackay, D.J. Wheatley, *In vitro* function and durability of a polyurethane heart valve - material considerations, J. Heart Valve Dis. 5 (5) (1996) 538–542.
[175] L.E. Millon, W.K. Wan, The polyvinyl alcohol – bacterial cellulose system As a new nanocomposite for biomedical applications, J. Biomed. Mater. Res. B Appl. Biomater. 79B (2) (2006) 245–253.
[176] H. Mohammadi, D. Boughner, L.E. Millon, W.K. Wan, Design and simulation of a poly(vinyl alcohol)—bacterial cellulose nanocomposite mechanical aortic heart valve prosthesis, Proc. Inst. Mech. Eng. H J. Eng. Med. 223 (6) (2009) 697–711.
[177] M. Serrani, et al., A computational tool for the microstructure optimization of a polymeric heart valve prosthesis, J. Biomech. Eng. 138 (6) (2016) 061001.
[178] G. Cacciola, G.W.M. Peters, P.J.G. Schreurs, J.D. Janssen, Development and testing of a synthetic fiber-reinforced three-leaflet heart valve, Biomimetics 4 (2) (1996) 83–103.
[179] J. De Hart, G. Cacciola, P.J.G. Schreurs, G.W.M. Peters, A three-dimensional analysis of a fibre-reinforced aortic valve prosthesis, Journal of Biomechanics 31 (7) (1998) 629–638.
[180] G. Cacciola, G.W.M. Peters, F.P.T. Baaijens, A synthetic fiber-reinforced stentless heart valve, J. Biomech. 33 (6) (2000) 653–658.
[181] M. Kütting, J. Roggenkamp, U. Urban, T. Schmitz-Rode, U. Steinseifer, Polyurethane heart valves: past, present and future, Expert Rev. Med. Devices 8 (2) (2011) 227–233.
[182] E.L. Gerring, B.J. Bellhouse, F.H. Bellhouse, W.S. Haworth, Long term animal trials of the oxford aortic/pulmonary valve prosthesis without anticoagulants, Trans. Am. Soc. Artif. Intern. Organs 20 (1) (1974) 703–707.
[183] M.V. Vellayappan, et al., Tangible nanocomposites with diverse properties for heart valve application, Sci. Technol. Adv. Mater. 16 (3) (2015) 033504.
[185] B. Rahmani, et al., *In vitro* hydrodynamic assessment of a new transcatheter heart valve concept (the TRISKELE), J. Cardiovasc. Trans. Res. 10 (2) (2016) 104–115.
[186] R.Y. Kannan, H.J. Salacinski, P.E. Butler, A.M. Seifalian, Polyhedral oligomeric silsesquioxane nanocomposites: the next generation material for biomedical applications, Acc. Chem. Res. 38 (11) (2005) 879–884.
[187] R.Y. Kannan, et al., The degradative resistance of polyhedral oligomeric silsesquioxane nanocore integrated polyurethanes : an *in vitro* study, Biomaterials 27 (2006) 1971–1979.
[188] B. Rahmani, S. Tzamtzis, H. Ghanbari, G. Burriesci, A.M. Seifalian, Manufacturing and hydrodynamic assessment of a novel aortic valve made of a new nanocomposite polymer, J. Biomech. 45 (7) (2012) 1205–1211.
[189] L.E. Millon, H. Mohammadi, W.K. Wan, Anisotropic polyvinyl alcohol hydrogel for cardiovascular applications, J. Biomed. Mater. Res. B Appl. Biomater. 79B (2) (2006) 305–311.
[190] H. Mohammadi, Nanocomposite biomaterial mimicking aortic heart valve leaflet mechanical behaviour, Proc. Inst. Mech. Eng. H J. Eng. Med. 225 (2011) 718–722.
[191] H. Mohammadi, G. Fradet, A Proposed Percutaneous Aortic Valve Made of Cryogel, *The Heart Valve Society*, 2018 [Online]. Available: http://heartvalvesociety.org/meeting/abstracts/2018/P168.cgi.
[192] M.M. Rozeik, D.J. Wheatley, T. Gourlay, Investigating the suitability of carbon nanotube reinforced polymer in transcatheter valve applications, Cardiovasc. Eng. Technol. 8 (3) (2017) 357–367.
[193] D.N. Ghista, Toward an optimum prosthetic trileaflet aortic-valve design, Med. Biol. Eng. 14 (2) (1976) 122–129.
[194] J.L. Mercer, Acceptable size of the pulmonary valve ring in congenital cardiac defects, Ann. Thorac. Surg. 20 (5) (1975) 567–570.
[195] M.S. Hamid, H.N. Sabbah, P.D. Stein, Influence of stent height upon stresses on the cusps of closed bioprosthetic valves, J. Biomech. 19 (9) (1986) 759–769.
[196] N.S. Braunwald, T. Cooper, A.G. Morrow, Complete replacement of the mitral valve. Successful clinical application of a flexible polyurethane prosthesis, J. Thorac. Cardiovasc. Surg. 40 (1960) 1–11.
[197] J.S. Sachweh, S.H. Daebritz, Novel 'biomechanical' polymeric valve prostheses with special design for aortic and mitral position: a future option for pediatric patients? Am. Soc. Artif. Intern. Organs J. 52 (5) (2006) 575–580.
[198] I. Gregoric, et al., Preclinical assessment of a trileaflet mechanical valve in the mitral position in a calf model, Ann. Thorac. Surg. 77 (1) (2004) 196–202.
[199] G. Burriesci, F.C. Marincola, C. Zervides, Design of a novel polymeric heart valve, J. Med. Eng. Technol. 34 (1) (2010) 7–22.
[200] B.B. Roe, J.W. Owsley, P.C. Boudoures, Experimental results with a prosthetic aortic valve, J. Thorac. Surg. 36 (4) (1958) 563–570.
[201] B.B. Roe, P.B. Kelly Jr., J.L. Myers, D.W. Moore, Tricuspid leaflet aortic valve prosthesis, Circulation 33 (1966) I124–I130.
[202] B.B. Roe, D. Moore, Design and fabrication of prosthetic valves, Exp. Med. Surg. 16 (2–3) (1958) 177–182.
[203] K.P. Chong, D.W. Wieting, N.H.C. Hwang, J.H. Kennedy, Stress analysis of normal human aortic valve leaflets during diastole, Biomater. Med. Devices Artif. Organs 1 (1973) 307–323.
[204] C.B. Wisman, W.S. Pierce, J.H. Donachy, W.E. Pae, J.L. Myers, G.A. Prophet, Polyurethane trileaflet cardiac valve prosthesis - *in vitro* and *in vivo* studies, Trans. Am. Soc. Artif. Intern. Organs 28 (1982) 164–168.
[205] H. Jiang, G. Campbell, D. Boughner, W.K. Wan, M. Quantz, Design and manufacture of a polyvinyl alcohol (PVA) cryogel tri-leaflet heart valve prosthesis, Med. Eng. Phys. 26 (4) (2004) 269–277.
[206] K. Li, W. Sun, Simulated transcatheter aortic valve deformation: a parametric study on the impact of leaflet geometry on valve peak stress, Int. j. numer. method. biomed. eng. 33 (3) (2017) 1–14.

[207] F. Piatti, et al., Hemodynamic and thrombogenic analysis of a trileaflet polymeric valve using a fluid-structure interaction approach, J. Biomech. 48 (13) (2015) 3641–3649.
[208] M.C. Hsu, et al., Dynamic and fluid–structure interaction simulations of bioprosthetic heart valves using parametric design with T-splines and Fung-type material models, Comput. Mech. 55 (6) (2015) 1211–1225.
[209] S.H. Gharaie, Y. Morsi, A novel design of a polymeric aortic valve, Int. J. Artif. Organs 38 (5) (2015) 259–270.
[210] F. Xu, et al., A framework for designing patient-specific bioprosthetic heart valves using immersogeometric fluid–structure interaction analysis, Int. J. Numer. Method. Biomed. Eng. 34 (4) (2018) 1–25.
[211] M.E. Leat, J. Fisher, The influence of manufacturing methods on the function and performance of a synthetic leaflet heart valve, Proc. Inst. Mech. Eng. H J. Eng. Med. 209 (1) (1995) 65–69.
[212] J. Jansen, H. Reul, A synthetic three-leaflet valve, J. Med. Eng. Technol. 16 (1) (1992) 27–33.
[213] S.H. Daebritz, et al., New flexible polymeric heart valve prostheses for the mitral and aortic positions, Heart Surg. Forum 7 (5) (2004) 371–378.
[214] M. Herold, et al., The Helmholtz Institute tri-leaflet polyurethane heart valve prosthesis: design, manufacturing and first *in-vitro* and *in-vivo* results, Polyurethanes Biomed. Eng. II (1987) 231–256.
[215] O.M. Rotman, B. Kovarovic, W.C. Chiu, et al., Novel polymeric valve for transcatheter aortic valve replacement applications: *in vitro* hemodynamic study, Ann. Biomed. Eng. 47 (1) (2019) 113–125.
[216] E. Imamura, M.P. Kaye, Function of expanded-polytetrafluoroethylene laminated trileaflet valves in animals, Mayo Clin. Proc. 52 (12) (1977) 770–775.
[217] A.I. Isayev, D.L. Crouthamel, Residual Stress Development in the Injection Molding of Polymers, Polymer-Plastics Technology and Engineering 22 (2) (1984) 177–232.
[218] J. Stasiak, et al., A bio-inspired microstructure induced by slow injection moulding of cylindrical block copolymers, Soft Matter 10 (32) (2014) 6077–6086.
[219] D. Rottenberg, E. Sondak, D. Haimovich, Method for Producing Heart Valves, United States Patent 6,165,215, Dec. 26, 2000.
[220] C. Escobedo, et al., Hydrodynamic effects of the partial opening of a trileaflet valve, Annu. Int. Conf. IEEE Eng. Med. Biol. - Proc. (2006) 2896–2899.
[221] E. Sacristan, et al., Development of a universal second generation pneumatic ventricular assist device and drive unit, Proc. 25th Annu. Int. Conf. IEEE Eng. Med. Biol. Soc. 1 IEEE, 2003, pp. 427–430.
[222] G.E. Chetta, J.R. Lloyd, The design, fabrication and evaluation of a trileaflet prosthetic heart valve, Trans. ASME 102 (1980) 34–41.
[223] G. Zhu, Q. Yuan, J.H. Yeo, M. Nakao, Thermal treatment of expanded polytetrafluoroethylene (ePTFE) membranes for reconstruction of a valved conduit1, Bio Med. Mater. Eng. 26 (2015) S55–S62.
[224] F. Nistal, et al., *In vivo* experimental assessment of polytetrafluoroethylene trileaflet heart valve prosthesis, J. Thorac. Cardiovasc. Surg. 99 (6) (1990) 1074–1081.
[225] M. Koh, et al., Long-term outcome of right ventricular outflow tract reconstruction using a handmade tri-leaflet conduit, Eur. J. Cardio-thoracic Surg. 27 (5) (2005) 807–814.
[226] U. Jammalamadaka, K. Tappa, Recent advances in biomaterials for 3D printing and tissue engineering, J. Funct. Biomater. 9 (1) (2018) 22.
[227] P.S. Kowalski, C. Bhattacharya, S. Afewerki, R. Langer, Smart biomaterials: recent advances and future directions, ACS Biomater. Sci. Eng. 4 (11) (2018) 3809–3817.
[228] O.M. Rotman, M. Bianchi, R.P. Ghosh, B. Kovarovic, D. Bluestein, Principles of TAVR valve design, modelling, and testing, Expert Rev. Med. Devices 15 (11) (2018) 771–791.
[229] M.J. Mack, et al., Transcatheter aortic-valve replacement with a balloon-expandable valve in low-risk patients, N. Engl. J. Med. 380 (18) (2019) 1695–1705.
[230] S.H. Alavi, E.M. Groves, A. Kheradvar, The effects of transcatheter valve crimping on pericardial leaflets, Ann. Thorac. Surg. 97 (4) (2014) 1260–1266.
[231] F.B. Russell, et al., Development of seamless tri-leaflet valves, Trans. Am. Soc. Artif. Intern. Organs 26 (1980) 66–71.
[232] J.W. Boretos, W.S. Pierce, Segmented polyurethane: a new elastomer for biomedical applications, Science 158 (3807) (1967) 1481–1482.
[233] S.L. Hilbert, E.E. Eidbo, M. Jones, V.J. Ferrans, Y. Tomita, Evaluation of explanted polyurethane trileaflet cardiac valve prostheses, J. Thorac. Cardiovasc. Surg. 94 (3) (1987) 419–429.
[234] S.L. Gallocher, Durability Assessment of Polymer Trileaflet Heart Valves, Florida International University, 2007.
[235] D.A. Prawel, et al., Hemocompatibility and hemodynamics of novel hyaluronan–polyethylene materials for flexible heart valve leaflets, Cardiovasc. Eng. Technol. 5 (1) (2014) 70–81.
[236] F. Guo, et al., Novel transcatheter aortic heart valves exhibiting excellent hemodynamic performance and low-fouling property, J. Mater. Sci. Technol. 35 (1) (2019) 207–215.
[237] N.S. Braunwald, It will work - the first successful mitral valve replacement, Ann. Thorac. Surg. 48 (1989) S1–S3.
[238] K. Iwasaki, M. Umezu, K. Iijima, A. Inoue, K. Imachi, C.X. Ye, Development of a polymer bileaflet valve to realize a low-cost pulsatile blood pump, 27 (1) (2003) 78–83.
[239] B.B. Roe, Late follow-up studies on flexible leaflet prosthetic valves, J. Thorac. Cardiovasc. Surg. 58 (1) (1969) 59–61.
[240] G.M. Bernacca, T.G. Mackay, R. Wilkinson, D.J. Wheatley, Polyurethane heart valves: fatigue failure, calcification, and polyurethane structure, J. Biomed. Mater. Res. 34 (3) (1997) 371–379.
[241] T. Akutsu, B. Dreyer, W.J. Kolff, Polyurethane artificial heart valves in animals, J. Appl. Physiol. 14 (1959) 1045–1048.
[242] J. Jansen, S. Willeke, B. Reiners, P. Harbott, H. Reul, G. Rau, New J-3 flexible-leaflet polyurethane heart valve prosthesis with improved hydrodynamic performance, Int. J. Artif. Organs 14 (10) (1991) 655–660.
[243] D.J. Wheatley, et al., Hydrodynamic function of a biostable polyurethane flexible heart valve after six months in sheep, Int. J. Artif. Organs 24 (2) (2001) 95–101.
[244] G.M. Bernacca, T.G. Mackay, M.J. Gulbransen, A.W. Donn, D.J. Wheatley, Polyurethane heart valve durability - effects of leaflet thickness and material, Int. J. Artif. Organs 20 (6) (1997) 327–331.
[245] S.S. D'Souza, M. Butterfield, J. Fisher, Kinematics of synthetic flexible leaflet heart valves during accelerated testing, J. Heart Valve Dis. 12 (1) (2003) 110–120.
[246] H.-L. Leo, H. Simon, J. Carberry, S.-C. Lee, A.P. Yoganathan, A comparison of flow field structures of two tri-leaflet polymeric heart valves, Ann. Biomed. Eng. 33 (4) (2005) 429–443.
[247] H.L. Leo, L.P. Dasi, J. Carberry, H.A. Simon, A.P. Yoganathan, Fluid dynamic assessment of three polymeric heart valves using particle image velocimetry, Ann. Biomed. Eng. 34 (6) (2006) 936–952.
[248] T. Attmann, U. Steinseifer, J. Cremer, G. Lutter, Percutaneous valve replacement: a novel low-profile polyurethane valved stent, Eur. J. Cardio-thoracic Surg. 30 (2) (2006) 379.
[249] A. Metzner, et al., Percutaneous pulmonary polyurethane valved stent implantation, J. Thorac. Cardiovasc. Surg. 139 (3) (2010) 748–752.
[250] K.S. Park, H. Appa, C. Visagie, D. Bezuidenhout, P.P. Zilla, A Prosthetic Heart Valve, United States Patent Application 2016/0067038 A1, Mar 10, 2016.
[251] J. Scherman, et al., Transcatheter Valve with Hollow-Balloon for Rheumatic Aortic Incompetence, *EACTS Daily News*, 08-Oct-2017, pp. 4–5.
[252] N.S. Braunwald, A.G. Morrow, A late evaluation of flexible Teflon prostheses utilized for total aortic valve replacement, J. Thorac. Cardiovasc. Surg. 49 (1965) 485–496.
[253] H. Mohri, E.A. 2nd Hessel, R.J. Nelson, H.N. Anderson, D.H. Dillard, K.A. Merendino, Design and durability test of Silastic trileaflet aortic valve prostheses, J. Thorac. Cardiovasc. Surg. 65 (4) (1973) 576–582.
[254] W.J. Kolff, L.S. Yu, The return of elastomer valves, Ann. Thorac. Surg. 48 (3) (1989) S98–S99.
[255] F. De Gaetano, et al., A newly developed tri-leaflet polymeric heart valve prosthesis, J. Mech. Med. Biol. 15 (2) (2015) 1540009.
[256] F. De Gaetano, et al., Fluid dynamic characterization of a polymeric heart valve prototype (Poli-Valve) tested under continuous and pulsatile flow conditions, Int. J. Artif. Organs 38 (11) (2015) 600–606.
[257] E. Imamura, M.P. Kaye, G.D. Davis, Radiographic assessment of leaflet motion of Gore-Tex laminate trileaflet valves and Hancock xenograft in tricuspid position of dogs, Circulation 56 (6) (1977) 1053–1058.
[258] T.E. Claiborne, D. Bluestein, R.T. Schoephoerster, Development and evaluation of a novel artificial catheter-deliverable prosthetic heart valve and method for *in vitro* testing, Int. J. Artif. Organs 32 (5) (2009) 262–271.
[259] P.F. Gründeman, et al., Flexible mechanoprosthesis made from woven ultra-high-molecular-weight polyethylene fibres: proof of concept in a chronic sheep model, Interact. Cardiovasc. Thorac. Surg. 25 (6) (2017) 942–949.